Lisanne Demelius, BSc

Stability and degradation of p-i-n lead halide perovskite solar cells for different hole transport layers

MASTER'S THESIS

to achieve the university degree of

Diplom-Ingenieurin

Master's degree programme:

Technical Physics

submitted to

Graz University of Technology

Supervisor

Univ.-Prof. Peter Hadley Ph.D.

Institute of Solid State Physics

Co-Supervisor

Univ.-Prof. DI Dr.techn. Gregor Trimmel

Institute of Chemistry and Technology of Materials

In cooperation with AIT Austrian Institute of Technology

Graz, July 2020

AFFIDAVIT

I declare that I have authored this thesis independently, that I have not used other than the declared sources/resources, and that I have explicitly indicated all material which has been quoted either literally or by content from the sources used. The text document uploaded to TUGRAZonline is identical to the present master's thesis.

Date, Signature

"When nothing is sure, everything is possible."

Margaret Drabble

Acknowledgements

I would like to thank Prof. Peter Hadley and Prof. Gregor Trimmel from the TU Graz, and Dr. Neha Bansal and Dr. Marcus Rennhofer from the AIT for supervising my master thesis. I am particularly grateful for the prompt and precise feedback I got from Prof. Peter Hadley, as well as for his support with the EBIC measurements.
Apart from my supervisors, I would like to thank all the people - my working group at the ICTM and the AIT, as well as helpers outside these groups - who contributed to my thesis by supporting and encouraging me. A special thank you goes to Dr. Thomas Rath, from my working group at the ICTM, who always made time to discuss my results with me and to give me valuable advice on how to improve my synthesis process and measurement routines. I would also like to thank Stefan Weber and Indira Kopacic who showed me how to operate most of the measuring instruments at the institute. From the AIT, I would like to thank Ankit Mittal, Rachmat Adhi Wibowo, Selina Götz and Stefan Schrittwieser for their support with the measurements there. Further, I would like to thank Prof. Peter Hadley and Prof. Egbert Zojer for the valuable, enlightening discussion on band diagrams.
Last but not least, I would also like to thank Sina Pohl, Petra Schönfelder and Judith Kirchgässner for their unconditional support as friends and for proofreading parts of my thesis.

Abstract

Perovskite solar cells are a rising star in the field of thin film photovoltaics. Their efficiency increased to over 25 % within hardly more than a decade and has thus reached values comparable to those of crystalline silicon solar cells. The success of perovskite solar cells lies in the rare combination of easy, low-temperature processability and excellent photovoltaic properties. However, serious challenges are faced when it comes to their long-term stability. Degradation can be induced by almost all external factors, such as light, oxygen or humidity. The mechanisms underlying degradation can be complex and are not yet fully understood.

This thesis' work takes a look at the response of perovskite solar cells to several different external stressors, most importantly light, thus contributing to a better understanding of stability and degradation effects. Similar to other thin film photovoltaics, such as CIGS or CdTe, metastable responses to illumination can be observed in perovskite solar cells that is almost fully reversible upon dark storage. In this thesis' work, these metastable effects are examined more closely. In particular, the impact of the choice of hole transport layer is investigated by comparing the stability of cells with organic PEDOT:PSS to cells with inorganic Cs-doped NiO_x as a hole transport layer.

This thesis' work can be divided into two main parts. The first part comprises the successful synthesis, process optimisation and basic characterisation of perovskite solar cells with the aforementioned hole transport layers. In the second part, the stability of the thus assembled photovoltaic devices was examined by using different standard testing protocols (e.g. damp heat testing, dark storage, light soaking) and thin film characterisation techniques (e.g. XRD, EBIC, profilometry, SEM).

The results demonstrate that the choice of hole transport layer has a huge impact on the stability of perovskite solar cells. Devices with inorganic Cs-doped NiO_x exhibit better long term stability as well as a less distinct metastable response to illumination.

Kurzfassung

Perowskitsolarzellen sind ein aufsteigender Stern im Gebiet der Dünnschichtphotovoltaiktechnologie. Innerhalb kaum mehr als eines Jahrzehnts wurden Rekordeffizienzen von über 25 % erzielt. Im Bezug auf ihren Wirkungsgrad kann die Perowskittechnologie also bereits mit kristallinen Siliziumsolarzellen mithalten. Ihren Erfolg haben Perowskitsolarzellen ihrer kostengünstigen Verarbeitbarkeit, die weder hohe Temperaturen noch Hochvakuumbedingungen erfordert, und ihren ausgezeichneten photovoltaischen Eigenschaften zu verdanken, eine vorteilhafte Kombination, die in der Photovoltaik nur selten anzutreffen ist. Allerdings weisen Perowskitsolarzellen eine Schwachstelle auf: ihre schlechte Langzeitstabilität. Fast alle externen Faktoren, wie zum Beispiel Licht, Sauerstoff oder Feuchtigkeit, können zu einer Degradation der Solarzellen führen. Die zugrundeliegenden Prozesse und Mechanismen sind komplex und noch nicht vollständig erforscht.

Die vorliegende Masterarbeit untersucht die Reaktion von Perowskitsolarzellen auf verschiedene externe Stressoren und leistet einen wichtigen Beitrag zum besseren Verständnis ihres Stabilitätsverhalten. Ein besonderer Fokus liegt dabei auf den beobachtbaren Veränderungen unter Beleuchtung. Ähnlich zu anderen Dünnschichtsolarzellentechnologien, wie CIGS oder CdTe, zeigen Perowskitsolarzellen ein metastabiles Verhalten als Reaktion auf Beleuchtung. Lichtinduzierte Veränderungen sind fast vollständig reversibel, wenn die Solarzelle wieder im Dunkeln gelagert wird. Im Rahmen dieser Masterarbeit wurde dieses metastabile Verhalten genauer untersucht und insbesondere die Rolle der Lochtransportschicht (hole transport layer) durch den Vergleich zweier Materialien (organisches PEDOT:PSS und inorganisches Cs-dotiertes NiO_x) unter die Lupe genommen.

Die vorliegende Masterarbeit kann grob in zwei Teile gegliedert werden. Der erste Teil beschäftigt sich mit der Herstellung, Prozessoptimierung und Grundcharakterisierung der Perowskitsolarzellen mit den eben genannten Lochtransportmaterialien. Im zweiten Teil wurde die Stabilität der gefertigten Solarzellen untersucht. Dazu wurden verschiedene Standard Testverfahren (z.B. Lagerung im Dunkeln, MPP-Tracking, Feuchte-Wärme-Testung) und Dünnschichtcharakterisierungsmethoden (z.B. Röntgendiffraktometrie, Profilometrie, Elektronenmikroskopie) verwendet.

Die Ergebnisse zeigen, dass die Wahl des Lochtransportmaterials einen großen Einfluss auf die Stabilität der Perowskitsolarzellen haben. Zellen mit inorganischem Cs-dotierten NiO_x weisen eine bessere Langezeitstabilität sowie ein schwächer ausgeprägtes metastabiles Verhalten auf.

Acronyms

arb. units	Arbitrary units
CB	Conduction band
CBM	Conduction band minimum
DH	Damp heat
DMF	Dimethyl formamide
DMSO	Dimethyl sulfoxide
DSSC	Dye-sensitized solar cell
E_F	Fermi level
E_g	Band gap energy
E_{vac}	Vacuum level
EA	Electron affinity
EBIC	Electron-beam induced current
EQE	External quantum efficiency
ETL	Electron transport layer
EVA	Ethylene-vinyl acetate
FA	Formamidinium
FF	Fill Factor
FTO	Fluorine doped tin oxide
HOMO	Highest occupied molecular orbital
HTL	Hole transport layer
IE	Ionisation energy
ITO	Indium tin oxide
J_{SC}	Short circuit current density
JV-curve/scan	Current density-voltage curve/scan
LS	Light soaking
LUMO	Lowest unoccupied molecular orbital
MA	Methylammonium
MPP	Maximum power point
OPV	Organic photovoltaics
PC(60)BM	[6,6]-Phenyl-C61-butyric acid methyl ester
PCE	Power conversion efficiency
PEDOT:PSS	Poly(3,4-ethylene dioxythiophene):poly(styrenesulfonate)
PSC	Perovskite solar cell
PV	Photovoltaic

RH	Relative Humidity
SEM	Scanning electron microscope
Spiro-OMeTAD	2,2',7,7'-Tetrakis[N,N-di(4-methoxyphenyl)amino]-9,9'-spirobifluorene
TC	Thermal cycling
TCO	Transparent conductive oxide
ToF-SIMS	Time-of-Flight Secondary ion mass spectroscopy
V_{OC}	Open circuit current
VB	Valence band
VBM	Valence band maximum
XRD	X-ray diffraction
XRR	X-ray reflectivity

Contents

Chapter 1

Fundamentals

In light of our society's growing energy demand, the finite nature of fossil resources and the climate crisis we face due to our ongoing excessive CO_2 and greenhouse gas emissions, the development of efficient, low-cost renewable energy sources is more relevant than ever. Besides wind power and hydro power, solar photovoltaics (PV) show huge potential to replace non-renewable energy sources, such as coal, petroleum or natural gas [1].

Solar photovoltaic cells directly convert the sun's energy into electrical power. Their working principle is based on a two-step process. First, incident solar radiation with a photon energy greater or equal to the band gap energy of the active material is absorbed, leading to the generation of an electron-hole pair. In a subsequent step, the generated charge carriers are separated by the cell's structure. The electron is transported to the negative electrode (anode), the hole to the positive electrode (cathode). Thus, electrical power is generated [2]. If the two terminals are electrically connected, a direct current (DC) flows. During operation, photovoltaic devices do not produce any chemical pollution or acoustic noise [3]. They do not require water for their operation nor (chemical) fuel supply, and they can run independently of the electrical power-grid. Their easy scalability and transportability further contribute to the versatility of photovoltaic modules, making them eligible for a wide range of potential applications.

However, the operation of photovoltaic devices is limited by their dependence on light exposure, their power conversion efficiency (PCE) and their finite lifetime [4]. To date, crystalline silicon PV modules constitute the oldest and most common solar cell technology [5]. Typical efficiencies for monocrystalline modules are at about 20 %, while those of polycrystalline silicon are a bit lower (between 15 to 17 %) [6]. The maximum theoretical efficiency of a solar cell is described by the Shockley-Queisser limit. It is valid for a single-junction photovoltaic cell under illumination by the AM 1.5 solar spectrum [3]. The only recombination mechanism taken into account is radiative, in accordance with the principle of detailed balance [7]. These considerations result in a maximum value of 33.7 % for a band gap energy of 1.34 eV [3]. Regarding module lifetimes, manufacturers typically provide warranty periods in the range of 20 to 25 years for crystalline silicon PV modules [8]. Given that silicon-based solar cells constitute the dominant photovoltaic technology and are well-established, one might ask what is still driving the ongoing research on new PV technologies based on materials other than silicon. The main driving force is the lowering of

production costs. In 2018, the silicon wafers for monocrystalline PV modules accounted for approximately 30 % of the total production cost [9]. Due to its indirect band gap, silicon absorbs light poorly, which necessitates the use of fairly thick silicon layers. Furthermore, requirements on the purity of silicon are extremely high and purification processes are both cost and energy intensive [10]. Thin-film photovoltaic cells are based on alternative materials that exhibit a much higher absorption coefficient than silicon, drastically reduce the material consumption and constitute a promising route towards efficient, low-cost PV modules.

1.1 Introduction to perovskite solar cells

Perovskite solar cells are a rising star in the field of thin-film photovoltaics. Research on the use of perovskites in photovoltaic devices has only just commenced in 2005, originally as light-sensitiser in dye-sensitised solar cells (DSSC, see section 1.2.6) [11]. Since then, it has evolved into one of the most extensively researched branches of photovoltaic technologies. It was soon realised that perovskite materials function more like a continuous p-n junction than a dye-sensitiser, which lead to the emancipation of perovskite cells from DSSCs and the establishment of an independent field of research [12]. Within a bit more than a decade, achieved efficiencies increased from initially 3.8 % [11] to the current record of 25.2 % efficiency (March 2020) [13], and 16.1 % for modules of about 800 cm^2 area (May 2019) [14], both registered by NREL - U.S. National Renewable Energy Laboratory. Such fast progress is unique in the field of PV technologies.

But what are the reasons for the fast rise of perovskite solar cells? On the one hand, the perovskite material has proven to be excellently suited for photovoltaic applications, due to its high absorption coefficient, its long carrier life times and diffusion lengths, its tunable chemical composition, and most importantly due to its superb defect tolerance (as summarized in an essay by Egger et al. [15]). The variable composition allows for tuning of the band gap within the broad range of 1.1 and 2.3 eV [16]. On the other hand, perovskite photovoltaics have caught on immediately due to their easy processability. Conventional silicon solar cells require highly pure materials with an accurately controlled amount of dopants. The purification of silicon involves high temperature processes and cost-intensive vacuum technologies are needed for further processing. In contrast, thanks to their defect tolerant nature, perovskite solar cells can be fabricated by simple solution processing (e.g. spin coating followed by a short annealing step at temperatures <150 °C), that is both low-temperature and low-cost and does not require vacuum conditions. It is exactly this combination of excellent optoelectronic properties on the one hand and easy processing methods on the other that intrigues and fascinates the research community. Generally, one would expect low-temperature solution processes to produce rather disordered materials with a high defect density that would thus exhibit very poor optoelectronic properties. This is however not the case. Interestingly, XRD measurements on solution-processed perovskite films reveal a high degree of crystallinity and respectable long-range order. Also, the large carrier life times (ns up to several μs) suggest that both grain boundaries and defects are of benign nature and do not play such an important role in carrier recombination. In a way, perovskite solar cells combine the best of both worlds: easy processing as that for organic solar cells, and excellent optoelectronic properties similar to those of conventional inorganic semiconductors [15].

However, despite the promising efficiencies of perovskite solar cells, serious challenges are faced when it comes to their long-term stability. Because perovskites are ionic crystals, and hence salts, they take on water easily which results in degradation of the complex [17]. Furthermore, the original and still most prominent perovskite composition used in photovoltaics contains the toxic element lead.

1.1.1 Toxicity of lead

When it comes to the potential of PSCs regarding successful commercialisation, opinions within the scientific community differ greatly. Reason for this is the presence of the toxic element lead (Pb) in the perovskite. Though efforts to replace lead have been undertaken, e.g. by using substitutes such as tin (Sn), germanium (Ge), bismuth (Bi) or antimony (Sb), so far achievable efficiencies and stabilities do not come close to those of lead-based perovskites [18]. The most extensively researched substitute is Sn. However, when exposed to ambient air or moisture, the Sn-based perovskite structure degrades within seconds. This is due to the inherent instability of Sn^{2+} that readily oxidises to the more stable Sn^{4+} under ambient conditions, thus leading to a decomposition of the perovskite compound [19]. So far, a proper alternative to lead is still missing.

The World Health Organization (WHO) has classified lead, a toxic metal occurring at low concentrations in the Earth's crust, as 1 of the 10 chemicals most hazardous to public health [20]. The release of lead into the environment can be largely ascribed to human activity, with mining, smelting, use in lead-acid batteries, leaded gasoline, solders, ceramics and paints representing some examples [21]. Human intake of lead takes place primarily via ingestion and inhalation. The WHO has summarized its observed effects on the human body, comprising gastrointestinal, cardiovascular and neurological disturbances as well as impaired fertility and neurodevelopmental impairment especially in children. In 2010, an expert committee, appointed by the FAO (Food and Agriculture Organization of the United Nations) and the WHO, stated that dose-response analysis did not indicate the presence of a threshold for lead intake below which health effects could be considered non-hazardous [22]. In order to reduce health risks and environmental damages the European Union has enforced a *directive on the restriction of the use of certain hazardous substances in electrical and electronic equipment (EEE)* (RoHS). This legislation applies to 6 substances, one of which is lead. Up to now, photovoltaic panels are exempted from the directive [23], i. a. because lead-containing solders are used in silicon-based PV modules [24], but it is doubtful whether this exemption will remain in force in future. There is a number of people calling for the inclusion of photovoltaics in the RoHS [25], especially since the exemption is based on the assumption that a substitution of the hazardous substance is either infeasible or that the environmental and human benefits of continued use are probable to outweigh the detrimental impacts on human health and the environment. With lead-free solders steadily replacing solders containing lead in silicon-based PV modules, this prerequisite is, strictly speaking, not met anymore [24]. The availability of lead-free PV modules of top performance invalidates the key reasoning for exempting photovoltaic panels from the RoHS.

Hailegnaw et al. [26] investigated the impact of rain on $MAPbI_3$ cells and developed a worst case scenario. According to their model, precipitation on a damaged module would result in the complete degradation of the perovskite absorber layer. In case of a broken

encapsulation and the absence of water-protecting layers on top of the perovskite, essentially all lead contained in the module would dissolve to the ground below. The resulting increase in lead concentration in the first centimetre of ground was estimated to be $\approx$ 70 ppm. Since soil particles strongly adsorb lead, the contaminated soil could probably be removed. Although naturally, any additional source of lead pollution should be avoided, the amount of lead per GW produced power that is estimated to enter the environment due to damaged perovskite solar modules is far smaller than that emitted into the air by coal-burning power stations. However, the environmental impact of lead mining and possible health risks to workers due to lead exposure during module manufacturing must be considered, too.

But even while bearing all these concerns and possible objections to lead in mind, perovskite solar cells still represent a fascinating and promising field of research. As indicated below (see 1.2.7), lead-halide perovskites exhibit a unique combination of material properties, unprecedented in other solar cell materials, that makes them exceptionally well-suited for photovoltaic applications. So far, many of the underlying microscopical mechanisms, such as recombination processes or charge transport, lack thorough comprehension. Another challenging issue of perovskite solar cells that is not yet well-understood concerns their stability when exposed to external factors such as oxygen, humidity, heat or light. Advancing a fundamental understanding of the material as well as of its degradation mechanisms may not only result in improved efficiencies and stabilities of lead perovskite solar cells but may also further the search for appropriate lead-substitutes and may also lead to technological applications beyond photovoltaic technology.

1.1.2 The perovskite structure

The following section provides an overview of what is already known about lead-halide perovskites and their extraordinary properties. The perovskite crystal structure was first discovered in $CaTiO_3$ by the Prussian mineralogist Gustav Rose in 1938 and named after the Russian Count Lev. A. Perovskiy [27]. Nowadays, the term perovskite refers to a whole number of materials that exhibit a crystal structure identical to that of $CaTiO_3$, generically denoted as ABX_3 [12]. The class of perovskites relevant for PV applications are the metal-halide perovskites, in which the X-anion is represented by a monovalent halide ion (either Cl^-,I^- or Br^-), the B-cation by a divalent metal ion (most prominently Pb^{2+}) and the monovalent A-cation either by an organic molecule or an inorganic species [28]. The perovskite structure can either occur in the ideal cubic form or in several distorted non-cubic phases, of which the orthorhombic and the tetragonal phase are the most common ones [29]. The occupied phase is of importance as several non-cubic configurations are photovoltaically inactive [30]. The ideal cubic structure can be best visualized in terms of BX_3 octahedra - a B-cation surrounded by 6 X-anions (see Fig. 1.1b). Those octahedra form a cubic network by sharing corners in all 3 dimensions. Each void in between 8 octahedra is then occupied by one of the larger A-cations [31]. If one looks at the unit cell, the A-cations are occupying the cube corners, the B-cations the body-centred position and the X-anions the face-centred positions (see Fig. 1.1a) [12]. In total, one unit cell comprises 5 ions.

Whether a specific compound can form a stable 3D perovskite structure depends primarily on the ratios of ionic radii and can be roughly anticipated by the octahedral factor μ and

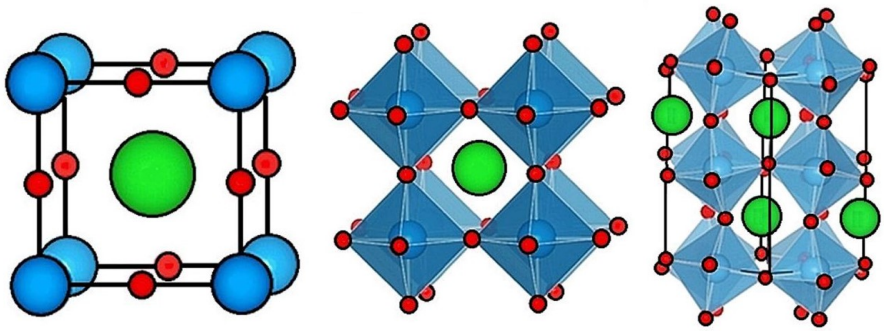

(a) (b) (c)

Figure 1.1: Perovskite structure. (a) Crystal structure of ABX_3, where A (the organic cation) is illustrated in green, B (metal cation) in blue and X (halide anion) in red. (b) An alternative display depicting the BX_6 octahedra, an X anion surrounded by 6 B cations. (c) Possible structure distortion via tilting of the BX_6 octahedra. (Reprinted with permission from Mohd et al. [32]. Copyright © 2018 Elsevier.)

the Goldschmidt tolerance factor t

$$\mu = \frac{R_B}{R_X} \tag{1.1}$$

$$t = \frac{R_X + R_A}{\sqrt{2}(R_X + R_B)} \tag{1.2}$$

where R_B depicts the radius of the B-cation, R_X the radius of the X-anion and R_A the radius of the A-cation. In order to attain stable BX_3-octahedra, μ needs to have a value between 0.442 and 0.895 [33]. Regarding the Goldschmidt tolerance factor, ideal packing, i.e. a minimal volume of unfilled space, is achieved for a value of $t = 1$. However, in practice, a cubic perovskite structure can usually be observed for $0.9 \leq t \leq 1$. Values $0.8 \leq t \leq 0.9$ predominantly result in a distorted perovskite structure with tilted octahedra in order to make up for the imbalance in atomic radii (see Fig. 1.1c). For $t > 1$, hexagonal structures can be observed, whereas values of $t < 0.8$ lead to other non-perovskite structures [34]. One should, however, keep in mind that these models only provide a rough indication of what can be expected for a given composition of ions. An effective way to fine-tune the Goldschmidt tolerance factor is to combine different A-cations and X-cations (see section 1.3.1).

The electronic band structure of lead-halide perovskites (see Fig. 1.2) looks similar to that of a conventional inorganic semiconductor. It exhibits a direct or close-to-direct band gap, which is ideal for efficient photon absorption. Interestingly, the (organic) A-cation does not contribute to the frontier bands. Apparently, its role in determining the optoelectronic properties of the perovskite is negligible and its main influence is structural. The band structure further shows low effective masses, a property one would expect to result in high carrier mobilities. However, compared to inorganic semiconductors of similar effective masses the mobility in perovskites turns out to be 1-2 orders of magnitude lower. While conventional semiconductors, such as silicon or GaAs, typically exhibit mobilities between 500-8000 $cm^2V^{-1}s^{-1}$, lead-halide perovskites only achieve values of 70-220 $cm^2V^{-1}s^{-1}$.

Taking a look at the temperature dependence of the mobility, one finds that both inorganic systems and perovskites behave very similarly. This indicates that the carriers are primarily scattered by temperature-induced lattice vibrations and not by (charged) defects [15]. In their essay Egger et al. [15] suggest that the surprisingly low carrier mobilities in perovskite systems could be related to their remarkable vibrational properties. Compared to inorganic semiconductors, halide perovskites are 3-10 times softer mechanically. As a result, vibrational and rotational modes have low energies and are occupied by many quanta at room temperature. Ion displacements may be so pronounced that anharmonic terms must be taken into account. These rather slow, large-amplitude lattice vibrations lead to structural dynamics that are uncommon for a high quality optoelectronic material. Rather than thinking of a perovskite crystal as a rigid system with well-defined, ordered ion positions, we must turn to a more dynamic picture where anharmonic, multi-mode ion motions induce structural distortions that can be strong locally. Only when averaged over time, the system will reveal its high degree of order.

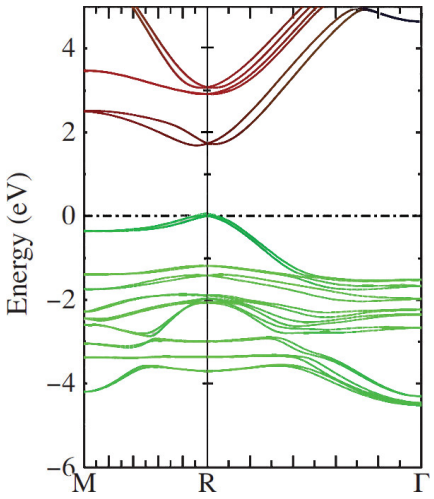

Figure 1.2: Calculated band structure of $MAPbI_3$. Green: bands originating from I 5p orbitals. Red: bands originating from Pb 6p orbitals. Modified and reprinted from Brivio et al. [35]. Copyright © 2014 American Physical Society.

1.1.3 Device Architecture

Perovskite solar cells can be realized employing different materials and device architectures. The original set-up was adopted from DSSCs and involves a mesoporous TiO_2-scaffold as electron transport layer. The scaffold is filled with the active perovskite layer, followed by a planar hole transport layer, most commonly spiro-OMeTAD. This structure is known as mesoporous (n-i-p) architecture [36]. In 2013, Liu et al. [37] demonstrated that the complex mesoporous structure was not necessary to achieve good efficiencies. Similarly high performances could be obtained using a planar device architecture with the perovskite absorber layer sandwiched between a compact ETL and HTL (normal (n-i-p) planar architecture). The order of transport layers can also be reversed, resulting in the so-called

inverted (p-i-n) planar structure. In this case, the HTL (most commonly PEDOT:PSS) is placed directly on the transparent electrode followed by the perovskite and the ETL (most commonly PC(60)BM) [36].

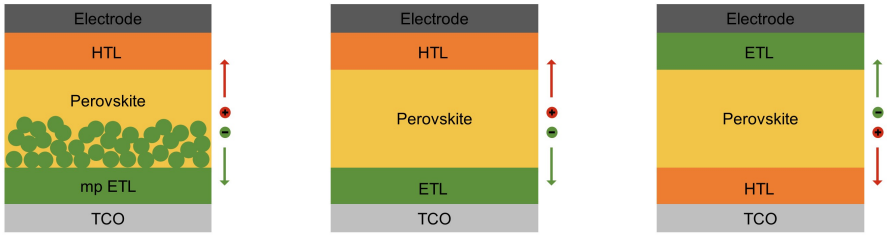

(a) Mesoporous n-i-p (b) Planar n-i-p (c) planar p-i-n (inverted)

Figure 1.3: Three main architectures used for perovskite photovoltaic devices. HTL - Hole Transport Layer, ETL - Electron Transport Layer, mp - mesoporous, TCO - Transparent Conductive Oxide. (Based on Boyd et al. [38])

1.2 Solar cell working principles

In order to understand the working principle of perovskite solar cells it is helpful to first take a look at other already well-comprehended types of solar cells since perovskite devices share properties with several of them. Before that, some fundamental theories regarding energy level alignment and charge transport in organic and inorganic semiconductors are explained, since they are prerequisite to understanding the different working principles. Transport mechanisms in other conducting materials relevant for solar cell fabrication, such as electrodes and transport layers, are also briefly discussed.

1.2.1 Energy level alignment

When two different materials are brought into contact, their electronic interaction depends on the difference in work functions. The work function, commonly denoted as φ, is the minimum thermodynamic work required to remove an electron from the solid to the vacuum, i.e. the energy difference between the Fermi level E_F and the vacuum level E_{vac}. In a metal, the work function φ coincides with the ionization energy IE [39]. For semiconductors, the definition of the work function is somewhat theoretical, since the Fermi level is located inside the band gap where there are no electronic states. In this case, the more practical quantities are the electron affinity EA, i.e. the energy difference between the conduction band (CB) - or the lowest unoccupied molecular orbital (LUMO) - and the vacuum level, and the ionization energy IE, i.e. the energy difference between the valence band (VB) - or the highest occupied molecular orbital (HOMO) - and the vacuum level [39, 40].

Now, when two different materials are brought into contact, electrons from the low-work function material tend to flow to the high-work function material until their Fermi levels

are aligned, i.e. until the system is in thermal equilibrium. In inorganic semiconductors, this electron transfer leads to a space charge region close to the interface that induces band bending. The resulting electric field holds back the electrons in the low-work function material (see Fig. 1.4b) [39]. Due to the large carrier density, the penetration depth of the electric field in the metal is extremely small and the band bending is not visible in the schematic drawings.

Organic semiconductors are molecular crystals, bound by a weak Van der Waals interaction. Instead of a delocalised valence and conduction band, they commonly exhibit HOMO and LUMO levels that are fairly localised on the individual molecules [41]. The difference between the HOMO and LUMO level corresponds to the band gap E_g. When an organic semiconductor is brought into contact with a metal, it depends on the number of mobile charge carriers present in the former whether Fermi level alignment via band bending is achieved. Depending on the type of materials and their purity, both cases with band bending and cases with no band bending have been experimentally observed [42]. Regardless of whether band bending occurs, contact between an organic semiconductor and a metal usually comes with the formation of an interface dipole layer that shifts the vacuum level by Δ (see Fig. 1.5b). Different mechanisms, such as rearrangement of the metal electron cloud or the formation of mirror image charges, have been suggested as the origin of these dipole layers [40].

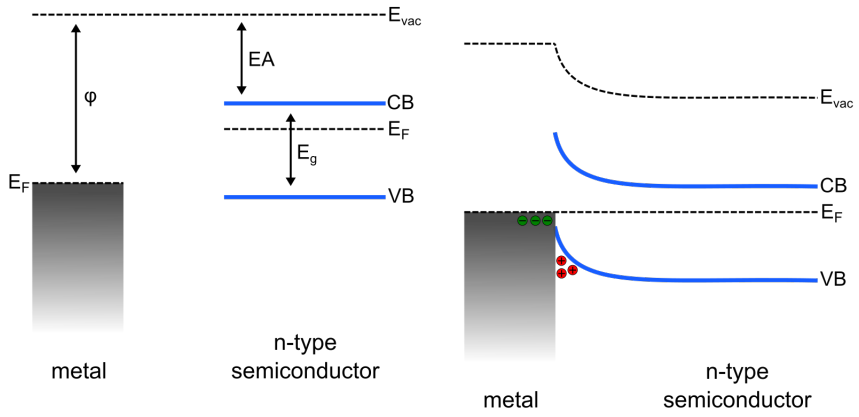

(a) before contact, no electronic interaction

(b) after electron transfer

Figure 1.4: Metal-inorganic semiconductor junction. E_F: Fermi level, CB: conduction band, VB: valence band, E_{vac}: vacuum level, EA: electron affinity, E_g: band gap.

1.2.2 Charge transport

The electronic structure of inorganic semiconductors consists of bands along which charge carriers move as delocalised Bloch waves. For bands to form, the material has to exhibit a high degree of crystallinity and the overlap between orbitals has to be large [41]. For intrinsic semiconductors at room temperature, the number of mobile charge carriers is fairly

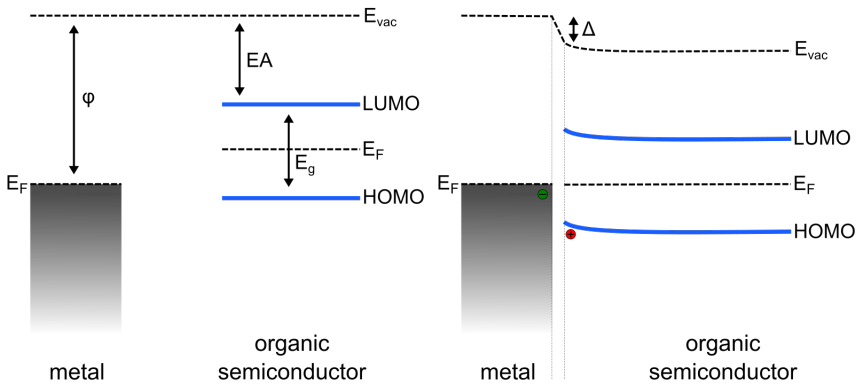

(a) no electronic interaction (Schottky-Mott limit)

(b) formation of an interface dipole layer Δ and band bending

Figure 1.5: Metal-organic semiconductor junction. E_F: Fermi level, HOMO: highest occupied molecular orbital, LUMO: lowest unoccupied molecular orbital, E_{vac}: vacuum level, EA: electron affinity, E_g: band gap, Δ: interface dipole.

low because their band gap only allows for a few electrons to be excited from the valence band into the conduction band. Doping shifts the Fermi level from the middle of the band gap towards one of the bands and significantly increases the number of mobile carriers of one type (either electrons or holes) [43].

As mentioned above, organic semiconductors, on the other hand, consist of loosely-bound molecular crystals. Usually, the orbital overlap between molecules is too small for bands to form. Instead, charge carriers move through the solid by hopping between separate localized states associated with individual molecules. This so-called hopping transport is thermally activated with the activation energy depending on geometry and vibrational properties of the crystal [41]. Mobilities in organic semiconductors are usually several orders of magnitude lower than those in inorganic semiconductors [15, 39, 44].

Another class of materials that is extensively used particularly in thin film photovoltaics are transparent conductive oxides (TCOs). As their name implies they are optically transparent, i.e. their band gap is large enough (> 3 eV) that visible light can pass through without being absorbed, but at the same time they are electrically conductive. This seems contradictory at first glance, since large-band gap materials are usually insulators and typical conductors (metals), on the other hand, have a high plasma frequency ω_p that allows transparency to occur only in the UV range. However, it turns out that in TCOs the conductivity is induced by intrinsic defects and/or dopants [39] that form shallow donor or acceptor states [45]. For common TCOs such as indium tin oxide (ITO) or aluminium-doped zinc oxide (AZO), doping concentrations are high enough to pull the Fermi level up into the conduction band, forming a degenerately doped material and allowing band transport. At the same time, the carrier concentrations remain low enough to keep the plasma frequency below the visible region. Conductivities of TCOs are usually a few orders of magnitude lower than that of metals [39].

Commonly used hole and electron transport materials, such as zinc oxide (ZnO) or nickel

oxide (NiO_x), have properties similar to those of TCOs. However, instead of active doping, interstitial metal atoms and/or oxygen vacancies act as native donors [45,46]. Depending on temperature, charge carriers either move by hopping between these impurity sites, similar to organic semiconductors, or electrons are thermally excited from the donor states into the conduction band, resulting in band-like transport [47,48]. In general, achieved conductivities are lower than those of TCOs.

1.2.3 Inorganic pn-junction solar cells

The classic example of a photovoltaic device is surely the crystalline silicon (c-Si) solar cell. It is based on a large-area pn-junction, i.e. two adjacent silicon layers, one p-doped, the other n-doped. Electrons from the n-doped layer diffuse into the p-doped layer and combine with the holes there, thus depleting the region close to the interface of mobile charge carriers. The remaining positively ionized donors in the n-type region and the negatively ionized acceptors in the p-type region build up an electric field (V_bi, built-in potential) that counteracts the diffusive motion of the majority carriers. A dynamic equilibrium is reached [49]. Whenever an electron-hole pair is generated by absorption of a photon within the depletion region, the charge carriers are separated by the built-in electric field of the pn-junction and drift towards their respective electrodes. In practice, two thin, heavily doped layers are added next to the metal electrodes to form tunnel contacts. Figure 1.6a shows the architecture of a generic pn-junction solar cell, fig. 1.6b the corresponding band diagram.

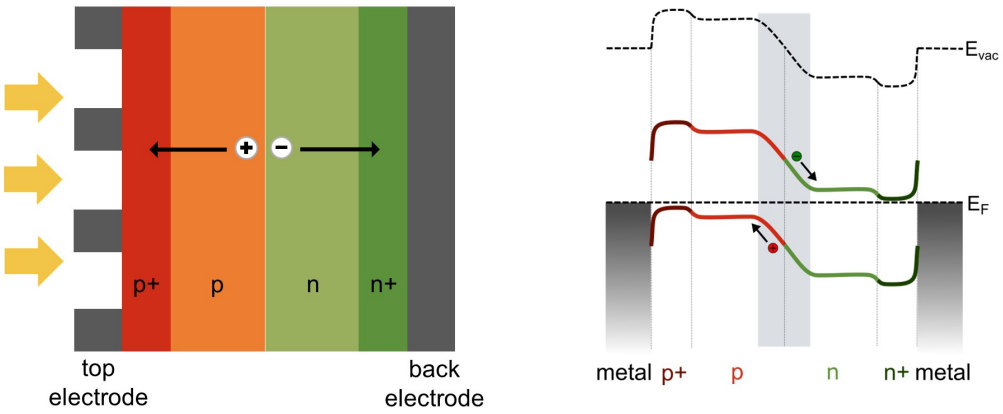

(a) Generic architecture

(b) Schematic band diagram. Blue shaded region: depletion area

Figure 1.6: Monocrystalline silicon pn-junction solar cell. E_F: Fermi level, E_{vac}: vacuum level. p+/n+ correspond to heavily doped regions.

1.2.4 Inorganic p-i-n-junction solar cells

In a p-i-n (or n-i-p) device, a relatively thick, intrinsic semiconductor (i) that acts as light absorber is sandwiched between two selective contacts (p and n) with different work functions. The mismatch in work functions induces an (ideally) constant electric field across the intrinsic layer along which generated charges drift towards the p- and n-contacts respectively (see Fig. 1.7b). Amorphous silicon-based (a-Si) solar cells are probably the most common p-i-n devices. For these, all three layers are made from the same semiconductor (silicon) and only differ in doping. In other devices, such as CdTe thin film cells, different materials are used that can bring about energy band offsets at the p-i and i-n junction [50]. Figure 1.7a shows the typical set-up of an a-Si cell, Figure 1.7b its schematic band diagram.

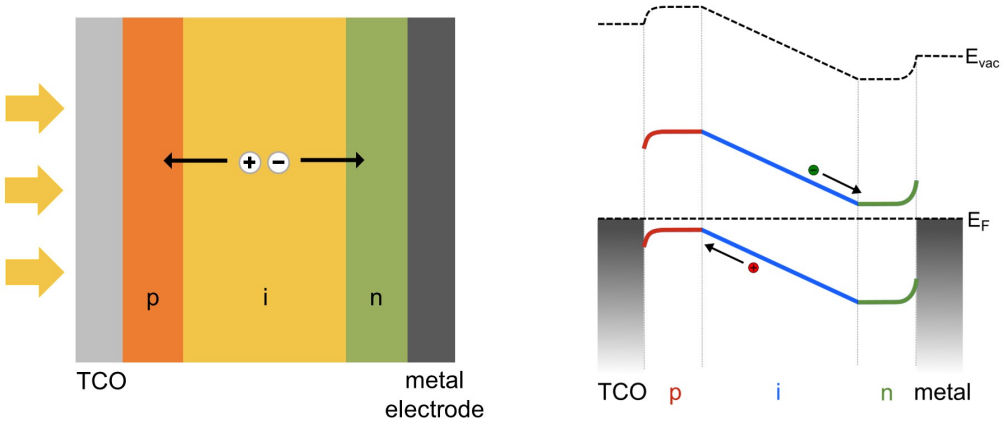

(a) Generic architecture

(b) Schematic band diagram. Blue shaded region: depleted area

Figure 1.7: Amorphous silicon-like p-i-n solar cell. E_F: Fermi level, E_{vac}: vacuum level.

1.2.5 Organic solar cells

Organic solar cells (OSCs) are based on organic semiconductors, i.e. conjugated 'small molecules' (molecular weight of several 100), oligomers or polymers that form crystalline, polycrystalline or amorphous solid films. Conjugation is essential to make the molecules conductive, since it allows for delocalisation of π-electrons. Organic semiconductors differ from their inorganic analogue in several important ways. Firstly, intermolecular binding forces in organic solids are governed by Van der Waals interaction, which are much weaker than the forces holding inorganic materials together (e.g. covalent or ionic bonds). Consequently, the electronic states are very localised on the individual molecules and charge transport takes place via hopping between these states. Mobilities are therefore significantly lower than for inorganic materials [2]. Another fundamental difference is that for organic semiconductors

photo-generated electron-hole pairs are quite strongly bound, with binding energies ranging from 0.6 to 1.2 eV [51]. These excitons do not readily dissociate. An additional force has to be applied to separate the charges. In organic solar cells, this is most commonly achieved by a heterojunction, consisting of a donor and an acceptor material. The donor has higher lying HOMO and LUMO levels than the acceptor. At the interface, this difference creates a locally strong electric field that is able to break up the excitons.

Heterojunctions can be realized in two ways. For a planar, bi-layer junction, donor and acceptor are deposited on top of each other, resulting in one large interface. The more popular variant is the bulk heterojunction, where donor and acceptor are blended together to form a single film, consisting of a percolating network of donor/acceptor domains. If the domain size coincides with the exciton diffusion length, excitons generated within the material are likely to reach an interface at which they will dissociate. To collect the separated charges, selective contacts that conduct only one charge carrier type whilst efficiently blocking the other are added at either side of the heterojunction, followed by the electrodes [2]. Figure 1.8a shows the generic set-up of a bulk heterojunction OSC, Figure 1.8b its schematic band diagram. The band diagram was drawn not as a function of distance across the device but according to a path that might be followed by an (arbitrarily chosen) charge carrier.

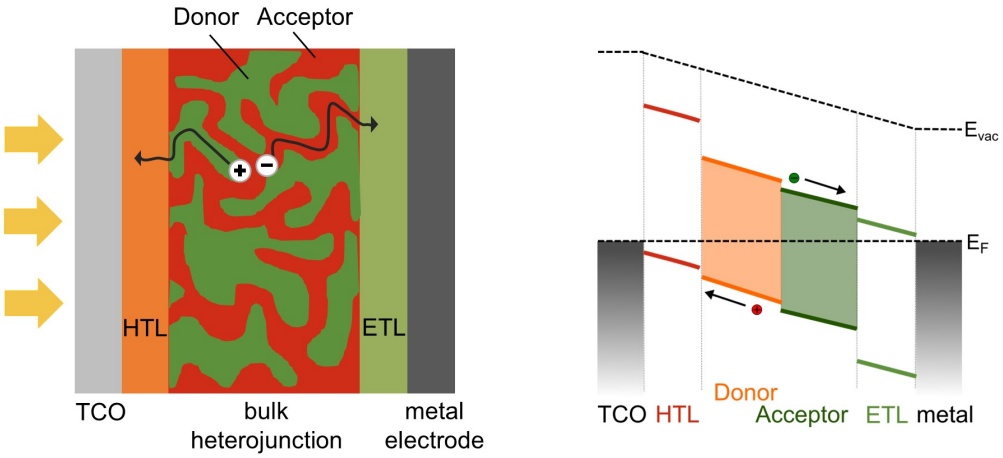

(a) Generic architecture

(b) Schematic energy level diagram

Figure 1.8: Bulk heterojunction organic solar cell. TCO: transparent conductive oxide, HTL: hole transport layer, ETL: electron transport layer, E_F: Fermi level, E_{vac}: vacuum level. The band diagram (b) was drawn for a path a typical charge carrier might take.

1.2.6 Dye-sensitised solar cells

Dye-sensitised solar cells (DSSCs) differ from other solar cell technologies in one important respect. Instead of having a donor and an acceptor that are responsible for both light absorption and charge transport towards electrodes, in DSSCs those tasks are carried out

by separate materials. The dye, usually an organic molecule, solely acts as light absorber and does not have to be a good conductor. The photo-generated charges are separated and transported away by the surrounding structures [2]. In a typical DSSC device, a monolayer of dye molecules is adsorbed on a porous n-type semiconductor scaffold (usually TiO_2) that is immersed in an electrolyte (see Fig. 1.9a). The electrolyte contains a redox system, most commonly $I^{3-}/3I^{-}$.

Under operation, the dye absorbs a photon of an energy matching its band gap, which results in photo-excitation of an electron from the HOMO to the LUMO of the system. The resulting bound electron-hole pair, called exciton, is separated in the following way: The electron from the LUMO of the dye is injected into the lower lying conduction band (CB) of the semiconducting scaffold. From there, it is transported through the scaffold to the underlying electrode. After flowing through an external circuit, the electrons reach the counter electrode, where they reduce the redox system in the electrolyte. Via diffusion, the reduced ions are transported back to the oxidized dye to reduce it, thus 'filling' the hole in the HOMO [12]. A schematic drawing of the energy levels in a DSSC is displayed in Figure 1.9b. The band diagram was drawn not as a function of distance across the device but according to a path that might be followed by an (arbitrarily chosen) charge carrier.

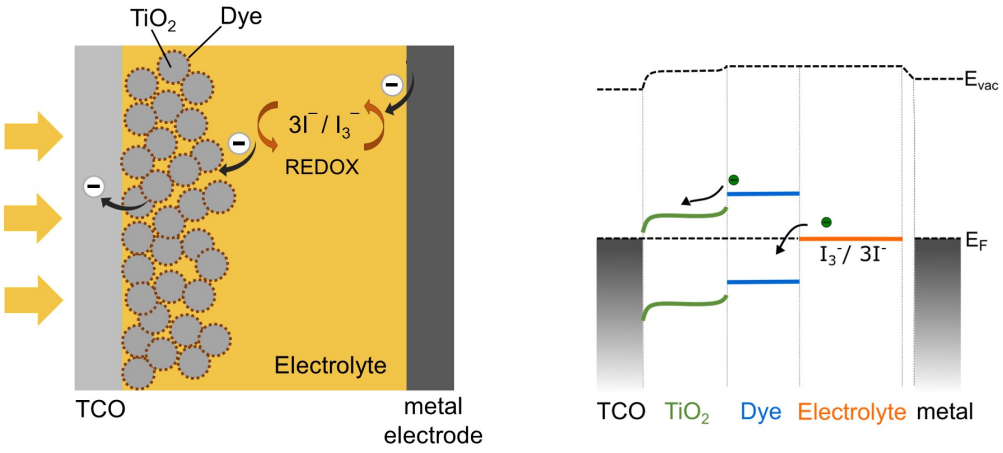

(a) Generic architecture

(b) Schematic energy level diagram

Figure 1.9: Dye-sensitised solar cell. TCO: transparent conductive oxide, E_F: Fermi level, E_{vac}: vacuum level. $3I^-$ /I_3^- is the redox system that allows electron transport through the electrolyte. At the interface between electrolyte and metal in (b), a dipole layer is generated that causes a shift in vacuum level. The band diagram (b) was drawn for a path a typical charge carrier might take.

1.2.7 Perovskite solar cells

When lead-halide perovskites were first used in DSSCs, it was assumed that they work analogous to a dye (see section 1.2.6). However, it was soon revealed that for perovskites

the semiconducting scaffold structure was not necessary to achieve efficient charge carrier transport. Fully working planar device architectures demonstrated that electrons and holes could move through the perovskite film itself. Moreover, exciton binding energies in perovskites were estimated via optical spectroscopy to be only 55 ± 20 meV, indicating that at room temperature almost all generated electrons and holes can be viewed as free charge carriers [52]. Another research group published an even smaller value of 37 meV [53]. This distinguishes perovskite-based devices from organic solar cells, in which much larger exciton binding energies in the range of 0.6 to 1.2 eV are typically found [51].

The above mentioned properties imply that perovskite-based solar cells function more like inorganic p-i-n devices (see section 2.2.4) than DSSCs or exciton-based organic photovoltaics [12].

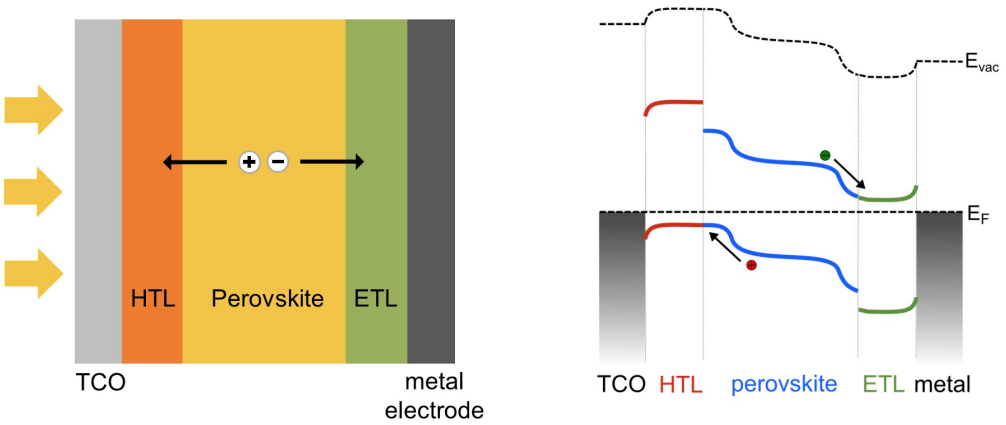

(a) Generic architecture

(b) Schematic energy level diagram (adapted from Edri et al. [50])

Figure 1.10: Planar, inverted (p-i-n) perovskite solar cell. TCO: transparent conductive oxide, HTL: hole transport layer, ETL: electron transport layer, E_F: Fermi level, E_{vac}: vacuum level.

Edri et al. [50] used cross-sectional electron beam-induced current (EBIC) measurements to successfully demonstrate the p-i-n nature of planar, perovskite-based solar cells. (To find out how EBIC works see section 2.2.4.) Mapping of the EBIC signal onto the cross section of the cell revealed two regions of high efficiency, one at the perovskite/ETL, and the other at the perovskite/HTL interface. Holes generated close to the perovskite/HTL interface are efficiently extracted while electrons have to diffuse all across the perovskite layer before they are extracted at the ETL. The opposite is true for charges produced near the perovskite/ETL interface. The further away electrons and holes are generated from their respective sink the higher is their probability to recombine, the lower their chances of being collected. Because electrons and holes are primarily extracted at opposite ends of the cell, the EBIC profile shows two distinct peaks with a significant efficiency drop towards the centre of the absorber layer. From the measured EBIC profile, Edri et al. derived a schematic band diagram for

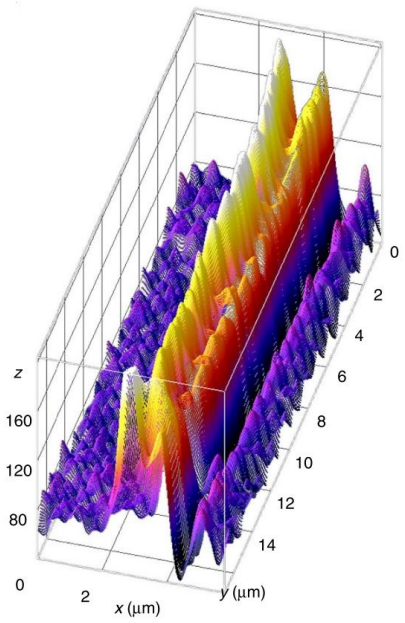

Figure 1.11: 3D surface plot of the EBIC image. Layers in x-direction: Au-HTL-perovskite-ETL-FTO. Reprinted with permission from Edri et al. [50]. Copyright © 2014 by Springer Nature.

the perovskite p-i-n junction (see Fig. 1.10b). Unlike other p-i-n devices such as amorphous silicon-based ones, the electric field within the intrinsic perovskite layer is not homogeneous. The reason for this can be found in the mixed ionic-electronic conductivity of the perovskite. To date, it is widely accepted that halide vacancies (V_X^+) dominate ionic transport. When the perovskite is brought into contact with the respective n- and p-selective layers, the difference in their work functions induces a linear potential drop across the absorber layer. The positively charged V_X^+ drift along the corresponding electric field towards the HTL, building up a region with positive charge. The area close to the ETL, on the other hand, is depleted from halide vacancies and becomes negatively charged. These charged regions lead to band bending similar to that encountered in standard inorganic pn-junctions. Because positively charged vacancies dominate the ion migration, the band diagram takes on an asymmetric shape [54]. Edri et al. [50] further used their EBIC line scans to calculate the effective diffusion lengths. For electrons they found a value of $L_n = 1.9 \pm 0.1$ μm, for holes $L_p = 1.5 \pm 0.2$ μm). Amorphous silicon-based devices, in comparison, only exhibit diffusion lengths of 0.1 - 0.2 μm [50].

1.2.8 Hysteresis in perovskite solar cells

Performing current-voltage (JV) scans of a solar cell is probably the most common method to ascertain its efficiency. However, it does not appear to be a reliable approach for perovskite solar cells because its results depend on scan direction and scan speed. In general, the efficiency derived from the reverse scan (from forward to reverse bias) exceeds that determined from the forward scan. A typical example can be found in Figure 1.12. This

dependence on scan direction is called hysteresis. It implies that the system goes through a transient change when subjected to the external bias and the measurement results therefore do not correspond to its steady state values [55].

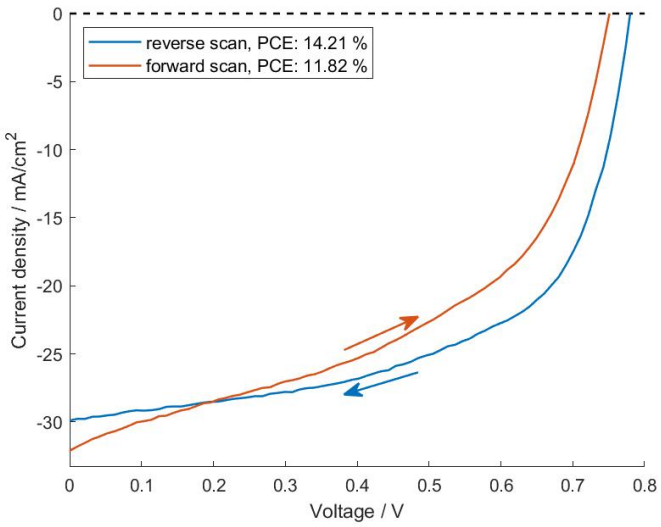

Figure 1.12: Exemplary JV-scans of a perovskite solar cell showing hysteresis. PCE values derived from forward and reverse scan respectively differ significantly.

It is now widely accepted that the already mentioned ion migration (see section 1.2.7) is the main cause for the hysteretic behaviour of perovskite solar cells. As described in the previous section, drift of the mobile ions along the built-in field leads to charge accumulations at the interfaces between the perovskite and the respective charge transport layers. This accumulated charge shields the built-in field, thus flattening the bands in between the interfaces. That way electron-hole pairs photogenerated in the bulk of the absorber do not experience a potential-driven force towards one of the electrodes anymore, which reduces charge extraction efficiency. But if the cell is pretreated with an external voltage larger than the built-in potential, ions will drift in the opposite direction, thus enhancing the built-in field, which results in a more efficient extraction of charges [56]. But ion migration does not only alter the built-in field, it is also assumed to affect trap density and recombination rates at the interfaces. This is supported by the fact that the choice of transport layers significantly influences hysteresis [57]. Another possible cause for hysteresis are ferroelectric effects within the perovskite [58].

There exist two different approaches to circumvent hysteretic effects and determine the steady state efficiency of solar cells. The first involves using slower scan rates (up to several seconds per voltage step) to allow the system to reach its steady state at each measuring point [59]. The other option is to keep the cell at its maximum power point (MPP) until its PCE stabilised [60].

1.3 Understanding the stability of perovskite solar cells

Standard solar panels (e.g. for the installation on roofs) that are currently commercially available exhibit lifetimes of up to 25 years [61]. During operation, solar modules are exposed to temperatures in the range of -40 to 80 °C depending on their geographical location [29]. Proper encapsulation protects cells from external impacts such as oxygen and humidity. However, no encapsulation material is perfectly impermeable and there is always a risk of leakage. Furthermore, the higher the demands for the materials, the higher are their costs. To achieve good long-term stability and to keep the costs low, a high intrinsic stability of the cells themselves is essential [38]. In addition, even a perfect encapsulation cannot protect the solar modules from temperature effects, nor can the exposure to (visible) light and bias voltage be avoided since they are a vital part of the solar cell's operation.

Degradation in perovskite photovoltaic cells, as stated in a review by Berhe et al. [62], can be driven by every single one of the above mentioned external factors: oxygen, moisture, temperature, light (especially high-energy UV light), and bias. In addition to these external impacts, internal mechanisms such as ion migration and chemical reactions at the interfaces can be of relevance. The following sections provide an overview of the present understanding of the different degradation pathways and states possible ways to mitigate them.

1.3.1 Structural stability

Initial efforts in understanding and improving the stability of perovskite solar cells focused on the perovskite structure itself. The chemical composition was continuously optimized to achieve more stable perovskite structures, introducing new ions and varying the mixing ratio [63].

The first perovskite structure that was investigated for use in solar cells was $MAPbI_3$, where MA is short for methylammonium (CH_3NH_3). $MAPbI_3$ has a band gap of about 1.5 eV [64] and adopts a tetragonal phase at room temperature [30]. However, $MAPbI_3$ proved to have rather poor thermal and structural stability [16]. Decomposition of the crystal structure can already be observed at temperatures of 85 °C [65]. In order to achieve both better device efficiency and enhanced stability, the research community began to look for improved compositions, investigating alternatives to the organic cation MA, to iodine as well as to lead. In this section, discussion will be restricted to substitutions of the former two, since the elimination of lead leads to a whole new class of perovskites, the lead-free perovskites.

Koh et al. [66] were the first to examine the organic cation formamidinium (CH_5N_2, for short FA^+) as a substitution to MA. The FA-cation is slightly larger than MA^+ [67], which leads to a smaller band gap of 1.47 eV for $FAPbI_3$ instead of 1.5 eV for $MAPbI_3$. This allows light absorption to take place further into the red, which results in more efficient harvesting. $FAPbI_3$ exhibits two polymorphs, a black trigonal perovskite phase (α-phase) and a yellow non-perovskite hexagonal phase (δ-phase) [68]. The latter is made up of linear chains of face-sharing PbI_6-octahedra [67]. At room temperature, $FAPbI_3$ is found in the yellow, photovoltaically inactive polymorph, while the black phase is only favoured at temperatures above 60 °C [68]. This issue can be resolved by combining both MA and FA to form $MA_xFA_{1-x}PbI_3$. Jeon et al. [67] showed that a value of $x = 0.15$ is enough to stabilise the

trigonal phase at room temperature. Introducing FA into the perovskite crystal comes with an improved thermal stability, i.e. the decomposition temperature is significantly raised compared to $MAPbI_3$ [69].

The A-cation does not necessarily have to be an organic molecule. Using inorganic atoms such as Cs proved beneficial as well (see section below on the triple cation perovskite).

Halide substitution and mixing

As for the X-anion, other halides such as bromine and chlorine have emerged as candidates for replacing iodine. Their ionic radii decrease from I to Br to Cl with 2.2 Å, 1.96 Åand 1.81 Årespectively [64]. Partial substitution of Iodine with the smaller bromine ($MAPb(I_{1-x}Br_x)_3$) was found to reduce the lattice constant [70], increase the band gap of the perovskite (from about 1.5 eV for $x = 0$ to 2.3 eV for $x = 1$) and thus shifts the absorption edge to smaller wavelengths [71]. As a result, only a smaller fraction of the incoming light can be harvested. But at the same time, increasing the Br-content leads to a favourable reduction of charge recombination. Suarez et al. [71] furthermore demonstrated that the incorporation of Br into $MAPbI_3$ results in an improved device stability. Upon 30 days dark storage in a glovebox, a Br-content of 50 % even resulted in an increase of PCE by 37 %, whereas pure $MAPbI_3$ devices experiences a PCE drop by 20 %. Adding bromine to iodine at ratios $x = 0.2$ and 0.29 was also found to significantly improve the device's tolerance towards moisture [70]. The case of chlorine as an X-anion is not yet fully understood. It was shown that chlorine can only be incorporated into the $MAPbI_3$ structure at small amounts (3-4 %), probably due to the large difference in ionic radii of the halogens. However, incorporation of Cl in the perovskite as a dopant still improves charge transport within the layer [72].

Triple cation perovskite

The most widely used perovskite composition today is the triple cation perovskite, developed by Saliba et al. [16] in 2016. To the commonly used molecules MA and FA, Cs is added as a third A-cation (hence the name 'triple cation perovskite'). Cs-cations have a significantly smaller ionic radius (1.81 Å) compared to MA (2.70 Å) and FA (2.79 Å) [73]. Introducing a small amount of Cs into the perovskite structure reduces the 'effective' ionic radius of the A-cation and pushes the Goldschmidt factor further into the desired black perovskite phase. Saliba et al. used the chemical composition $Cs_x(MA_{0.17}FA_{0.83})_{1-x}Pb(I_{0.83}Br_{0.17})_3$. They were able to show that a Cs-content of $x = 5-10$ % significantly increases structural stability, suppresses yellow phase impurities, enhances thermal stability and leads to a higher device efficiency. Additionally, a better reproducibility of device performance could be shown. With MA alone, the exact temperature at the start of the crystallization process is crucial to the stabilisation of the black phase of FA, whereas the triple cation perovskite is much less susceptible to temperature variations during processing [16].

1.3.2 Stability towards oxygen and light

Oxygen exposure is detrimental only in the presence of light, since the perovskite cannot be oxidized in its ground state [74]. However, an electron that is photo-excited into the con-

duction band of the perovskite can be trapped by an O_2-molecule to form superoxide (O_2^-). The superoxide then enrolls in an acid-base reaction with the A-cation of the perovskite, decomposing the structure into methylamine (CH_3NH_2), lead iodide (PbI−2), iodine (I_2) and water [75]. Replacing MA^+ with a less acidic cation, such as FA^+ or Cs^+, can significantly improve photo-oxidative stability [30]. Light exposure alone can, however, initiate different changes in the perovskite photovoltaic device, some of which can be reversed by storing the cell in dark conditions. Illumination can cause halide segregation, i.e. iodine- and bromine-rich regions forming within the perovskite. The varying composition affects the band gap which in turn reduces the achievable V_{oc}. Halide segregation was found to be reversible within minutes upon dark storage [76]. Illumination can also promote the migration of ions and defects [77–79], damage organic charge transport layers and cause interdiffusion of materials at the interfaces [80].

1.3.3 Stability towards moisture

Due to their ionic nature, perovskite crystals are especially susceptible to exposure to moisture. Severe degradation can take place within hours or even minutes, depending on the level of humidity [81]. The polar water molecules permeate the crystal along the grain boundaries [17] and lead to the formation of hydrated compounds. So far, two types of hydrates, one a monohydrate ($MAPbI_3 \cdot H_2O$) [82], the other a dihydrate ($(CH_3NH_3)_4PbI_6 \cdot 2H_2O$) [17], have been observed and identified by the research community. Both compounds consist of a network of isolated PbI_6^--octahedra connected by water molecules. Based on their experimental results, Leguy et al. [17] proposed equation (1.3) as a description of moisture-induced degradation. Upon exposure to humidity, a monohydrate starts to form that may further transform into a dihydrate. Eventually, an equilibrium between the two compounds forms that depends on the humidity level and the time of exposure. Hydration can easily be observed visually by a change from dark brown to a yellowish transparent colour.

$$4MAPbI_3 + 4H_2O \rightleftharpoons 4[MAPbI_3 \cdot H_2O] \leftrightharpoons MA_4PbI_6 \cdot 2H_2O + 3PbI_2 + 2H_2O \tag{1.3}$$

It was demonstrated that the hydration process is to some extent reversible by exposing the samples to dry air. However, reversibility is limited by the formation and phase segregation of PbI_2 [17, 81].

Christians et al. [83] observed that, when stored in the dark, some type of dihydrate formed in the perovskite thin films upon exposure to humidity but no significant amount of PbI_2 could be detected. In contrast, storage of the films in light conditions lead to degradation of the perovskite to PbI_2. Apparently, the moisture-induced decomposition of the perovskite structure is accelerated by illumination. An explanation could be that, in comparison to the ground state, the MA^+-ions are less tightly bound to the PbI_6-octahedra after photo-excitation [84]. Hydration of the perovskite compound involves the formation of a hydrogen bond between the PbI_6-octahedra and H_2O, a process that is favoured when the bonding strength of the MA^+-ion is reduced [83]. Christians et al. [83] further showed that incorporation of H_2O leads to a loss in absorbance of the perovskite film. However, solar cell performance drops much faster, indicating that the efficiency loss is not primarily due to the breakdown of the absorption properties of the perovskite, but instead caused by

changes at the interfaces or by a deterioration of charge transport.

In addition to direct humidity-induced degradation, the presence of moisture also strongly enhances the device's instability towards electric fields and heat, as was investigated by Leijtens et al. [36, 85]. In both cases, degradation due to electric fields or heat was almost negligible when the devices were kept in an inert atmosphere, while the same external stressors lead to rapid decomposition of the perovskite in humid air. As to field-induced degradation, Leijtens et al. proposed the following explanation. In the hydrated phases, the interaction strength between the MA^+-cation and the I^- of the PbI_6-octahedra is lower than that of the MA^+-cation with the water molecules. This most likely increases the mobility of the cations within the structure [36]. The application of an electric field induces a drifting motion of the MA^+-cations, leading to an accumulation of cations at the negative electrode. The remaining destabilised PbI_6^{4-}-octahedra readily decompose to PbI_2 and iodine.

Another effect observed by the research group around Leijtens is the increase in JV-hysteresis with the degree of hydration. This makes sense when one assumes that the formation of hydrated compounds increases the mobility of MA^+-ions and that hysteretic behaviour is mainly caused by ionic motion.

Strategies to reduce moisture ingress and mitigate humidity driven degradation comprise the use of hydrophobic transport layers or the development of proper encapsulation methods (see section 1.3.6).

1.3.4 Stability towards electric fields

The presence of electric fields can cause ion migration [86]. Further, applying a bias to the cell can assist moisture- induced degradation (see above) and promote degradation due to oxygen even in the absence of light [87].

1.3.5 Degradation at the interfaces

The previous sections primarily discussed degradation mechanisms of the perovskite absorber layer itself. However, the device architecture of a fully functioning solar cell comprises several additional layers, such as the electrodes, HTL, ETL and optional passivation/blocking layers. This makes understanding and eliminating device degradation much more complicated, since degradation can occur in all layers and at all interfaces. Mobile ions may diffuse into adjacent layers and initiate chemical reactions between the different materials. The reaction contributing most severely to device degradation probably takes place between the perovskite and the metal electrode. Since almost all metals readily react with halides and/or halogens, it is mostly independent of the exact cell architecture or type of metal used [63].

Xiong et al. [88] showed that storing the unfinished devices (ITO/NiO_x/perovskite) in ambient air for up to 200 h hours did not result in significant degradation, while completed devices collapsed in air within an hour. They concluded that degradation takes place mainly at the perovskite/PCBM/Al interface. Another group subjected their devices (ITO/NiO_x/$MAPbI_3$/PCBM/
Ag) to a temperature of 85 °C for 24 hours in an inert atmosphere, which resulted in considerable degradation, mainly noticeable by a drop V_{oc} and FF. ToF-SIMS measurements

revealed that upon thermal treatment, I^--ions diffuse through the ETL into the metal electrode where they form silver iodide (AgI). When the thermal treatment was applied before deposition of the Ag-electrode, no significant device degradation occurred [63]. However, it might not only be the halide ions that undergo migration. Domanski et al. [89] demonstrated that for mesoporous TiO_2-based cells, gold atoms from the metal electrode diffused through the HTL (spiro-OMeTAD) into the perovskite layer leading to severe losses in efficiency.

You et al. [90] observed etching of the metal electrode (in their case Al) through the complete device, rendering the electrode visible from the backside. Zhao et al. [81] assigned the etching to a redox reaction between Al (or other metals such as Ag, Cr and Yb) and Pb that is enhanced by the presence of moisture. In the case of You et al. [90], replacing the organic PCBM with a ZnO nanoparticle layer proved to detain the reaction, at least for a 10-days storage period in ambient air. Apparently, ZnO is more efficient in isolating the metal electrode from the perovskite. Possible strategies to eliminate this metal-induced device degradation are the use of alternative electrodes, such as carbon or TCOs that do not react with the perovskite, or the introduction of barrier layers that inhibit ion migration [63].

1.3.6 Encapsulation

A proper encapsulation not only protects the solar cells from moisture and oxygen ingress but also prevents volatile decomposition products from diffusing out of the device [91]. Glass-glass encapsulation, a technique commonly used for silicon solar modules [92], is viewed as a promising route for perovskite solar cells as well. In glass-glass encapsulation, the solar cell is sandwiched between two glass plates that are bonded to the cell surface by an encapsulant, most commonly Ethylene-vinyl acetate (EVA). The purpose of the encapsulant is to fill in voids in the package and hold everything firmly together. In some cases, an additional edge seal is used to protect the module from moisture ingress [93]. In addition to encapsulation, the use of protective coatings is frequently investigated. To give two examples, Hwang et al. [94] applied a hydrophobic Teflon layer on top of their cell to minimize moisture ingress, while Bella et al. [95] demonstrated that photopolymer coatings can protect from UV light and humidity simultaneously.

1.4 Stability testing and testing protocols

To allow for a comparison between the stability and degradation of different perovskite photovoltaic devices, and eventually modules, the use of a standardized set of testing protocols is of particular importance. With required lifetimes of up to 25 years it is uneconomical to probe them by real-time in-the-field operation. Therefore, devices are commonly tested under so-called accelerated ageing conditions, i.e. by applying additional stress factors such as elevated temperature or increased humidity [96]. To achieve meaningful lifetime prediction, it is important to know how large the acceleration factor is under the chosen ageing conditions. This, in turn, requires a thorough understanding of the degradation pathways present in the respective solar cell architecture, how they interact with each other and how they couple to measurable solar cell parameters (e.g. V_{oc}, J_{sc}) [30]. Below, a brief overview of standard testing protocols relevant for perovskite solar cells is given, followed by a description of the different routines by which one can monitor device stability. Finally,

ageing test results that exemplify the typical ageing dynamics of perovskite solar cells and the current state in terms of achieved stability are presented.

1.4.1 International testing protocols

To date, there exist two sets of protocols relevant for perovskite solar cells. The first is from the International Electrotechnical Commission (IEC), the second was developed during the international summit on organic photovoltaic stability (ISOS). However, the two protocols greatly differ in terms of sophistication and formal approval and focus on different stages of device development.

The IEC protocols function as an international standard, encompassing photovoltaic characterization, qualification and safety. They have been repeatedly reviewed and fine-tuned by committees composed of international representatives [97]. The protocol on module qualification (IEC 61215) comprises a set of stress tests - such as hail and mechanical load tests, leakage testing, temperature cycling and damp heat testing - all probing the module's stability under conditions that might realistically be encountered in outdoor applications. Most of these protocols are primarily module-related, testing the packaging and encapsulation, and are therefore applicable to all photovoltaic technologies. Passing the IEC qualification test is nowadays almost a prerequisite for solar modules to achieve commercialisation. However, these testing protocols neither provide quantitative acceleration factors nor a well-founded lifetime prediction [30]. The ISOS protocols, on the other hand, only represent a consensus of recommended testing routines (no standard). They were originally developed for organic photovoltaics (OPV) and focus on a much earlier stage of research, aiming to facilitate data comparison between different research groups.

The ISOS protocols provide testing routines for 3 different levels of sophistication and accuracy - Basic, Intermediate and Advanced - to make them applicable for all laboratories. They comprise stability monitoring in the dark, under outdoor conditions and simulated light, as well as thermal cycling and stress testing [96]. Towards the end of this thesis' work, a consensus protocol dedicated specifically to perovskite photovoltaic devices was published. It suggests several complementary stability tests aiming at addressing the special properties of perovskite solar cells, such as the presence of mobile ions in the perovskite or the observations that devices partly recover after the stress factors are removed [91].

1.4.2 Overview of important testing practices

The following section provides an overview of commonly used ways of stability monitoring with references to the above mentioned testing protocols where applicable, some of which will be referred to again in the experimental section of the thesis. The simplest way of monitoring device stability is by storing the cells in the dark (either under inert atmosphere or in ambient air) and periodically performing single measurements of their JV-curves, extracting the most important cell parameters: the power conversion efficiency (PCE), the open-circuit voltage (V_{oc}), the short-circuit current density (J_{sc}) and the fill factor (FF). This is called **shelf life testing** in the ISOS-D-1 protocol (see [96]). Introducing elevated temperatures leads to the so-called **high temperature storage** (ISOS-D-2). The most demanding test is probably the **damp heat test** (ISOS-D-3). It comprises exposure of the cell to a temperature of 85 °C at a RH of 85 %. In order to pass the IEC qualification

protocol, cells have to retain at least 90 % of their initial efficiency when subjected to damp heat (DH) conditions for 1000 h [98]. Another IEC standard test performed in the dark is **thermal cycling** (TC). It involves 200 temperature cycles between −40 °C and +85 °C and its main purpose is to check for delamination caused by a mismatch in thermal expansion coefficients. To pass the test, similar to damp heat testing, the cell's efficiency must not drop by more than 10 % [93].

Closer to the cells' eventual operational conditions are stability tests that monitor the cells under continuous illumination (ISOS-L). If the cells are kept at open circuit with single JV-scans being performed at regular intervals to track their performance, one generally speaks of **light soaking**. This procedure is often employed to investigate light-induced metastable effects within the devices. **Maximum power point (MPP) tracking**, on the other hand, requires that the cells are kept at their maximum power point at all times, thus simulating actual operational conditions [61].

The consensus protocol specifically addressing perovskite solar cells (see above) [91] suggests the following additional stability tests. Due to the partial reversibility of light-induced degradation processes, the performance of light-dark cycling (ISOS-LC) is recommended during which devices should be kept either at open circuit or at MPP. Keeping the cells under electric bias in the dark (ISOS-V) is suggested as a way of separately looking at the impact of electric fields. To be able to better differentiate between degradation modes initiated by ambient air (i.e. oxygen and humidity) and intrinsic processes (e.g. due to the exposure to light, heat or electric fields), the protocol recommends to carry out stability test in an inert atmosphere (e.g. inside a glovebox) as well (ISOS-I).

T_{80} - a figure of merit for solar cell stability

A figure of merit often used to evaluate a solar cell's stability is the time it takes until the cell's efficiency drops below 80 % of its initial value (commonly denoted as T_{80}). Because perovskite solar cells often show a non-uniform degradation behaviour, alternative definitions of the T_{80}-times might be more suitable. Ageing curves of perovskite devices can display all sorts of shapes. Sometimes, a fast initial degradation, often called burn-in, is followed by a much slower decrease (stabilised region). In other cases, the cell's efficiency initially increases until it reaches a maximum and starts to drop. A stabilised T_{80}-value (T_{s80}) can be defined by either extrapolating back to time t = 0 after burn-in and taking the resulting PCE as initial PCE or by using the maximum PCE as a reference value for the T_{80}-time in case of a non-monotonic ageing curve [91].

1.4.3 Ageing behaviour of perovskite solar cells

As mentioned above, ageing curves for perovskite solar cells can have all sorts of shapes depending on the specific device architecture and fabrication process [91]. Moreover, the different options for monitoring cell efficiencies over time, i.e. MPP-tracking or regular JV-scans, were observed to lead to different results.
Due to the hysteresis, efficiencies derived from a JV-scan do not in general coincide with those measured by MPP-tracking. However, two independent research groups [99, 100] demonstrated that, under continuous illumination, the difference between efficiencies derived from regular JV-scans and the values measured by MPP-tracking steadily increases. Monitoring

the stability by JV-scans lead to an overestimation of the PCE. It was assumed that the hysteresis that becomes more pronounced as degradation progresses was a main driver of this effect.

Reversible, metastable behaviour of perovskite solar cells

However, perovskite solar cells do not only exhibit permanent degradation. Several research groups observed reversible (i.e. metastable) effects as a response to illumination. For example, Saliba et al. [99] noticed reversible effects upon MPP-tracking that took different forms depending on the device architecture. Regular n-i-p devices were found to exhibit a steep initial decrease in efficiency under continuous illumination for 150 hours, followed by a more gradual degradation. After a recovering period of several hours in the dark, the cells appeared to regain part of their lost efficiency ("reversible loss"). Inverted p-i-n devices, on the other hand, displayed the inverse behaviour: an initial increase in efficiency under illumination and a loss when recovered in the dark ("reversible bonus").

Another study that revealed reversible degradation behaviour was conducted by Domanski et al. [79] using mesoporous TiO_2-cells. They performed day/night cycling under N_2-atmosphere, i.e. several hours of MPP-tracking followed by a similar period in which the cells are left at open circuit in the dark. Surprisingly, they found that even though the devices lost up to 15 % of their initial efficiency during MPP-tracking, they fully recovered over the dark period. The initial PCE at each cycle was similar to or even higher than the previous one. Domanski et al. attributed this behaviour to migrating cation vacancies that move on a much longer timescale (more than 10^3 s) than halide vacancies that have repeatedly been used to explain hysteresis (see section 1.2.8).

Zhao et al. [101] investigated the light soaking behaviour of inverted perovskite solar cells with PEDOT:PSS as HTL in an inert atmosphere. They found that V_{oc}, FF and PCE significantly improved within 30 min of illumination. J_{sc}-values displayed an initial increase followed by a distinct decrease. By performing several light soaking cycles (each 30 min) with periods of dark storage in between, almost full reversibility could be demonstrated. Zhao et al. ascribed the light soaking effect to a neutralization of interfacial defects and of mainly positively charged bulk defects by photo-generated electrons, the former reducing recombination losses and thereby increasing V_{oc}, while the latter improves charge transport and hence FF. They also found that light soaking reduces bulk polarisation, which might diminish charge dissociation and with it J_{sc}.

Metastabilities in other thin-film photovoltaics

Metastable effects upon illumination have already been observed and investigated in other thin-film photovoltaic technologies, such as CIGS or CdTe-cells. Usually, a reversible increase in fill factor and V_{oc} is observed upon exposure to light [102]. For chalcogenide photovoltaics, the origin of the metastabilities was traced back to point defects present in the absorber material that trap and de-trap photo-generated charge carriers, resulting in lattice relaxations and changes in the built-in field and the number of recombination centres present [103]. Generally, such metastable effects are undesirable because they hamper and complicate a reliable energy rating of the photovoltaic cells [104].

State of the art: Achievements in device stability

It has already been demonstrated that properly encapsulated perovskite solar cells can withstand standard accelerated ageing tests, such as temperature cycling (TC) or damp heat (DH) testing, both part of the IEC qualification protocols [105, 106]. PSCs encapsulated between two glass sheets with the polymer EVA and a butyl rubber edge seal were shown to not only withstand damp heat testing, but even improve throughout the 1000 h. The device architecture was of the p-i-n type with NiO_x as HTL, and LiF followed by PCBM as ETL [105]. However, yellowing of the perovskite was noticeable after the 1000-hour period, indicating that the package might have failed eventually [93].

Cheacharoen et al. [106] performed temperature cycling (TC) tests on sealed perovskite solar cells of the same architecture, comparing two encapsulants with different elastic moduli, the stiff ionomer Surlyn and the softer ethylene vinyl acetate (EVA). While 4 out of 5 cells encapsulated with Surlyn failed the test, probably due to partial delamination, all 9 cells encapsulated with the softer EVA passed successfully. Measuring the fracture energies of the separate layers in the solar stack, they furthermore found that PCBM was the weakest layer and most susceptible to delamination, even with encapsulation. In a subsequent study [93], the encapsulation design and method was further improved. EVA as an encapsulant was replaced by polyolefin, because EVA is known to decompose into acetic acid in damp heat conditions [107], which in turn could react with the perovskite and lead to its degradation. For polyolefin, no chemical reactions with the perovskite could be observed and cells protected by this optimized encapsulation withstood both thermal cycling and damp heat testing, the latter with an average drop in efficiency by only 1 %.

1.5 Challenges for perovskite solar cells: A summary

Perovskite solar cells have a huge potential due to their low-cost and low-temperature processability, paired with the high power conversion efficiencies - the current record exceeds 25 % - that can be achieved. However, serious challenges are faced in terms of device stability. As was described in section 1.3, perovskite solar cells were observed to degrade when exposed to external factors such as oxygen, humidity, light, heat and electric fields. Internal mechanisms, such as ion migration and chemical reactions at the interfaces, can also have a large impact on device stability. Therefore, the choice of transport layers and electrode materials can play an important role in mitigating degradation effects. But not all induced changes are irreversible. Several research groups [17, 79, 81, 99, 101] observed metastable behaviours in perovskite solar cells upon exposure to light or moisture. After removal of the stressor, the induced changes were partly or fully reversed. Although a few research groups have already succeeded in developing perovskite solar cells with device architectures and encapsulations stable enough to withstand standard IEC stability tests, such as damp heat testing and temperature cycling, degradation mechanisms and the influence of material choices still lack thorough understanding.

1.6 Aim of this thesis

The aim of this thesis was to investigate the degradation and stability of inverted p-i-n perovskite solar cells by measuring the cells' response to different external stressors such as oxygen, light and moisture. The first step on the way to testing the device stability was the fabrication of the devices themselves. Promising synthesis routes were adopted from literature and then further optimised in order to achieve solar cells with good and reproducible efficiencies. Synthesis was performed for two different device architectures, one with an organic hole transport layer (PEDOT:PSS) and one with an inorganic one (Cs-doped NiO_x). Several characterisation techniques, such as XRD, SEM, EBIC or profilometry, have been employed to examine crystal structures, microstructures, spatial cell performances or layer thicknesses and support the optimisation of the photovoltaic devices. After the synthesis, the stability of the cells was evaluated by using several different stability testing procedures: shelf life testing, light soaking, MPP-tracking and damp heat testing. A special focus was put on the stability of the cells towards illumination. Exposure to light was investigated in different atmospheres (nitrogen and ambient) and for encapsulated devices to gain a better understanding of the interplay of permanent degradation and metastable changes. Cells with PEDOT:PSS and NiO_x as hole transport layers were compared in terms of their stability behaviour, both to determine whether NiO_x can be a possible substitute for the organic PEDOT:PSS and to investigate how the choice of hole transport layer, in general, influences the stability of the cells.

Chapter 2

Experimental Methods

The following section describes the experimental methods used within this thesis together with important arguments as to why a particular material, method or set of parameters was chosen. The first part addresses the synthesis and assembly of the solar cell devices, while the rest of the section is dedicated to the description of used measurement techniques and technical equipment.

2.1 Synthesis of perovskite solar cells

2.1.1 Choice of device architecture

For the scope of this thesis the inverted, planar p-i-n architecture (see Fig. 1.3c) was chosen, primarily due to its easier processability compared to regular n-i-p devices. The device architecture comprised the following sequence of layers:

glass substrate/ITO/HTL/perovskite/ETL/Ag

For the HTL, two different materials, one organic and one inorganic, were used and compared with respect to cell performance and stability. The organic material was PEDOT:PSS, partly diluted with either DMSO or 2-propanol, the inorganic one Cs-doped NiO_x, prepared from a sol-gel method. $PC_{60}BM$ was chosen as the electron transport layer (ETL), in combination with an additional, protective layer of ZnO nanoparticles. The cell architecture and the process parameters (see section 2.1.4) were largely adopted from Weber et al. [108].

Choice of hole transport layer

In the inverted architecture, the HTL lies beneath the perovskite layer. It therefore needs to resist solvation by the solvents used for the perovskite precursor. It furthermore must be transparent enough to allow irradiation of the perovskite through the HTL when operating the cell [109].

PEDOT:PSS, a highly conducting aqueous polymer dispersion, is a popular hole transporting material that is widely used especially in organic solar cells. The high conductivity

is achieved by doping PEDOT, a semiconducting polymer, with the electrolytic PSS. In addition to its function as dopant, PSS ensures the water-solubility of PEDOT [110]. DMSO as an additive to PEDOT:PSS was shown to increase the conductivity of the PEDOT:PSS layer [111, 112] and enhance perovskite crystal growth [113].

NiO_x represents another potential candidate for the hole extraction layer. It is especially attractive due to its chemical stability and its good hole conductivity [114]. Furthermore, NiO_x is highly transparent due to its wide band gap of 3.5–3.9 eV [109] and has a large work function that can range from 4.7 to 5.5 eV depending on processing parameters [114]. NiO_x generally occurs in a non-stoichiometric compound. While stoichiometric NiO is insulating, an excess in oxygen leads to nickel vacancies V_{Ni} that give rise to p-type conductivity. However, V_{Ni}-states are too far away from the valence band maximum (VBM) to have most of the vacancies ionised at room temperature. Introducing extrinsic impurities as dopants can considerably increase the density of free holes [115]. Chen et al. [114] showed that doping NiO_x with Cs significantly improves the cell performance. They measured a better hole-conductivity and a larger work function, the latter resulting in higher V_{oc}-values. To form an HTL, NiO_x can either be processed by a simple sol-gel solution-based method or prepared from pre-synthesized NiO_x nanoparticles [116]. Seo et al. [116] investigated the relationship between sol-gel NiO_x film thickness, annealing temperature and different solar cell parameters (PCE,V_{OC},FF,J_{SC}) and found that films with 15 nm thickness, achieved with a 0.1 M percursor solution and spin-coating at 3000 rpm for 40 s and subsequent annealing at 350 °C, yield the best performances. Tang et al. [117] compared cells with PEDOT:PSS and NiO_x nanocrystals as HTL. Their studies showed that NiO_x was superior both in terms of cell performance and stability. When exposed to 60-80 % relative humidity (RH) in air for over 90 hours, cells with NiO_x only lost about 30 % of their initial efficiency, while those with PEDOT:PSS degraded completely [117].

Choice of electron transport layers

A double ETL consisting of PCBM followed by a ZnO nanoparticle layer was chosen for the device architecture, since the complementary properties of the two materials lead to an improved device performance. PCBM was demonstrated to reduce the surface roughness by filling the gaps in the underlying perovskite layer [118]. This is important to achieve a closed, smooth electrode layer [118]. Additionally, it was shown that PCBM successfully passivates trap states, thus reducing surface carrier recombination [119]. However, PCBM alone cannot prevent the reaction between the electrode and the perovskite which is detrimental to device performance. The diffusion of perovskite across the PCBM layer into the electrode was demonstrated by Qiu et al. [118] via SIMS measurements. However, an additional thin film of ZnO nanoparticles works. The ZnO efficiently functions as a physical barrier, prohibiting any reaction between the electrode and the perovskite [118]. Moreover, ZnO has a large enough energy band gap to provide efficient hole blocking, which leads to an improved carrier selectivity compared to PCBM [120].

2.1.2 Used materials

A list of the chemicals used for the solar cell fabrication can be found in the Table 2.1 below. For PEDOT:PSS and the ZnO nanoparticle layer, ready-made solutions were purchased from

the manufacturers listed in the table. For the other materials, the perovskite, NiO_x and $PC_{60}BM$, precursor solutions were prepared as described below (section 2.1.4).

Table 2.1: List of chemicals used for this thesis.

Chemical	Manufacturer	Purity / %
Acetone	Sigma-Aldrich	-
2-propanol	Roth	$\geq$ 99.8
Chlorobenzene	Sigma-Aldrich	99.8
Clevios P VP AI 4083	Heraeus	-
Cs acetate	Sigma-Aldrich	$\geq$ 95
CsI	Sigma Aldrich	99.999
DMF	Sigma-Aldrich	$\geq$ 99.8
DMSO	Sigma-Aldrich	$\leq$ 0.02 % water
E132 PV & LED Encapsulation Epoxy	Ossila	-
ETA	Fluka Analytical	-
FAI	DyeSol	-
MABr	DyeSol	-
MaBr	TCI	$\geq$ 98.0
Ni(II) acetate tetryhydrate	Aldrich	$\geq$ 99.0
PbI_2	TCI	99.99
$PbBr_2$	Sigma Aldrich	99.999
$PC_{60}BM$	Solenne	99.5
Plus Sofortfest 2-component epoxy glue (62981)	UHU	-
ZnO nanoparticle ink	Sigma-Aldrich	

2.1.3 Deposition techniques

Almost all layers, namely PEDOT:PSS, NiO_x, perovskite, $PC_{60}BM$ and the ZnO nanoparticle layer, were deposited via spin-coating. For the silver top electrode, thermal evaporation was used. The deposition of the perovskite was performed in a one-step process. For this method, the perovskite is spin-coated directly from a single precursor solution and an anti-solvent step is carried out towards the end of the spin-coating process to induce crystallisation. During the anti-solvent step, a liquid that is a bad solvent for the perovskite (i.e. an anti-solvent) is dripped onto the spinning sample. The anti-solvent drastically reduces the solubility of the perovskite in the solvent and thus speeds up nucleation and crystal growth [121]. For this thesis, chlorobenzene was used as an anti-solvent. The one-step deposition process is faster and less cost-intensive than the other existing deposition methods, namely vapour deposition or a two-step sequential deposition technique [121]. In the two-step deposition method, a layer of PbI_2 is formed that is subsequently converted to $MAPbI_3$ by dipping it into a solution of MAI [122].

2.1.4 Solar cell assembly

The fabrication of the cells comprised the following steps:

1. Preparation of ITO-substrates
2. Preparation of PEDOT:PSS films
3. Preparation of perovskite films
4. Preparation of PCBM films
5. ZnO nanoparticle layers
6. Evaporation of silver electrodes

Preparation of ITO-substrates

For the solar cell fabrication ITO patterned glass substrates of the size 15x15 mm (15 Ω/sq) by Lumtec Corp. were used. After rinsing them with acetone and drying them in a N_2-air stream, the substrates were placed in a 2-propanol bath and subjected to 20 min of ultrasonic cleaning at 40 °C. Subsequent drying of the substrates was again performed with a N_2-air stream. The samples were then exposed to a 3-minute O_2-plasma etching treatment to increase the surface polarity and the wettability of ITO. This facilitates the subsequent spin-coating of the HTL [123].

Preparation of HTLs

PEDOT:PSS was used partly undiluted, partly diluted with DMSO (5 % and 10 % v—v) or 2-propanol (ratio 1:2). To ensure good mixing the diluted solutions were placed in an ultrasonic bath for 1 hour at 40 °C, then filtered with a Chromafil Xtra 0.45 μm PVDF filter by Macherey-Nagel. The PEDOT:PSS solution was spin-coated onto the substrates at 3000 rpm (1000 rpm/s) for 60 s, applying 40 μl per sample. Afterwards the substrates were transferred into a N_2-filled glovebox, where all further process steps were carried out. To remove any remaining solvent from the PEDOT:PSS film, the substrates were placed on a hot plate at 120 °C for 20 minutes.

The NiO_x films were prepared from a sol-gel process adopted from Chen et al. [114]. The precursor solution consisted of 0.1 M nickel acetate and 0.1 M ethanolamine dissolved in 2-propanol. 1 mM caesium acetate was added to the mixture to achieve 1 % Cs-doping. The precursor solution was stirred at 70 °C overnight in the course of which its colour changes from blue to green. Preparation of the NiO_x films took place via spin coating. 40 μl of the precursor solution were applied to the ITO-substrates and spun at 3000 rpm for 30 s. Afterwards, the films were annealed at 275 °C for 1 hour in a furnace.

Preparation of perovskite films

The perovskite precursor solution was prepared under nitrogen atmosphere the day before and continuously stirred overnight. The composition
$(Cs_{0.08}(MA_{0.17}FA_{0.83})_{0.92}Pb(I_{0.83}Br_{0.17})_3)$ was adopted from Weber et al. [108]. Lead iodide (PbI_2, 1.1 M), formamidinium iodide (FAI, 1 M), lead bromide ($PbBr_2$, 0.2 M) and

methylammonium bromide ($MABr$, 0.2 M) were dissolved in a mixture of DMF:DMSO with a volume ratio of 1:4. Because CsI does not readily dissolve in DMF [124], a solution of caesium iodide (CsI, 1.5 M) in DMSO was prepared separately and subsequently added to the first solution so as to achieve the desired caesium content of 8 %. Before spin-coating the precursor solution was filtered with a Chromafil Xtra 0.45 μm PVDF filter. Used spin-coating parameters were 10 s at 1000 rpm (500 rpm/s) followed by 20 s at 6000 rpm (1200 rpm/s). Per substrate 50 μl of precursor solution were used. During the last 5 s of spinning an anti-solvent treatment with 50 μl chlorobenzene was performed. The perovskite films were then annealed on a hot plate at 100 °C for 1 hour to evaporate any remaining solvents and to further advance crystallisation.

Preparation of PCBM films

Similarly to the perovskite precursor solution, the PCBM solution was prepared the day before, under nitrogen atmosphere, and stirred overnight. It consisted of 20 mg/ml PCBM in chlorobenzene. Prior to film preparation the PCBM solution was filtered with a Chromafil Xtra 0.45 μm PVDF filter. Afterwards, it was spin-coated on top of the perovskite layer at 2000 rpm (500 rpm/s) for 60 s, applying 30 μl per substrate.

ZnO nanoparticle layers

The ZnO layer was prepared from a ready-made ZnO nanoparticle ink, purchased from Sigma Aldrich. 40 μl were applied to each sample and spin coated at 3000 rpm (1000 rpm/s) for 30 s.

Evaporation of silver electrodes To contact the ITO-electrode, two small areas were freed from the superjacent layers using a Stanley knife and a mask. The substrates were then placed into an evaporation chamber, where silver electrodes of 120 nm thickness were deposited under high vacuum conditions (10^{-5} mbar) employing a shadow mask.

2.2 Thin film and solar cell characterisation methods

The fabricated solar cells were examined using a variety of characterisation methods to gain information of both their electrical and structural properties. This section provides an overview of the characterisation techniques employed within the scope of this thesis. The fundamental principles underlying the respective methods are briefly explained and the choice of measurement parameters is discussed, whenever relevant. A list of the measuring instruments and equipment used for this thesis can be found in the appendix A.

2.2.1 Current density-voltage (JV) characterisation

Current density-voltage measurements (or for short: JV-scans) are a standard characterisation method for photovoltaic cells. The current generated within the device per cell area is measured as a function of voltage. If the scan is performed in the dark, a curve identical in shape to that of a diode is obtained. If the cell is illuminated, a photocurrent of opposite polarisation is generated that shifts the curve along the current-axis [125]. One usually refers

to measurements performed under these two lighting conditions as dark and light JV-curve respectively. From the light JV-curve, the following solar cell parameters can be extracted: the power conversion efficiency (PCE), the open-circuit voltage (V_{oc}), the short-circuit current density (J_{sc}), the fill factor (FF), as well as voltage and current at the maximum power point (MPP). For this thesis, JV-scans were performed both at the TU Graz and at the AIT in Vienna. In Graz, a Keithley 2400 source meter controlled by a Labview-based program was used for the measurements. In Vienna, a LXI 2651A High Power System source meter connected with the commercial software 'IV Rider'.

Light sources

The irradiance spectrum of the light source used to illuminate the solar cells greatly influences the achieved efficiencies. To measure in standard conditions, a 'solar simulator' is required whose spectrum is as close as possible to the AM1.5 solar spectrum [125]. For the measurements in Graz, a HMI lamp by Dedolight (see appendix A) with an irradiance of 100 mW/cm^2 was used for illumination of the samples. In Vienna, a Trisol^{TM} Class AAA Standard Solar Simulator by OAI served as a light source. It is based on a 1.8 kW Xenon lamp. The spectra of the two illumination sources are depicted in Figure 2.1 together with the AM1.5 solar spectrum as defined by the international standard IEC 60904:3.

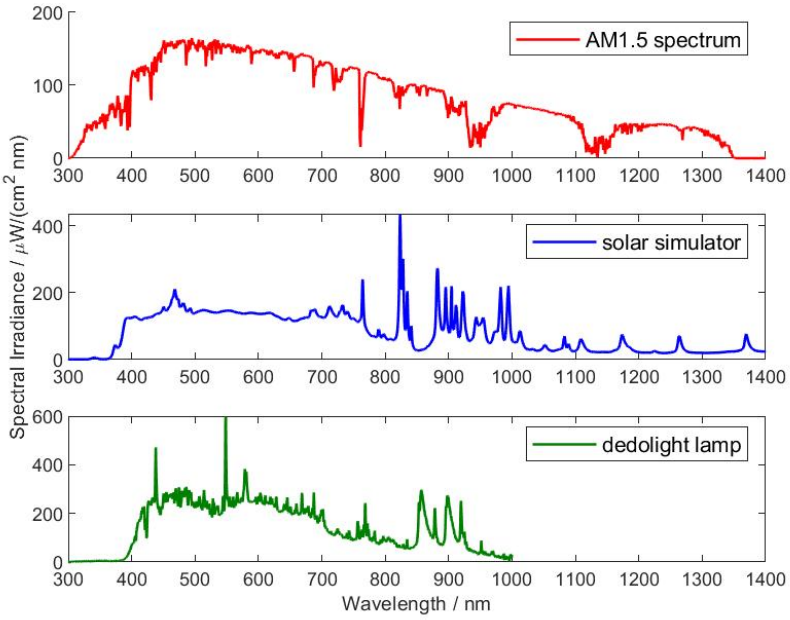

Figure 2.1: Spectra of light sources used for JV characterisation together with the AM1.5 solar spectrum as defined by IEC60904-3.

Measurement parameters

As discussed in section 1.2.8 on hysteretic effects, the choice of measurements parameters, i.e. scan speed and scan direction, affects the shape of the resulting JV-curve. In general, slower scan rates were shown to reduce hysteresis and achieve results closer to the steady state. The scan range plays a role, too. Starting reverse scans at a bias significantly larger than the V_{oc} of the cell can lead to considerable measurement errors that make the cells look more efficient than they actually are [126]. The opposite effect was observed by Wei et al. [58] for scans in forward direction. If the measurement was started at a higher reverse bias, the resulting JV-curve exhibited a reduced FF and PCE. Due to these observations, a narrow scan range was chosen for this thesis' JV-measurements, restricting the voltage sweeps to values between -0.02 V and +1 V (+1.2 V) for cells with PEDOT:PSS (NiO_x) as HTL. Different scan speeds were used throughout the thesis and are specified together with the results. On the whole, a trade-off had to be made between achieving measurements close to steady-state and avoiding changes in the solar cell due to the prolonged illumination that comes with a slower scan rate.

2.2.2 External Quantum Efficiency (EQE)

This characterisation technique, also known as 'incident photon conversion efficiency (IPCE)' or 'spectral response', provides the performance of a short-circuited solar cell as a function of wavelength of the incident light. During measurement, the cell is irradiated by monochromatic light of different wavelengths and the respective conversion efficiencies are calculated from the measured current output and the incident photon flux. An EQE spectrum sheds light on which parts of the solar spectrum actually contribute to current generation and which do not [125]. For perovskite solar cells, the responsive part of the spectrum lies between 300 and 800 nm (see [126]). However, with the apparatus used for this thesis, a 75 W Xenon lamp combined with a MuLTImode4-AT grating monochromator by AMKO, only a range from 380 to 800 nm could be accessed. The incident photon flux was measured by a Newport 818-UV photodiode, the current by a Keithley 2400 source meter. Because the EQE measurements had to be performed outside the glovebox, the solar cells were placed into a sealed measurement unit. Although probably not perfectly impermeable, the box should have provided decent protection from oxygen and moisture over the measurement time. During the EQE measurements, the cells were only illuminated by the monochromatic light beam without any background illumination to avoid unnecessary exposure of the cells to light that might accelerate degradation.

2.2.3 Scanning electron microscope (SEM)

SEM represents a microscopic setup that uses a highly focused beam of electrons for the image generation. During imaging, the electron beam continuously scans across the sample surface and a detector measures the secondary electrons that are produced by the high energy beam. The gathered data is then used to calculate a grey-scale image [127]. For the SEM images taken within this thesis, acceleration voltages between 2-5 kV were used. The instrument was a SUPRA 40 scanning electron microscope by ZEISS.

2.2.4 Electron beam-induced current (EBIC)

An EBIC measurements allows to investigate the spatial dependence of the cell's efficiency. An electron beam (e.g. from a scanning electron microscope (SEM)) is used to scan the surface of the cell. Similar to photons, the incident electrons generate electron-hole pairs within the perovskite layer that are then separated by the solar cell architecture, leading to a measurable current. By scanning across the cell's surface, a 2D image is created that shows where current is generated and how efficiently. The penetration depth of the electron beam is determined by the acceleration voltage [50] and the atomic number of the sample [127]. For the EBIC measurements performed within this thesis' work, a Jeol 6490LV scanning electron microscope was used with an acceleration voltage of 30 kV. The solar cells were contacted with manipulators inside the SEM chamber. To check if good electric contact was achieved, JV-curves were measured with a Keithley 2600 Series source meter. The EBIC was run via an ADwin-Pro II Data Acquisition System with a SR570 Low noise current pre-amplifier. The measurements were controlled by a Python-based software.

2.2.5 X-ray diffraction (XRD)

X-ray diffraction allows the examination of a sample's crystal structure via elastic scattering of x-rays. If the atoms in the sample are arranged in a periodic lattice, constructive interference takes place whenever Laue's condition is fulfilled.

$$\Delta\vec{k} = \vec{G} \tag{2.1}$$

where $\Delta\vec{k}$ represents difference between the incident and the scattered wave vector and $\vec{G}$ is a reciprocal lattice vector. From the Laue condition, one can obtain the angle 2θ at which constructive interference can be observed [128].

$$sin\theta = \frac{|\vec{G}|}{2|\vec{k}|} \tag{2.2}$$

For this thesis, XRD measurements were performed both at the TU Graz using a Rigaku MiniFlex powder XRD instrument and at the AIT in Vienna with a ARL^{TM} EQUINOX 100 X-ray Diffractometer by ThermoScientific. The sample area irradiated by the x-ray beam was 10x20 mm for the Rigaku instrument and 2.3x1 mm for the ThermoScientific setup. Thus, the Rigaku captured the whole substrate surface while the ThermoScientific could be focused approximately on 1 specific cell. For the ThermoScientific instrument, the scan time was 5 min. For the Rigaku setup, the chosen measurement parameters were 0.01 °/step and 10-20 °/min.

2.2.6 X-ray reflectivity (XRR)

Contrary to XRD, x-ray reflectivity measurements are not restricted to crystalline samples. Structural thin-film parameters, such as film thickness, roughness and electron density, are derived from the intensity curve of the specularly reflected beam at grazing incident angles. As the incident angle surpasses the critical angle for total reflection, part of the beam penetrates the sample by refraction. The x-rays reflected from the sample surface and the

interface between thin film and substrate undergo interference leading to a detector signal that oscillates as a function of angle (so-called Kiessing fringes). The film thickness can be determined from the period of these oscillations [129]. The XRR measurements were performed with a Panalytical EMPYREAN x-ray diffractometer.

2.2.7 Stylus profilometry

In profilometry, the sample surface is scanned by a diamond tip that is kept in contact with the surface at a constant contact force. The resulting profile can be used to determine surface roughness [130]. A commonly used measure for surface roughness is the root mean-square roughness R_q.

$$R_q = \sqrt{\frac{1}{n}\sum_{i=1}^{n} y_i^2} \tag{2.3}$$

where y_i is the distance from the average surface height and n the total number of measuring points [131]. Stylus profilometry can also be applied to measure film thicknesses. For this purpose, a penetrating scratch is inflicted on the film across which a line scan is performed. For this thesis, a DektakXT device by Bruker was used.

2.3 Data analysis

The collected data was processed and analysed by use of MATLAB and Microsoft Office Excel, as well as evaluation software supplied by the instrument manufacturers. For the interpretation of the XRD measurements, the open source programme Fityk was used to perform baseline subtraction and fit the peaks with Pseudo-Voigt functions to get the peak parameters (position, height, area and full-width-half-maximum (FWHM)). To calculate the J_{sc} from the EQE data, a website tool (https://opvap.com/eqe.php) was used.

2.3.1 Reproducibility and statistical relevance of the results

Since this thesis was laid out as rather broad, exploratory study of stability-related effects in perovskite solar cells, and therefore the responses to several different external factors for different device architectures have been investigated, the restricted time did not allow for a sufficient check of reproducibility. For most ageing experiments, only one cell has been measured per type of hole transport layer and ageing condition. In order to verify the obtained results and enable a statistical analysis, the corresponding measurements have to be repeated for several comparable cells of the same architecture. Unless this has been done, conclusions can be drawn only with great caution, while keeping in mind that a single cell does not necessarily display the average behaviour of a large number of equivalent cells.

Chapter 3

Synthesis, optimisation and device characterisation

3.1 Introduction

This section contains all results that concern the fabrication process, as well as general device characterisation. In the first part (section 3.2), steps that were performed to optimise the synthesis route are presented, followed by results demonstrating the effect that the underlying hole transport layer (section 3.3) and the anti-solvent step (section 3.4) have on the perovskite film formation. Attempts to protect the solar cell devices from oxygen and humidity by encapsulating them are discussed in section 3.5. The last section (3.6) deals with the general characterisation of the fabricated devices. Achieved power conversion efficiencies and their reproducibility are discussed, and results that are useful to better understand the solar cell setup (such as layer thicknesses) and the properties of the used materials (such as XRD peak identification) are presented. Last but not least, a few comments are made on the presence and effect of hysteresis.

3.2 Optimisation of the synthesis route

Even though the optimisation of the solar cell synthesis route was not the main objective of this thesis, certain steps had to be performed in order to achieve decent device efficiencies with an acceptable degree of reproducibility that could the be used to perform stability experiments. For this thesis, two different hole transport layers (HTLs) were implemented in the solar cell architecture: the organic PEDOT:PSS and the inorganic NiO_x. Since NiO_x has only been introduced after satisfying results had been achieved with PEDOT:PSS, most optimisation efforts were directed towards the organic HTL. Below, an overview over the performed optimisation steps is given.

3.2.1 Optimisation of PEDOT:PSS

PEDOT:PSS is a standard hole transport material, commonly implemented in inverted perovskite solar cells. To increase its conductivity, different additives have already been successfully used in literature [108,111,112]. Two of them, 2-propanol and DMSO were also tested within this thesis. Diluting PEDOT:PSS with 2-propanol resulted in a bad wettability of the HTL, which was why this approach was abandoned after the first test batch. Adding DMSO (in volume ratios of 5 and 10 %) lead to significantly higher J_{sc}-values, and thus improved efficiencies, as can be seen in Table 3.1. However, issues regarding film homogeneity were encountered in later batches. Part of the samples exhibited non-uniform coverage after spin-coating, with holes in the PEDOT:PSS layer. This resulted in a high percentage of non-working solar cells (see Table 3.5), and thus reduced reproducibility. A possible explanation for the non-uniform film formation could be the separation of an insulating, transparent PSS phase from the PEDOT:PSS phase, as was observed by Ouyang et al. [110] for air-dried PEDOT:PSS films with varying volume ratios of DMSO. They suggested that the DMSO-induced separation of PSS results in a more compact packing of the remaining PEDOT:PSS network, thus leading to enhanced conductivity. By using only 5 % v/v DMSO, phase separation could be kept at a minimum (88-90 % PEDOT:PSS area ratio after air-drying), whilst still achieving a significant increase in conductivity. However, this presumed origin of the problem could not be confirmed experimentally within this thesis' work, nor could it be eliminated. It was attempted, without success, to get rid of the inhomogeneities in the PEDOT:PSS layer by reducing the amount of DMSO from 10 % to 5 % (based on the findings by Ouyang et al. [110] described above) and by double-checking for possible sources of contamination (e.g. dust particles). Holes in the spin-coated films still appeared in some samples, while they did not occur in others. For this reason, most ageing measurements were only performed for cells with pure PEDOT:PSS, despite its lower cell efficiency.

Table 3.1: Average solar cell parameters for devices with PEDOT:PSS with no or 10 % DMSO added. Only cells with PCE > 1 % were considered for the averages (i.e. 36 cells with pure PEDOT:PSS and 43 cells with DMSO), the rest was categorized as failures.

amount of DMSO	PCE / %	V_{oc} / V	J_{sc} / mA/cm^2	FF	failure / %
none	5.1 ± 1.3	0.73 ± 0.08	14.1 ± 2.1	0.49 ± 0.10	14.3
10 %	6.4 ± 1.6	0.73 ± 0.10	17.6 ± 1.3	0.47 ± 0.10	10.4

3.2.2 Optimisation of NiO_x

At first, the NiO_x layers were annealed on a hot plate at 275 °C in ambient air. However, this resulted in very poor results. More than two thirds of the thus fabricated cells had PCE-values below 1 % and the fill factors were extremely low (see Table 3.2). A low fill factor is usually caused by very high series resistances. Performing the annealing step inside a furnace at the same temperature significantly improved the results and led to an increase in both J_{sc} and FF and a much lower failure percentage. This suggests that the samples

were not homogeneously heated on the hot plate due to a temperature gradient forming between the plate surface and the surrounding air, and hence did not reach the temperature required for a conductive NiO_x film to form. The furnace, however, provided homogeneous heating of the sample from all sides.

Table 3.2: Average solar cell parameters for devices with NiO_x as HTL, annealed on a hot plate and in the furnace. Only cells with PCE > 1 % were considered for the averages (i.e. 27 cells that were annealed on the hot plate and 87 cells in the furnace), the rest was categorized as failures.

NiO_x annealing	PCE / %	V_{oc} / V	J_{sc} / mA/cm^2	FF	failure / %
hot plate	4.7 ± 2.4	1.00 ± 0.08	14.6 ± 3.9	0.31 ± 0.09	67.9
furnace	10.1 ± 3.5	0.91 ± 0.14	20.5 ± 2.7	0.52 ± 0.11	9.4

3.2.3 Introduction of ZnO nanoparticle layer

As described in section 2.1.1, the introduction of a ZnO nanoparticle layer on top of the organic ETL $PC_{60}BM$ was found to inhibit the diffusion of electrode atoms into the perovskite and vice versa. To investigate the effect of ZnO, a batch was fabricated where half of the solar cells incorporated a ZnO nanoparticle layer and half of them only featured $PC_{60}BM$. The resulting average solar cell parameters are listed in Table 3.3 and clearly show the beneficial effect of ZnO. Cells featuring a double ETL of $PC_{60}BM$ and ZnO achieve a higher PCE, V_{oc}, J_{sc} and FF. The increase in J_{sc} and FF could indicate improved conductivity and charge extraction. The increase in V_{oc} could be due to a decrease in charge recombination at the perovskite/ETL interface.

Table 3.3: Average solar cell parameters for devices with and without an additional ZnO nanoparticle layer. As HTL PEDOT:PSS with 10 % DMSO was used. Only cells with PCE > 1 % were considered for the averages (i.e. 29 cells without ZnO, and 36 cells with ZnO), the rest was categorized as failures.

ETL	PCE / %	V_{oc} / V	J_{sc} / mA/cm^2	FF	failure / %
PCBM	4.3 ± 3.3	0.64 ± 0.21	13.0 ± 1.4	0.44 ± 0.20	3.3
PCBM+ZnO	9.9 ± 3.1	0.81 ± 0.12	17.4 ± 1.3	0.67 ± 0.15	0.0

3.3 Perovskite growth on top of different HTLs

SEM images of perovskite films grown on top of different HTLs (pure PEDOT:PSS, PEDOT:PSS + 5 % DMSO and NiO_x) were taken in order to compare film homogeneity and crystallite sizes (see Fig. 3.1). In general, all three films look quite homogeneous, although there are some pinholes visible in the one grown on NiO_x. This might, however, be due to the fact that the examined sample was one for which the NiO_x annealing process had not

yet been optimized. The NiO_x film had been annealed on a hot plate, which resulted in bad wettability for the perovskite precursor. Performing the annealing step in a furnace, where the samples are more homogeneously heated, resolved this issue. One could presume that the perovskite films grown on top of the thus annealed NiO_x films should therefore exhibit less pinholes. However, the correlation between perovskite film coverage and NiO_x annealing method remains to be properly investigated.

In terms of grain size, no difference is discernible between the films grown on pure PEDOT:PSS and those deposited on PEDOT:PSS with 5 % DMSO added. This is in contradiction to the results published by Adam et al. [113], who observed that DMSO as an additive greatly enhanced crystal growth. However, a different type of PEDOT:PSS solution (PH1000, instead of AI4083) was used, which might explain the different results. Compared to the HTLs based on PEDOT:PSS, perovskite growth on NiO_x appears to result in slightly larger grains. Grain sizes range from around 130-300 nm.

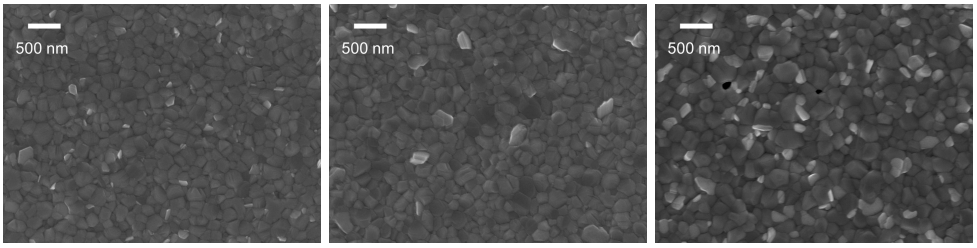

(a) PEDOT:PSS (5 % DMSO) (b) PEDOT:PSS (c) NiO_x

Figure 3.1: SEM images of perovskite layers grown on different HTLs.

3.4 Spatial uniformity of solar cell performance

Highly efficient and reproducible solar cells should exhibit uniform layers that yield the same PCE in all areas. To investigate whether this prerequisite was fulfilled for the cells synthesised within this thesis, EBIC images of the active cell areas were taken. They revealed that the EBIC signal was far from homogeneous. Small areas of a large current response were surrounded by regions where only a comparatively small current could be extracted. Apparently, only small parts of the cells yield high efficiency, thus limiting the total cell efficiency. Figure 3.2 shows EBIC images of 4 nitrogen-stored cells with PEDOT:PSS as HTL that were all located on the same substrate. Their relative positioning in the figure roughly corresponds to their actual position on the square substrate. Areas with a large EBIC response are shaded in red, those giving a small signal in blue. The different regions form circular shapes and structures, indicating that the inhomogeneity might be a result of solution processing (i.e. spin coating and anti-solvent dripping).

A closer investigation of the circular line rendering a high EBIC signal in the cell on the lower right via profilometry (see Figure 3.3) reveals a variation in cell thickness. Whether the high-efficiency circular line corresponds to a thicker region and in which layer the thickness variation takes place cannot be deduced from the measurement. Further investigation, such

as cross sectional SEM analysis, would be necessary.

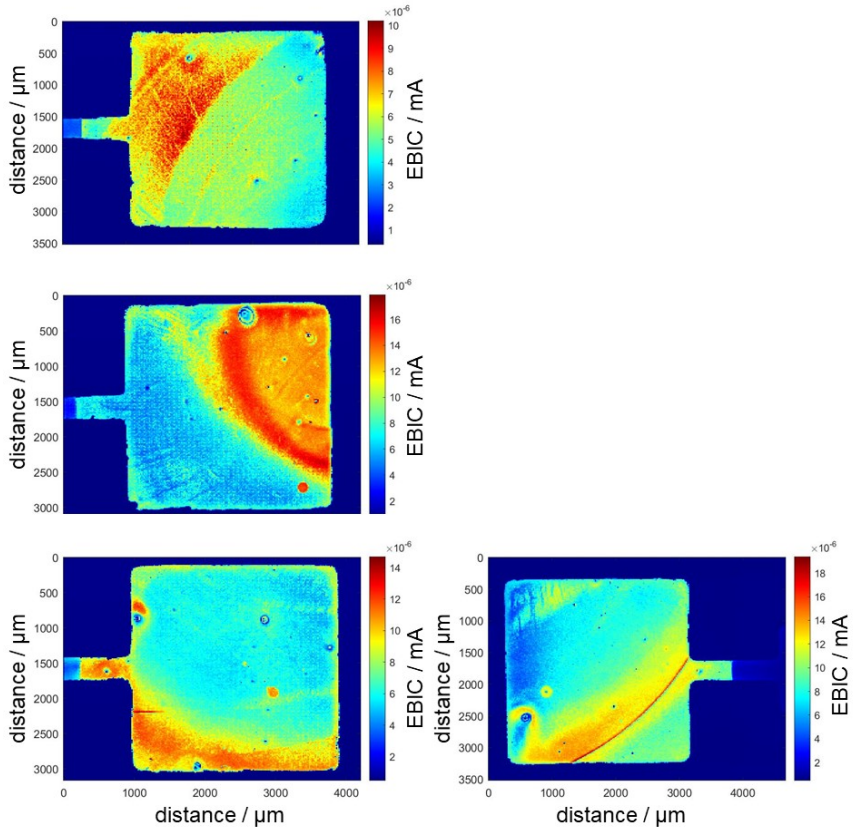

Figure 3.2: EBIC images of 4 cells on the same substrate. During spin coating, 50 μl CB were applied. HTL: PEDOT:PSS. Positioning corresponds roughly to actual position on the square substrate.

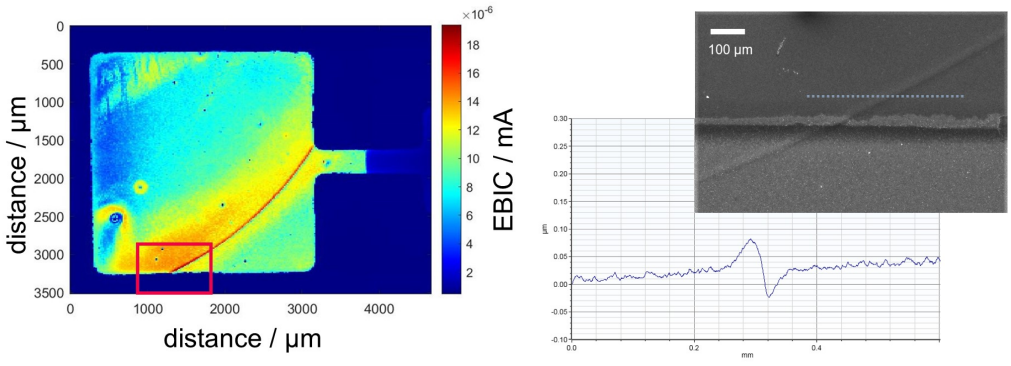

(a) (b)

Figure 3.3: More detailed investigation of circular line rendering a high EBIC signal. (a) EBIC image: black rectangle indicates the segment displayed in (b) SEM image showing part of the circular line together with a profilometer scan measured along the dashed line.

3.4.1 Effect of anti-solvent dripping on the perovskite layer

To shed light on the influence of anti-solvent dripping on homogeneity, three perovskite films on glass substrates with varying amounts (0, 25 and 50 μl) of the anti-solvent CB applied were fabricated. The reduction or omission of anti-solvent lead to a huge difference in surface morphology that was clearly visible with the naked eye (see Fig. 3.4). While the perovskite film that was processed with 50 μl CB was shiny and reflective, the other two films with 0 and 25 μl CB had a dull, rough surface. In addition, holding the samples against the light revealed a bad film coverage in the latter. Light was able to shine through many small holes in the sample. The application of anti-solvent during spin coating indeed seems to have a large impact on the crystallisation behaviour of the perovskite. Table 3.4 lists the average

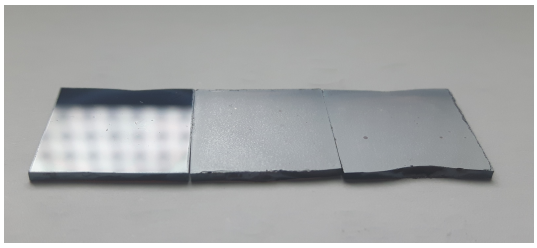

Figure 3.4: Difference in surface roughness for perovskite films fabricated using different amounts of anti-solvent. Photo shows perovskite films on glass substrates. Amount of applied anti-solvent (from left to right): 50 μl, 25 μl, 0 μl.

thickness and roughness R_q of the perovskite films with different amounts of anti-solvent applied. The roughness increases by a factor larger than 20 upon moving from 50 to 0 μl CB. Interestingly, there is only little difference between the surface morphologies of the film to which no anti-solvent was applied and the one where 25 μl CB was applied.

Table 3.4: Dependence of layer thickness and surface roughness of the perovskite on top of glass on the amount of anti-solvent applied during spin coating.

CB / μl	thickness / nm	R_q / nm
50	301 ± 8	7±3
25	316 ± 30	140 ± 35
0	348 ± 20	180±30

A comparison of the film's crystal structures via XRD (Fig. 3.5) reveals only slight differences. The typical perovskite peaks are present in all samples, though the peaks are less distinct for those with less to no anti-solvent applied. This could point to a reduced degree of crystallinity. Small amounts of lead iodide (PbI_2) can be found in all three films. However, the XRD pattern of the samples with 0 and 25 μl anti-solvent exhibit a small additional peak at 11.6°. Comparison with literature [132–134] suggests that the additional peak might belong to the hexagonal δ-phase of $FAPbI_3$. This could indicate that in the cases where less or no anti-solvent was applied FA-rich regions phase-separate and crystallise in the δ-phase that is stable at room temperature.

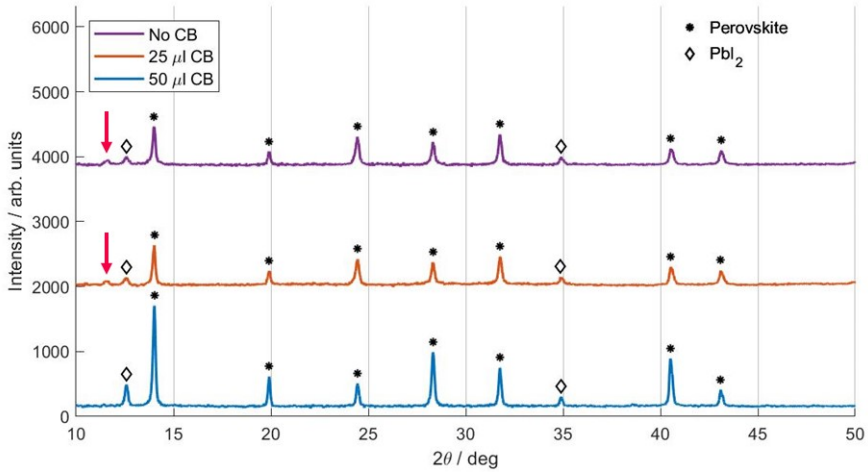

Figure 3.5: XRD pattern for perovskite films fabricated using different amounts of the anti-solvent CB. Instrument: Rigaku.

3.4.2 Effect of anti-solvent dripping on the device performance

Subsequent to the above described investigations of perovskite films on glass, 6 fully working solar cells were fabricated incorporating perovskite layers to which 0, 25 and 50 μl of anti-solvent were applied, 3 with PEDOT:PSS as HTL and 3 with NiO_x.

Figure 3.6 shows the achieved average solar cell parameters as a function of the amount of anti-solvent. Surprisingly, the average efficiency is not improved by the anti-solvent dripping. If anything, it seems to decrease with the amount of anti-solvent. In contrast, the standard

deviation increases with the amount of CB that was applied, indicating that solar cells whose perovskite layers were subjected to anti-solvent dripping are far less reproducible. This does not come as a surprise considering that the anti-solvent step can be poorly controlled and that the result sensitively depends on the exact dripping time, speed and force. Besides that, spin coating itself, though a very fast, low-cost method for thin film processing, can induce inhomogeneities in the film. The centrifugal forces, acting on the sample while it is spinning, introduce strain effects and depending on the roughness and uniformity of the underlying surface, the resulting thin film might not always be as uniform as desired.

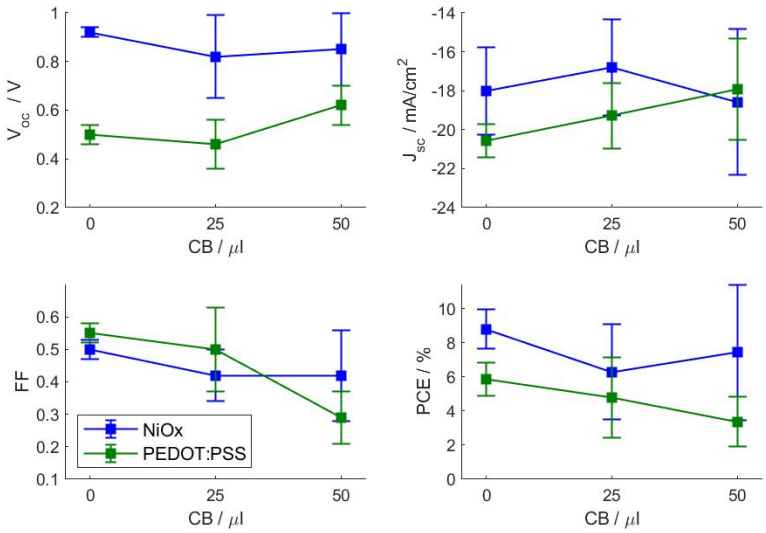

Figure 3.6: Effect of different amounts of anti-solvent (0, 25 and 50 μl) on achieved solar cell parameters. Values represent average taken over 6 cells (1 substrate each) with their standard deviation. Scan rate: 1000 mV/s. Scan direction: reverse. Light source: Dedolight.

Comparing the EBIC images of cells fabricated using different amounts of anti-solvent (Fig. 3.7 and 3.8) shows that none of the cells generate a homogeneous current signal but the scale and shape of the inhomogeneities differ. Analogous to the surface morphology of the perovskite films in Figure 3.4, the EBIC images appear rather smooth for 50 μl CB (Fig. 3.7) but grainy in the cases of 25 and 0 μl (Fig. 3.8). For the former, inhomogeneities seem to stem mainly from the impact of spin coating and anti-solvent dripping directly. The dropping anti-solvent might have washed away part of the perovskite film, e.g. resulting in the circular non-responsive region in the middle cell. For the latter, inhomogeneities seem to derive from the crystallisation behaviour of the perovskite film. Clusters and grains with a high EBIC signal are surrounded by areas that yield zero current. Combined with the observation of poor film coverage mentioned above, the non-responsive regions might correspond to regions where there is simply no (or only a very thin) perovskite layer present. Due to unfortunate circumstances, no SEM measurements could be performed on the perovskite layers to which less or no anti-solvent was applied. Taking SEM images of the film surfaces would have allowed a direct comparison of the film micro structures (also to Fig. 3.1),

possibly confirming the above mentioned hypotheses.

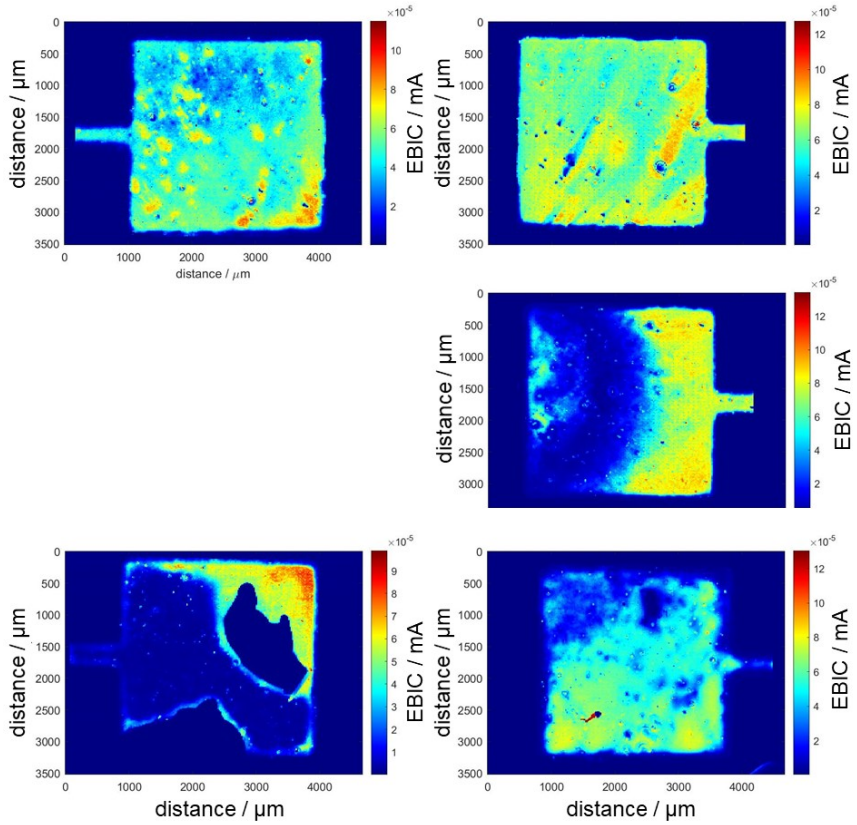

Figure 3.7: EBIC images of 5 cells on the same substrate. During spin coating of the perovskite, 50 μl CB were applied. HTL: NiO_x. Positioning corresponds roughly to actual position on the square substrate. For the cell in the lower left corner, part of the silver electrode was accidentally peeled off.

It would also be interesting to have EBIC images of cells that are close to the current record of 25.2 % in terms of efficiency to check whether their excellent performance is due to a more uniform power output over the entire cell area or whether the efficient regions are merely much more efficient compared to the cells fabricated in this thesis.

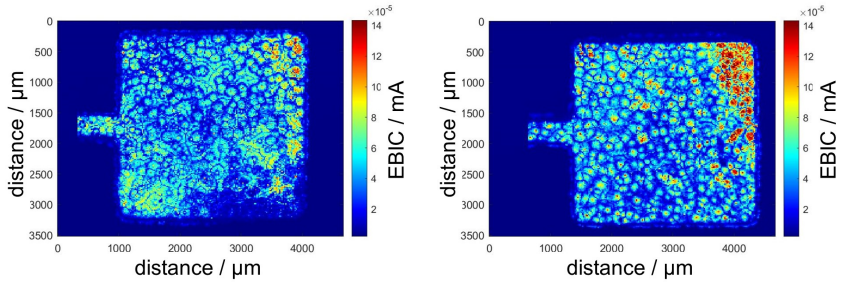

(a) 25 μl CB (b) 0 μl CB

Figure 3.8: EBIC images of cells with 0 or 25 μl CB applied during anti-solvent step.

3.5 Device encapsulation

To protect the perovskite solar cells from moisture and oxygen and to allow measurements in ambient air without rapid degradation, a simple encapsulation method was tested on several devices. The aim was not to achieve a perfect encapsulation that would prohibit oxygen and moisture ingress on a permanent basis, but rather to achieve decent protection for a limited period with minimal effort. For this reason, only the active area of the cells was covered by a glass sheet, leaving the contact pads exposed (see Fig. 3.9a). That way, the encapsulated cells could be electrically contacted in the same fashion as the unencapsulated devices. The glass sheet was attached to the device by a thin layer of an encapsulant (see Fig. 3.9b). A photo of an encapsulated device can be found in Figure 3.9c.

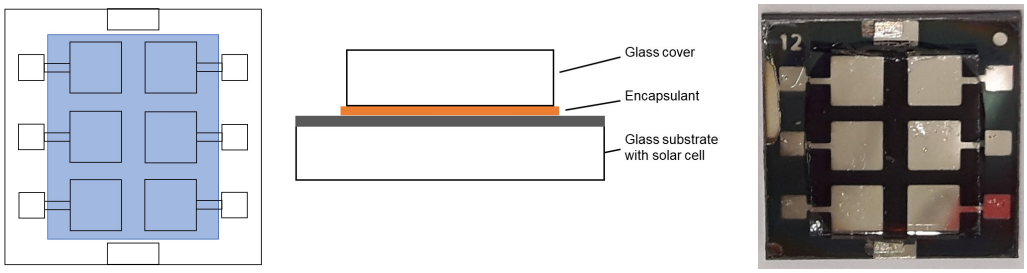

(a) (b) (c)

Figure 3.9: Encapsulation method. (a) Top view. Area covered with glass sheet in blue (1x1.2 mm). (b) Cross sectional view. (c) Photo of a substrate encapsulated with UHU epoxy glue.

To find a suitable encapsulant, two different products were tested and compared with each other. The first one was an encapsulation epoxy specifically designed for organic photovoltaics and LEDs by Ossila. The second one was an ordinary 2-component epoxy

adhesive by UHU (product no. 62981, see section 2.1.2). To test the effectiveness of the encapsulant, JV-scans of the cells were measured directly before and after the encapsulation, as well as after 1 and 4 days of storing the cells in ambient air. For an unencapsulated reference device, the PCE dropped to 30 % of its initial value within 1 day. After 4 days, the cell was almost completely degraded. Only 1 % of the initial efficiency was left.

Interestingly enough, the encapsulant by Ossila did not prove suitable for perovskite solar cells. Upon application of the epoxy onto the surface of the cell, an almost instant change of the perovskite to a more yellowish transparent colour was observable. The colour change was more distinct if ZnO was part of the cell's architecture. JV-scans revealed a drastic decrease in cell efficiency after encapsulation with Ossila epoxy (Fig. 3.10a). Apparently, the encapsulant chemically reacts with part of the solar cell. The change is most notable in the short-circuit current which drops almost to zero. In comparison, the UHU epoxy glue led to more promising results (Fig. 3.10b). The J_{sc} remained almost constant over the monitored period of time. Slight changes in FF and V_{oc} are noticeable, but they appear to stabilise 1 day after the encapsulation.

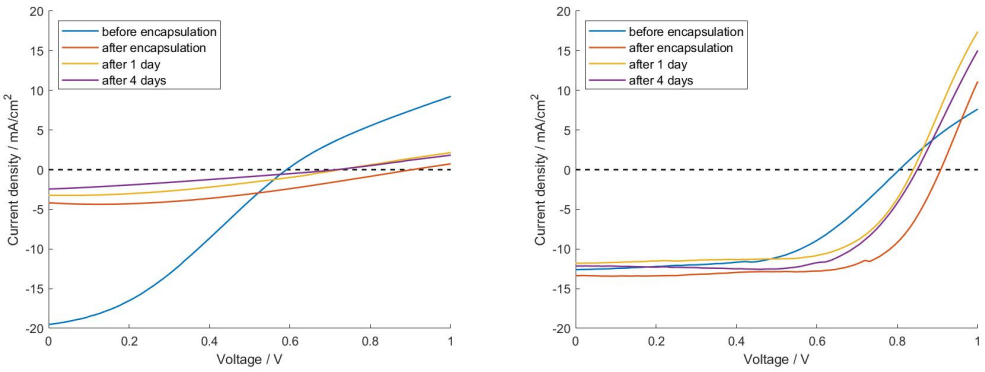

(a) Ossila encapsulation epoxy

(b) UHU 2-component epoxy glue

Figure 3.10: Change in JV-curves upon ageing in ambient air for two different encapsulants. HTL: PEDOT:PSS. Scan speed: 1000 mV/s. Scan direction: reverse. Light source: Dedolight.

Due to these promising results, several devices were encapsulated with UHU epoxy glue in the described fashion, packaged in nitrogen atmosphere and transported to Vienna for further measurements. However, re-measuring the cells in Vienna revealed distinct changes of the encapsulated cells when compared to the unencapsulated ones (Fig. 3.11). The PCE of all cells dropped upon transport, probably because the packaging was not completely impermeable, yet the loss in PCE was larger in the encapsulated cells. This is most likely due to the behaviour of the V_{oc}. While the open circuit voltage improved on average for unencapsulated cells, the UHU epoxy encapsulant appears to significantly reduce it. At the same time the fill factor (FF) improves. However, the drop in V_{oc} was not permanent. Upon light soaking for several hours, the V_{oc} went up to its original values of around 0.8 - 0.9 V (see Fig. 6.6 in section 6.3.2).

Nevertheless, the encapsulant appears to react with and change the device, an effect that is, in general, undesirable. The photo in Figure 3.12 provides another indication for a

reaction of the encapsulant with the solar cell. Some days after the encapsulation, smears in the perovskite layer appeared in some of the devices.

Another problem that was encountered with the above described encapsulation methods was the degradation of the exposed contact pads. After a certain ageing time, electrical contact to the cells was lost, and it was therefore impossible to check whether the encapsulated, active cell area was still intact.

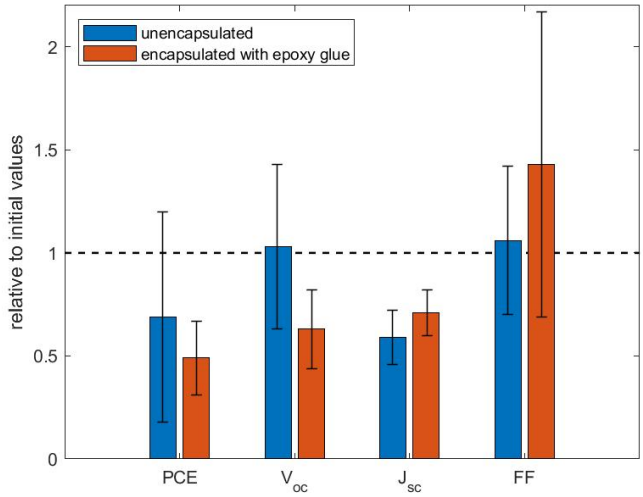

Figure 3.11: Average change in solar cell parameters for encapsulated and unencapsulated devices relative to their initial values measured directly after fabrication. Measurements were taken after sealed transport to Vienna and 5-13 days of storage in N_2-atmosphere for 21 unencapsulated and 18 encapsulated cells.

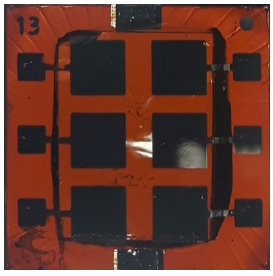

Figure 3.12: Photo of an encapsulated device. Smears, making the device transparent, are visible in the centre of the substrate.

3.6 Device characterisation

3.6.1 Device efficiencies and reproducibility

This section provides an overview of device efficiencies achieved by using the optimised synthesis routes described in section 2.1.4 (and discussed above), and evaluates their reproducibility.

Figure 3.13 shows a statistical analysis of all fabricated cells that achieved a PCE greater than 1 %. In terms of device efficiency, NiO_x as HTL clearly gives the best results, followed by PEDOT:PSS with DMSO, and pure PEDOT:PSS. The distributions roughly have Gaussian shape, but with a large variance. Table 3.5 lists the percentage of cells that only achieved a PCE below 1 % and were thus classified as failures. The failure rate was especially high for cells with PEDOT:PSS + DMSO for reasons discussed above (sec. 3.2.1). All this shows that reproducibility is not very good, even though great care was taken during synthesis to process all cells in the same manner. This might be due to the fact that many

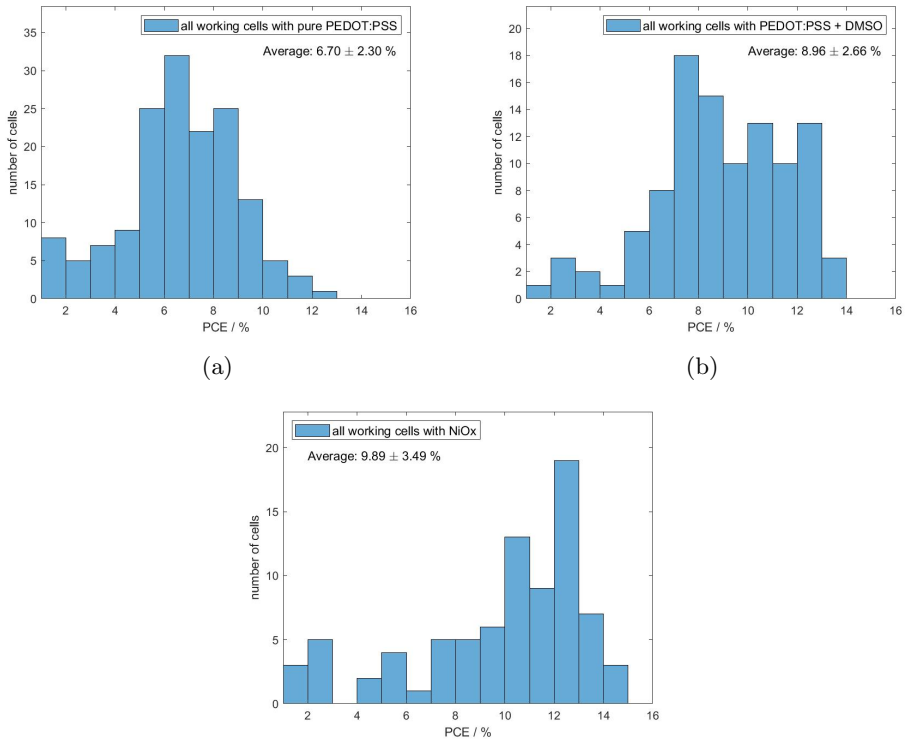

Figure 3.13: Distribution of efficiencies achieved with different cells architectures. (a) all working cells with pure PEDOT:PSS as HTL. (b) all working cells with DMSO (5 % or 10 %) added to PEDOT:PSS as HTL. (c) all working cells with NiO_x as HTL. Efficiency was extracted from fast reverse JV-scans with a scan rate of 1000 mV/s.

process parameters could not be properly controlled, the most crucial of them probably the

Table 3.5: Percentage of fabricated cells whose PCE was below 1 %. Those cells were considered as failures.

HTL	failure / %
PEDOT:PSS	15.9
PEDOT:PSS (5 % or 10 % DMSO)	24.1
NiO_x	9.4

weighing in of the perovskite precursor and the anti-solvent dripping (see section 2.1.3). The actual molar ratios of the components in the precursor usually deviated slightly from the calculated values. Such a variation in the composition might influence the crystallisation of the perovskite. However, careful analysis of the data did not reveal a distinct correlation between precursor composition and achieved device parameters. Regarding the anti-solvent step, the homogeneity of the resulting film heavily depends on the exact time of dripping, the distance between the pipette tip and the substrate, and the force and speed with which the anti-solvent is applied. Sufficiently reproducible results can probably only be achieved by an automation of this process. Other factors that might influence the achieved device efficiency are fluctuations in room temperature and relative humidity, as well as different amounts of solvent vapour present inside the glovebox.

3.6.2 Layer thicknesses

Thicknesses of the individual layers in the solar cell setup were measured by profilometry and evaluation of SEM cross sectional images. For each layer, SEM images of several different samples were taken. From the extracted thickness values an average was calculated. In order to determine the thickness of the NiO_x films, x-ray reflectivity (XRR) measurements were taken because profilometry did not work in this case. Probably, NiO_x is too hard to scratch with a common blade. The measurement results obtained by the different methods are listed in Table 3.6. The agreement is quite good for most of the layers. In comparing them, one has to take into account that measurements were performed on different samples, although all were fabricated using the same process parameters. In addition to measuring inaccuracy, a certain degree of thickness variation occurring over the different samples can be expected.

In contrast, the thickness values obtained for $PC_{60}BM$ differ by more than 100 %. This could have several reasons. As noticeable in Figure 3.14b, the thickness of the $PC_{60}BM$ layer varies quite a lot, filling the valleys within the perovskite film and reducing its surface roughness. In extracting the thickness from the SEM images, places where the layer was clearly discernible, and thus of notable thickness, were chosen. Most likely, this led to an overestimation of the average thickness.

The perovskite layers reveal thicknesses below 300 nm while values reported in literature are generally higher (310-350 nm) [37, 114, 118]. Increasing the perovskite thickness, e.g. by reducing the spin coating speed or raising the concentration of the precursor, could lead to higher absorption, and thus higher efficiencies. Regarding the Ag electrode, measured film thicknesses are lower than the desired 120 nm (see section 2.1.4). This could be improved by adjusting the tooling factor of the quartz crystal thickness monitor.

Figure 3.14 shows cross sectional images of two solar cells, one with PEDOT:PSS as HTL, the other with NiO_x.

Table 3.6: Average thicknesses for the different layers in the solar cell architecture, measured by different methods.

	Profilometer	SEM	XRR
Layer	thickness / nm		
ITO	121 ± 5	130 ± 6	-
NiO_x	-	20 ± 2	21 ± 2
PEDOT:PSS	49 ± 5	40 ± 10	-
Perovskite	285 ± 15	285 ± 20	-
PC(60)BM	30 ± 15	68 ± 15	-
ZnO	34 ± 15	47 ± 10	-
Ag	108 ± 2	94 ± 20	-

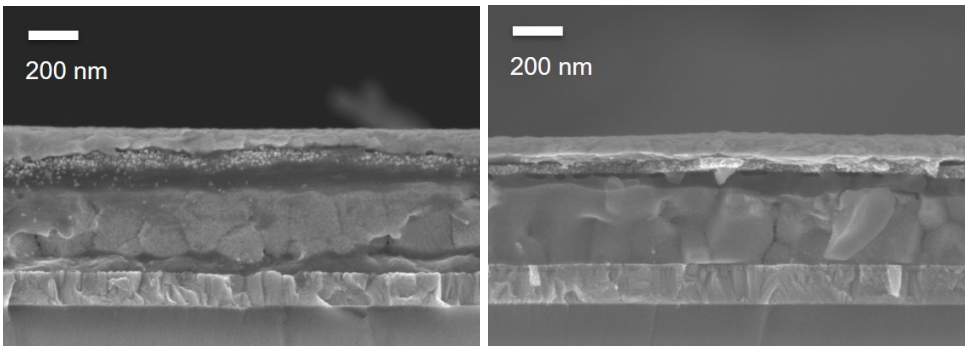

(a) PEDOT:PSS as HTL (b) NiO_x as HTL

Figure 3.14: SEM cross sections of completed solar cells. Sequence of layers from bottom to top: glass/ITO/HTL/perovskite/PC(60)BM/ZnO/Ag.

3.6.3 XRD characterisation

To facilitate the peak identification in XRD pattern of completed solar cell devices, XRD measurements of the separate materials were performed (see Fig. 3.15). A list of the peak positions can be found in Table 3.7. The values are in good agreement with literature [37, 135–138]. For PbI_2, not all peaks that were reported in literature [136] appear in the measurement in Figure 3.15. Nonetheless, they are listed in Table 3.7 for the sake of completeness.

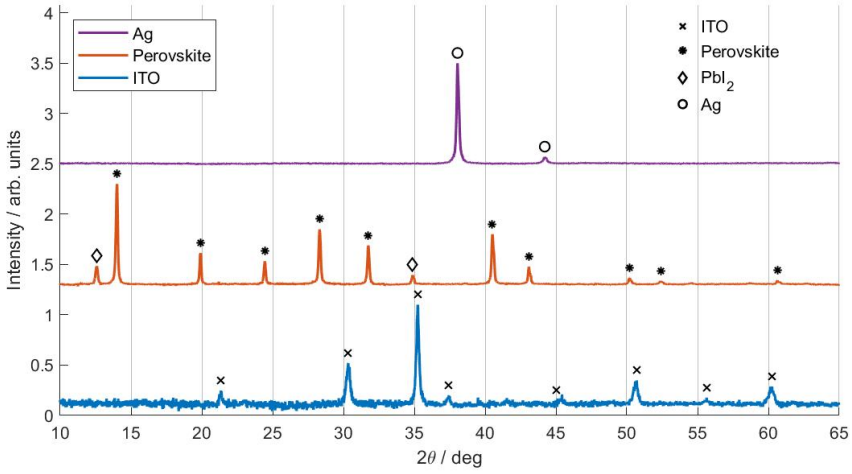

Figure 3.15: XRD pattern of single layers on glass substrates. Instrument: Rigaku.

Table 3.7: XRD peak positions (2θ) of the materials used in the solar cell setup. Unless indicated otherwise, peak positions were derived from the measurements in Figure 3.15 by Split Pseudo-Voigt peak fitting.

triple-cation perovskite / °	ITO / °	Ag / °	PbI_2 / °
14.0	21.4	38.1	12.6
19.9	30.3	44.2	26.0 *
24.5	35.2		34.9
28.3	37.4		39.0 *
31.8	45.4		45.5 *
40.5	50.7		53.0 *
43.1	55.6		
50.2	60.3		
52.4			
60.7			

* taken from [136]

3.6.4 Hysteresis

Hysteresis was present to some degree in all cells that were fabricated for this thesis. The magnitude and shape of hysteresis varied but no distinct tendency or correlation with other parameters could be identified which is why hysteresis effects often have been disregarded in the discussion of the results. Figure 3.16 shows some examples of hysteresis in both cells with PEDOT:PSS as HTL and cells with NiO_x.

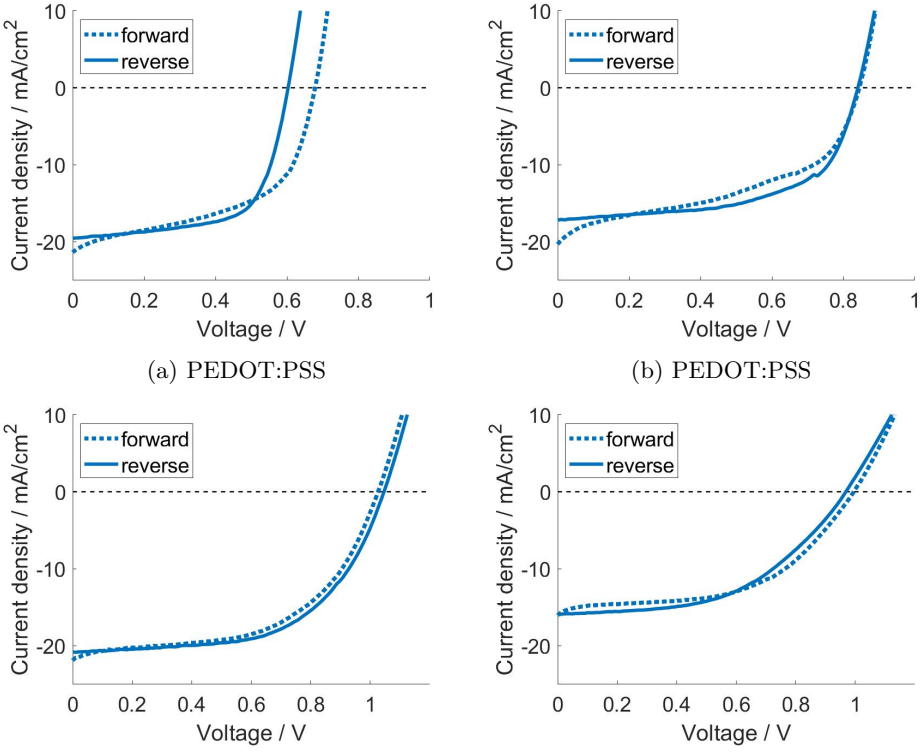

(a) PEDOT:PSS (b) PEDOT:PSS

(c) NiO_x (d) NiO_x

Figure 3.16: Hysteresis of exemplary JV-curves for cells with different hole transport layers. Scan speed: 100 mV/s. Delay time: 100 ms. Light source: Dedolight.

3.6.5 Effect of different scan speeds

In order to estimate the effect of different scan speeds on the JV-characteristics, a cell with NiO_x as HTL was repeatedly measured using different delay times (see Fig. 3.17). However, the change in JV-curves seems to be dominated by the effect of illumination. The J_{sc} increases continuously with the succeeding scans, independent of the scan speed that starts at high values, goes down to lower values and back to high ones again. Only the FF is consistently higher for slower scan rates. One therefore needs to take great care when performing JV-characterisation. It is not only the choice of measurement parameters that influences the result but even more importantly the history of the sample, especially its exposure to light. This has already been demonstrated by Unger et al. [59]. They

showed that subjecting a device to illumination at positive bias, or while performing several cycles between 0 V and V_{oc}, significantly improves the PCE. Comparing the two scans in Figure 3.17 with 50 ms delay time shows that the first scan (1) yields a PCE of 3.34 % while the second (4) has improved to 4.76 %.

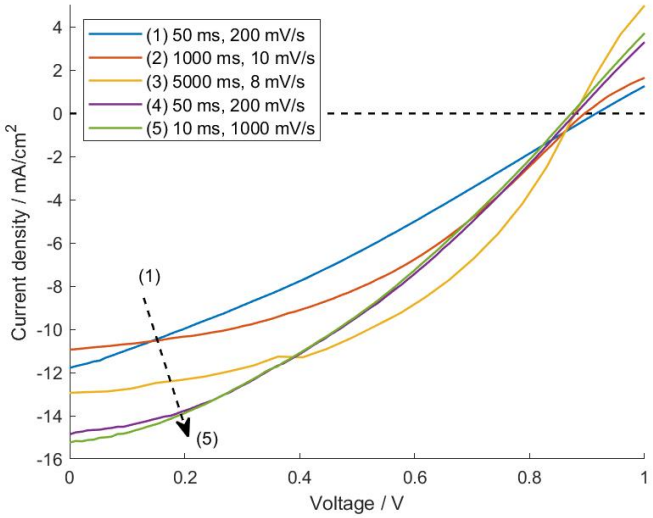

Figure 3.17: Effect of different scan speeds on JV-curve. Measurements were performed in the chronological order (1) to (5). Delay time at each voltage step is given in ms, scan speed in mV/s. Scan direction: reverse. Dashed arrow indicates the tendency of J_{sc} to increase upon prolonged illumination, independent of scan speed. HTL: NiO_x. Light source: Dedolight.

3.7 Conclusion

To sum up, for this thesis, inverted p-i-n perovskite solar cells could be successfully synthesised with two different hole transport layers: organic PEDOT:PSS and inorganic NiO_x. In terms of optimisation of PEDOT:PSS, it could be shown that DMSO as an additive significantly improves the short-circuit current density J_{sc}, and thus the power conversion efficiency PCE, of the resulting solar cells. This is in agreement with previously reported results [111, 112]. However, issues with film uniformity were encountered that could not be resolved satisfactorily within this thesis' work. Using the inorganic NiO_x as a hole transport layer resulted in very promising device efficiencies when the annealing of the NiO_x films was performed inside a furnace. Regarding the electron transport layer, the introduction of a ZnO nanoparticle layer on top of PCBM lead to much higher efficiencies, most likely due to an improvement of the charge extraction and blocking properties. However no optimisation in terms of layer thickness was performed. Optimising the deposition parameters, such as spin-coating speed, duration and annealing procedures, for each layer individually, would probably lead to still more improvements in the solar cell performance.

Regarding the perovskite film formation, SEM images showed a very regular polycrystalline micro structure with grain sizes ranging from 130-300 nm. Pin holes are rare for perovskite films grown on top of hole transport layers that were deposited by the optimised routes discussed in sections 3.2.1-3.2.2. The XRD measurements in section 3.6.3 show a high degree of crystallinity of the deposited perovskite layers, sometimes with a small amount of PbI_2 present. EBIC images taken of completed solar cells revealed that the spatial uniformity of solar cell performance was bad. This might be due to the 1-step deposition method (see section 2.1.3) that was used for the perovskite layers because the appertaining anti-solvent dripping step is poorly controllable. Nevertheless, it has a large influence on the crystallisation process of the perovskite, as was demonstrated in section 3.4.1. However, even though the surface morphology is drastically altered by applying an anti-solvent, no significant improvement of the total device performance could be observed. It seems that the negative impacts of anti-solvent dripping (i.e. bad film uniformity) counteract the positive aspects. Despite the easy, fast processing of the 1-step method, other deposition techniques, such as the 2-step method or vapour deposition, might be better suited to achieve higher film uniformity, and hence a spatially more homogeneous device performance.

In terms of device encapsulation, no well-suited encapsulant could be found, although decent results were achieved with UHU epoxy glue.

Average device efficiencies that could be achieved amounted to 6.7 $\pm$ 2.3 % for cells with pure PEDOT:PSS as HTL, 9.0 $\pm$ 2.7 % for PEDOT:PSS+DMSO and 9.9 $\pm$ 3.5 % for Cs-doped NiO_x.

Chapter 4

Stability towards moisture

4.1 Introduction

This section focusses on the stability of perovskite solar cells towards moisture. As described in section 1.3.3, the perovskite structure takes on water easily which results in the formation of hydrates, or in the worst case, the complete decomposition of the crystal. It has already been demonstrated [105] that, for an optimised encapsulation and device architecture, perovskite solar cells can withstand high levels of humidity and temperature, as are present during the damp heat test, for 100 hours. However, without a proper encapsulation perovskite solar cells can be expected to degrade within a very short time period. It was the aim of the damp heat tests performed in this section to investigate exactly how short this time period was and examine the structural changes that occur upon exposure to moisture. Furthermore, the effectiveness of the encapsulation method developed in the previous section 3.5 was tested with respect to its protection against moisture ingress.

4.2 Damp heat testing

As briefly described in section 1.4.2, damp heat testing is a standard stability testing routine during which the cells are exposed to 85 °C and 85 % relative humidity.

4.2.1 Measurement routine

For this thesis, damp heat tests were performed on two cells with PEDOT:PSS as hole transport layer, one unencapsulated and one encapsulated with UHU epoxy glue (see 3.5 for details on the encapsulation method).

The tests were performed inside a climate chamber that was pre-heated to 85 °C and 85 % relative humidity. However, damp heat conditions were not perfectly fulfilled during the experiment. For the loading and unloading of the chamber, the door had to be opened for a few seconds, causing part of the humidity to escape. Since most cells were kept inside the chamber for a couple of minutes only, the humidity level did not reach the desired value of 85 % again within this period but was around 60 %. In addition to that, the devices were at room temperature when put into the climate chamber which resulted in water vapour

condensing on the surfaces, forming large droplets. It can be expected that liquid water is much more efficient in penetrating the solar cell and dissolving the perovskite. To avoid such condensation in future experiments, samples should be preheated to 85 °C before entering the climate chamber.

To track the stability of the devices, the samples were removed from the chamber at regular intervals, subjected to JV- and XRD characterisation and returned to the chamber. In the discussion of the results, stated time intervals always refer to the total time that the sample has spent inside the damp heat chamber. For the encapsulated device, no XRD characterisation was possible.

4.3 Damp heat for an unencapsulated device

Visual degradation of the unencapsulated device is already visible after 1 min in damp heat (see Fig. 4.1). The sample has become partly translucent and blotchy. After 5 min, the silver electrodes show distinct signs of degradation and the subjacent layers look very inhomogeneous. Figure 4.2 displays JV-curves of one of the cells on the sample that were measured after different time intervals inside the climate chamber. Already after 1 min inside the damp heat chamber, the cell has lost almost all its photovoltaic efficiency. The JV-curve still resembles that of a solar cell but both J_{sc} and V_{oc} are negligibly low. After 3 min, the cell does not exhibit any photovoltaic response anymore. Dark and light JV-curves are almost identical in shape.

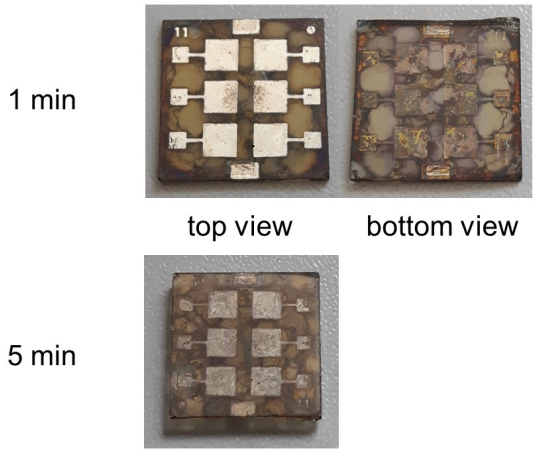

Figure 4.1: Photos of an unencapsulated device after being subjected to damp heat conditions for different time intervals.

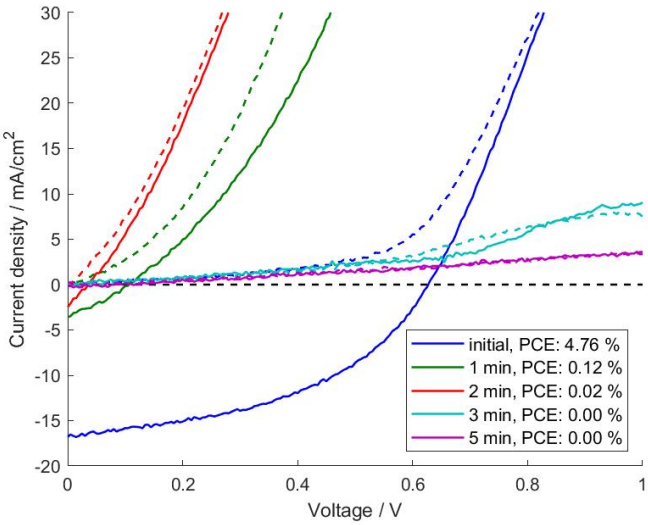

Figure 4.2: Change in JV-scans of a device subjected to damp heat conditions. Solid (dashed) line corresponds to illuminated (dark) scan. Scan direction: reverse. Scan speed: 250 mV/s. Light Source: solar simulator.

4.3.1 Structural changes (XRD)

The change in crystal structure upon damp heat testing is shown in Figure 4.3. After 1 min, a small amount of PbI_2 is visible that disappears in due course. Instead, several other peaks emerge, the most distinct at around 11.9 °C, while the peaks associated with the perovskite crystal structure are greatly reduced in intensity. Comparing the emerging peaks with literature suggests that the new structure that forms might be some kind of hydrate. The fact that no evidence of large amounts of PbI_2 forming upon damp heat testing might either indicate that the perovskite does not fully and irreversibly decompose or that some components, such as iodine, are dissolved by water and removed from the structure, thus preventing PbI_2-formation. The former could be verified by drying the sample for several hours subsequent to the damp heat exposure and remeasure its XRD. However, considering the state of the device after 5 min of damp heat testing (see Fig. 4.1), it is very unlikely that drying would be able to revert it to its original state. Table 4.1 lists the positions of the peaks that emerged upon damp heat exposure.

As a final remark, it should be mentioned that the area illuminated by the x-ray beam was only 2.3x1 mm, and therefore smaller than the active cell area. It was attempted to measure the same part of the sample at each characterisation step. Positioning might not have been exact, though, and it is therefore possible that changes in the XRD pattern measured after 1 to 5 min were due to a shift in the illuminated area rather than due to an actual structural change. Nonetheless, the failure of the perovskite solar cell within minutes when subjected to damp heat without any protective encapsulation could be successfully shown and the development of a hydrate-like structure verified by XRD characterisation.

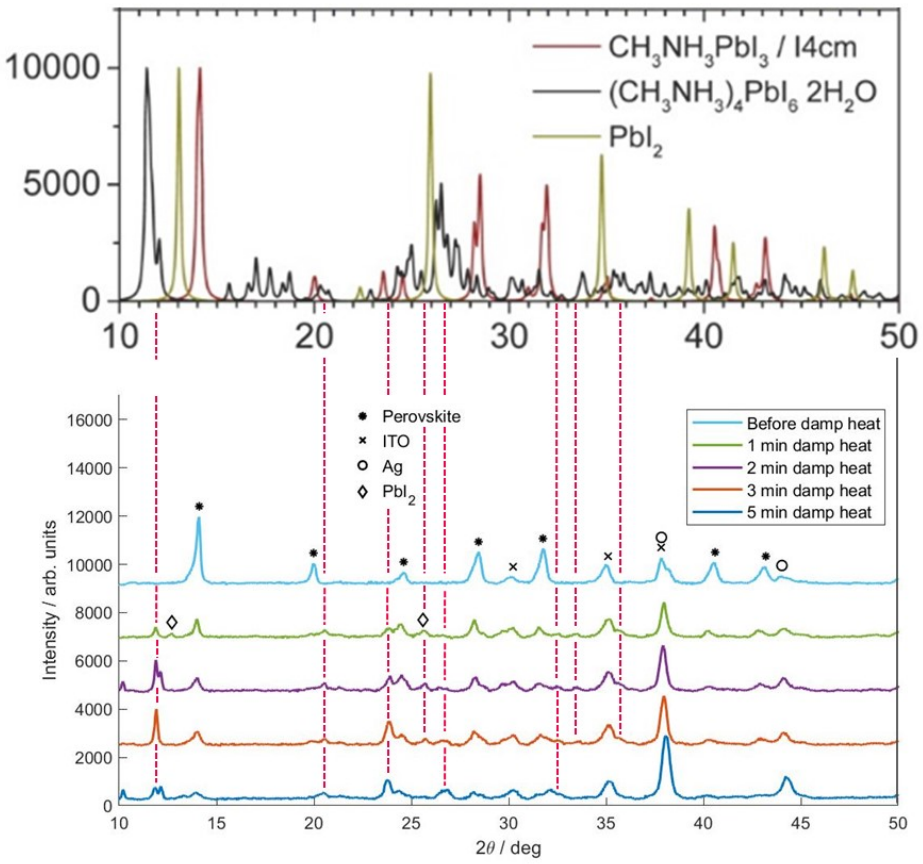

Figure 4.3: Change in XRD pattern for a device subjected to damp heat conditions (lower graph) after different exposure times in comparison with an XRD pattern calculated for a copper x-ray source (upper graph, reprinted from [82]. Copyright © 2015, American Chemical Society). The positions of the peaks appearing upon damp heat testing roughly correspond to those of the dihydrate (black line in the upper graph). Instrument: ThermoScientific.

4.4 Encapsulated device

The results of damp heat testing for the encapsulated device are presented in the following. After 1 min in the damp heat chamber, the encapsulated area still looked fully intact (see photo in Fig. 4.4) while the unprotected device area showed signs of severe degradation. Unfortunately, due to the degradation of the outer contact pads, no electrical contact to the encapsulated solar cells could be achieved. Thus, it could not be tested whether the cells that looked intact were indeed still functioning. Because of this, testing of the effectiveness of the encapsulation could be performed by visual inspection only. The device was kept in

Table 4.1: XRD peaks appearing in unencapsulated devices after damp heat testing. Peak position was averaged over all measurements (exposure times: 1 min, 2 min, 3 min, 5 min).

$2\,\theta$ / °	$\Delta 2\theta$ / °
11.9	0.1
20.5	0.1
23.8	0.1
25.7	0.1
26.6	0.2
32.6	0.2
33.5	0.1
35.8	0.2

the damp heat chamber until signs of failure could be observed for the encapsulation. This was the case after over an hour in the damp heat chamber at which point the encapsulation began to fail at the edges. To put this result in context, the IEC standard test requires the devices to withstand 1000 hours in the damp heat (see section 1.4.2). However, since the aim of the encapsulation developed for this thesis was only to provide crude, short-term protection, the result is quite satisfying.

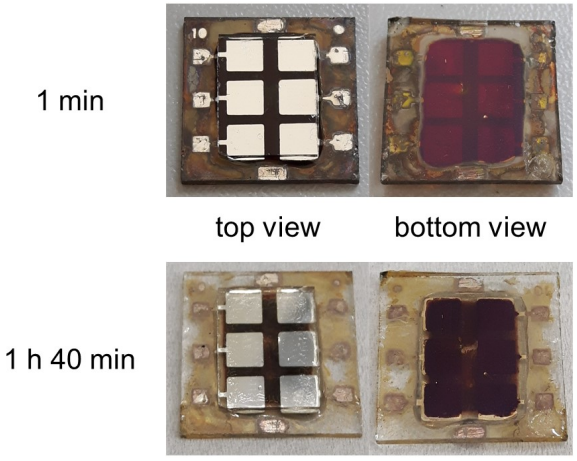

Figure 4.4: Photos of an encapsulated device after being subjected to damp heat conditions for different time intervals. After 1 hour and 40 min, the encapsulation begins to fail at the edges.

4.5 Conclusion

To sum up, the damp heat tests above could successfully demonstrate that unencapsulated perovskite solar cells of the device architecture used for this thesis rapidly degrade in damp

heat conditions. 1 min in the damp heat chamber sufficed to cause a loss in device efficiency of over 95 %. XRD analysis revealed a strong decrease in the height of the peaks that correspond to the perovskite structure while new peaks, possibly belonging to a hydrate compound, appeared (Fig. 4.3).

By encapsulating the cells with UHU epoxy glue, major moisture ingress could be successfully prevented for more than 1 hour. After 1 hour 40 minutes, the encapsulation began to fail at the edges. Unfortunately, electric contact to the encapsulated cells was lost after the first minute in damp heat. For this reason, no information on the electrical state of the cells could be gained.

Chapter 5

Influence of storage conditions

5.1 Introduction

As described in section 1.3, perovskite solar cells are sensitive to almost all possible external stressors: oxygen, moisture, light, temperature and electrical fields. This results in a multitude of different degradation pathways that most likely interact, forming a complex system. To gain a better understanding of how a device reacts to a specific external stressor and how these degradation mechanisms are influenced by the presence of other stressors, it is crucial to separate out the individual effects and perform stability tests on devices exposed to one stressor at a time.

A standard stability testing routine, as discussed in section 1.4.2, is shelf life testing. During shelf life testing, the stability of solar cells under different storage conditions is investigated, the most basic one being dark storage at room temperature.

Because the previous section 4 confirmed the high sensitivity of perovskite solar cells to the presence of humidity, for this thesis shelf life testing was performed only in dry, low-humidity environments. Two different storage conditions were chosen: dark storage in an inert nitrogen atmosphere and dark storage in dry air. Measurement routines and results for both variants are described in the following sections.

5.2 Dark storage in inert atmosphere

Dark storage in inert atmosphere eliminates all possible external influences that might induce degradation of the solar cells. As long as no internal mechanisms occur, such as chemical reactions or ion diffusion, the cell should remain perfectly stable. However, in order to monitor the stability of the cells, regular measurements are necessary that require short-term exposure of the cell to light and electrical bias.

5.2.1 Measurement routine

Dark storage testing was carried out for 6 perovskite solar cells located on 6 different substrates (3 with pure PEDOT:PSS as HTL, 3 with 5 % DMSO added). The cells were

wrapped in aluminium foil to achieve dark conditions and kept inside the glovebox (nitrogen atmosphere) for 350 hours. At regular intervals, JV-scans were performed to track their performance. The cells were unwrapped and placed into the light just before measuring them. That way exposure to light was minimized and the cells could be measured as close as possible to their dark state. JV-scans were performed first in forward direction, immediately followed by the reverse scan. A rather low scan speed (26 mV/s, 500 ms per voltage step) was chosen to reduce hysteretic effects, as suggested by Unger et al. [59].

After the 350 hours, the cells were removed from the glovebox to perform XRD characterisation.

5.2.2 Initial characterisation

Table 5.1 lists the solar cell parameters of the devices that were subjected to dark storage in inert atmosphere. It should be noted here that the batch that was used for testing storage conditions was not a very good one. J_{sc} values were only around 10 mA/cm^2, which was probably because there were issues with the evaporation of the silver electrode. Only a 82 nm-thick electrode could be deposited instead of the usual 120 nm. However, this should not have had any influence on the storage stability of the cells.

Table 5.1: Initial solar cell parameters of devices (3 with pure PEDOT:PSS as HTL, 3 with 5 % DMSO added) subjected to dark storage inside the glovebox (inert atmosphere). Scan parameters: 1000 ms per step, scan speed 13 mV/s. Light source: Dedolight.

Cell type	Scan direction	V_{oc} / V	J_{sc} / mA/cm^2	FF	PCE / %
PEDOT:PSS	forward	0.96	6.70	0.69	4.62
	reverse	0.88	8.02	0.41	2.99
	forward	0.94	5.46	0.71	3.77
	reverse	0.90	6.98	0.41	2.66
	forward	0.91	6.98	0.63	4.22
	reverse	0.86	7.76	0.42	2.87
PEDOT:PSS (5 % DMSO)	forward	0.85	8.96	0.60	4.73
	reverse	0.86	10.09	0.53	4.71
	forward	0.86	10.46	0.49	4.54
	reverse	0.87	11.34	0.51	5.17
	forward	0.77	11.71	0.64	5.89
	reverse	0.81	13.84	0.57	6.42

5.2.3 Results

The results of dark storage in inert atmosphere can be found in Figure 5.1-5.2 for the JV-scans measured in forward an reverse direction respectively. A fact that immediately catches the eye is that the curves resulting from the JV-scans in forward and reverse direction look quite differently. This might to some extent be caused by hysteretic effects. However,

repeating the JV-scans while keeping the cells illuminated, revealed a drift of the JV-curves, suggesting that metastable effects induced by the illumination might play a role. A strong response to light was already discussed in section 3.6.5 where it was demonstrated that the effect of illumination dominates the effect of different scan speeds. It can therefore be assumed that the discrepancy between the forward and reverse scans observed here is also to a large extent caused by the effect of light. The results derived from the reverse scans (Fig. 5.2) show a much narrower spread than that from the forward scans, suggesting that, upon illumination, the devices move towards a stabilised state and that this stabilised state does not significantly change over time when the devices are stored in the dark in nitrogen atmosphere. The effect of metastabilities and the cell's response to illumination will be discussed in more detail in due course (see section 5.6 and 6).

To eliminate the effect of illumination, one could monitor the JV-curves only in the dark and check whether their shape changes over time. However, dark JV-curves provide information only on the diode behaviour of the solar cell, determination of the power conversion efficiency and other characteristic solar cell parameters requires (short-time) illumination.

On the whole, neglecting the instability of the cells towards illumination, it can be concluded that the majority of the cells are stable when stored in the dark in an inert atmosphere. For both cells with pure PEDOT:PSS and cells with 5 % DMSO 2 out of 3 cells maintained more than 98 % of their initial PCE, when looking at the reverse scans, and can thus be considered stable. However, 1 out of 3 cells exhibited a significant loss in PCE that might have been induced by the presence of electric fields and/or illumination.

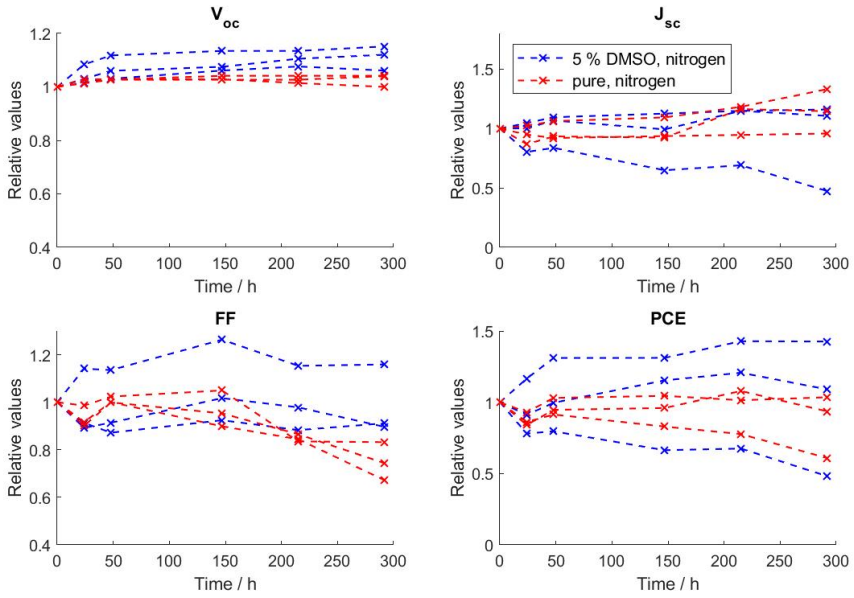

Figure 5.1: Change in solar cell parameters upon dark storage in nitrogen atmosphere. Scan direction: **forward**. 500 ms per step, scan speed 26 mV/s. Light source: Dedolight.

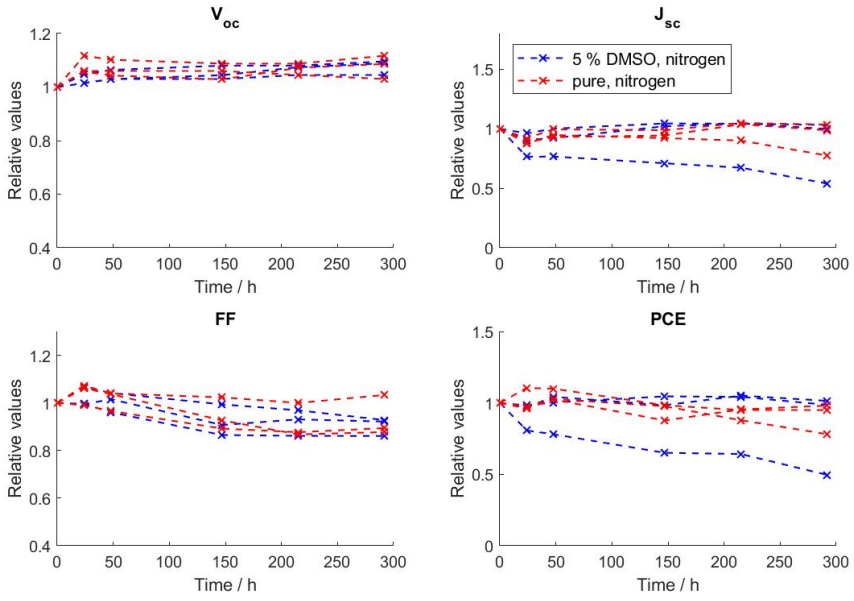

Figure 5.2: Change in solar cell parameters upon dark storage in nitrogen atmosphere. Scan direction: **reverse**. 500 ms per step, scan speed 26 mV/s. Light source: Dedolight.

5.3 Dark storage in dry air

Compared to dark storage in inert atmosphere, dark storage in dry air introduces the external factor oxygen. As discussed in section 1.3.2, perovskite solar cells are only expected to degrade due to oxygen if light is present at the same time. Therefore, cells stored in the dark in dry air should be stable. However, in order to monitor the stability of the cells, regular measurements are necessary that require short-term exposure of the cell to light and electrical bias.

5.3.1 Measurement routine

Analogous to the dark storage measurements in inert atmosphere, 6 cells located on 6 different substrates (3 with PEDOT:PSS as HTL, 3 with PEDOT:PSS (5 % DMSO)) were monitored. Again, the samples were wrapped in aluminium foil to keep them in the dark. Dry air conditions were achieved by placing the cells in a desiccator filled with calcium chloride.

However, the desiccator was not properly closed at all times during the storage period. Because it was not evacuated, it tended to slide open on its own accord after several hours. This issue was only discovered and eliminated after 140 hours. From that time on, a slight vacuum was generated inside the desiccator to keep the lid closed while at the same time retaining a large enough amount of oxygen inside it. Thus, when looking at the results of the dark storage testing, one has to keep in mind, though, that the dry air conditions probably have not been perfectly fulfilled for the first 140 hours.

5.3.2 Initial characterisation

Table 5.2 shows the initial solar cell parameters of the cells stored in the desiccator. They came from the same batch as the cells used for dark storage testing in inert atmosphere, and therefore exhibit the same low J_{sc}-values.

Table 5.2: Solar cell parameters of devices (3 with pure PEDOT:PSS as HTL, 3 with 5 % DMSO added) used for dry air ageing. Scan parameters: 1000 ms per step, scan speed 13 mV/s. Light source: Dedolight.

Cell type	Scan direction	V_{oc} / V	J_{sc} / mA/cm^2	FF	PCE / %
PEDOT:PSS	forward	0.83	4.48	0.66	2.52
	reverse	0.82	5.83	0.47	2.30
	forward	0.91	5.83	0.61	3.33
	reverse	0.87	6.54	0.45	2.59
	forward	0.95	6.46	0.69	4.32
	reverse	0.91	7.96	0.40	3.03
PEDOT:PSS (5 % DMSO)	forward	0.86	8.96	0.56	4.58
	reverse	0.87	9.99	0.53	4.86
	forward	0.92	10.57	0.58	5.89
	reverse	0.90	11.77	0.50	5.51
	forward	0.88	10.66	0.60	5.81
	reverse	0.88	12.22	0.52	5.96

5.3.3 Results

The results of dark storage in dry air are depicted in Figure 5.3-5.4 for scan direction in forward and reverse direction respectively. Again, the curves resulting from the JV-scans in forward and reverse direction differ significantly. As stated above, possible reasons could be hysteretic effects as well as a metastable response of the cells to illumination.

Comparing the behaviour of the devices with pure PEDOT:PSS and those with 5 % DMSO added for both scan directions (Fig. 5.3 and 5.4), shows that the latter degrade slightly faster and also end up at lower final efficiency values. Degradation takes place primarily in the current. This can be deduced from the fact that the degradation curves of J_{sc} and PCE are of similar shape. While the V_{oc} of devices with pure PEDOT:PSS remains fairly constant throughout the course of the measurements, the cells with DMSO exhibit a significant drop in voltage when measured in reverse direction (Fig. 5.4).

To conclude, rapid degradation (i.e. an efficiency loss by over 50 % within roughly 2 days) could be observed for both cells with PEDOT:PSS and cells with PEDOT:PSS (5 % DMSO). This does not agree with the assumption (see above, section 5.3) that oxygen is only detrimental in the combined presence of light. It is, however, unclear to what extent the cells were involuntarily exposed to humidity during the experiment due to the imperfect closing of the desiccator mentioned above (section 5.3.1). And even without the leakiness of the desiccator, cells were exposed to (humid) ambient air for several minutes during transfer

from the desiccator to the glovebox. Thus, the observed degradation could also have been caused partly by exposure to humidity.

To investigate whether the presence of humidity played a role in the observed degradation, it is necessary to repeat the stability test using an improved measurement setup and routine that completely eliminates any exposure to humidity.

But regardless of whether degradation was induced by oxygen, humidity or some other unknown factor, the present experiment clearly demonstrated the importance of protecting perovskite solar cells from any external influences in order to keep them from degrading.

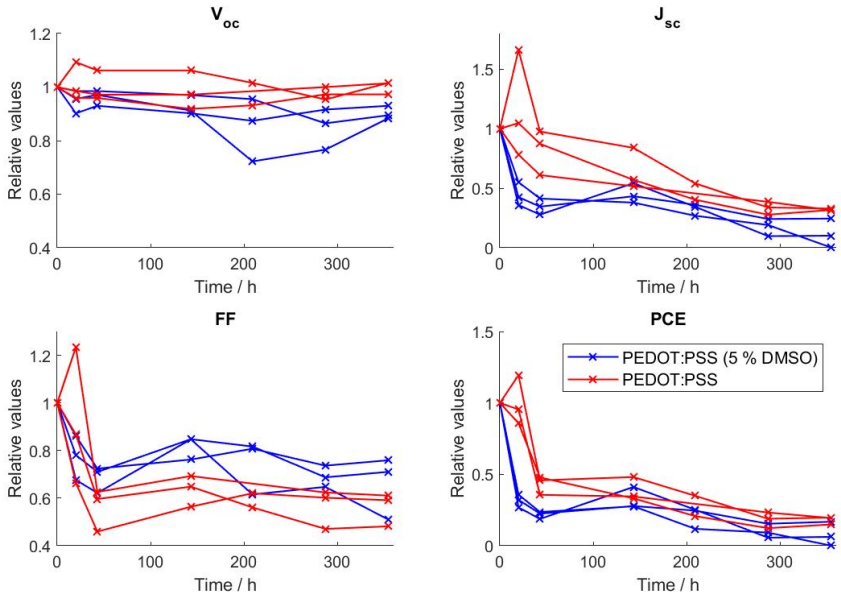

Figure 5.3: Change in solar cell parameters upon dark storage in dry air. Scan direction: forward. 500 ms per step, scan speed 26 mV/s. Light source: Dedolight.

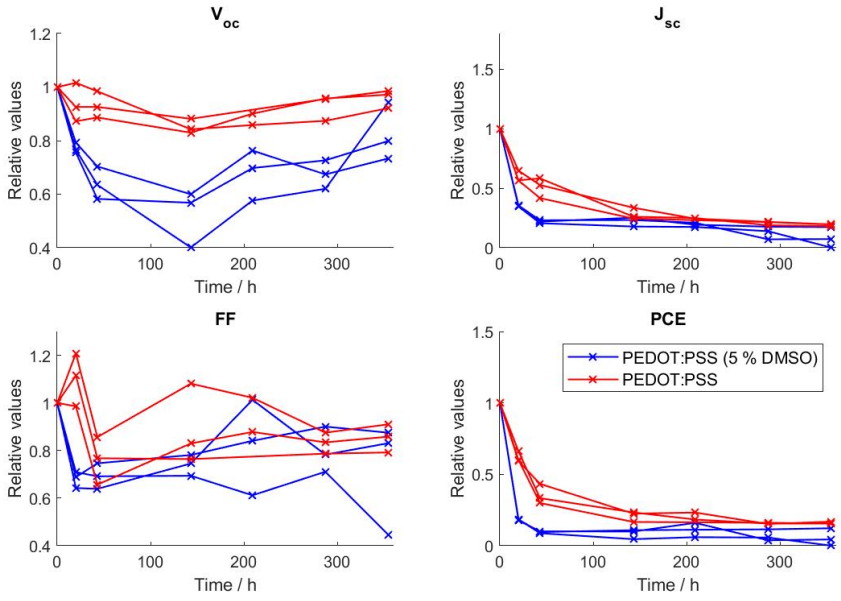

Figure 5.4: Change in solar cell parameters upon dark storage in dry air. Scan direction: reverse. 500 ms per step, scan speed 26 mV/s. Light source: Dedolight.

5.4 Degradation of the silver electrodes: Effect of electric fields

Figure 5.5 shows a photo of two of the samples that were subjected to shelf life testing, one that was stored in nitrogen atmosphere and one that was aged in dry air. For the latter, a slight blurring of the electrodes around the edges is visible. The electrode of the cell whose JV-characteristics were repeatedly measured (marked with a pink circle) darkened noticeably, indicating a degradation of the silver electrode. Apparently, the presence of electric fields and/or current flow has an effect on the degradation. It either speeds up the process or introduces new degradation pathways.

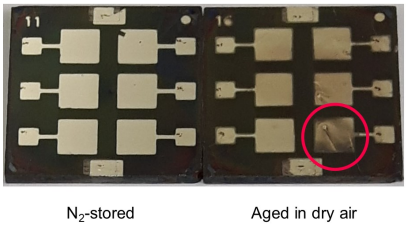

Figure 5.5: Photo of a device stored inside the glovebox and a device stored in dry air (both with PEDOT:PSS as HTL) after 350 hours.

5.5 Structural changes (XRD)

An interesting result was obtained by comparing the XRD pattern of an almost fully degraded cell stored in dry air and a reference cell whose efficiency had even improved over the monitored period. Even though the cells differ greatly in terms of performance, only small differences are revealed in their bulk crystal structure. In the air-aged cell, a small additional peak at 11.3 ° emerges, while the peaks assigned to the perovskite structure slightly decrease in height. Apparently, the observed degradation upon exposure to (dry) air is not predominantly caused by a change in bulk structure. This suggests that degradation mainly happens at the interface(s) whose volume is not large enough to affect the XRD. It would certainly be interesting to know how the bulk crystal structure looked before the cells were aged. However, no XRD measurements were taken before the stability tests because they would have required undesirable exposure of the cells to ambient air.

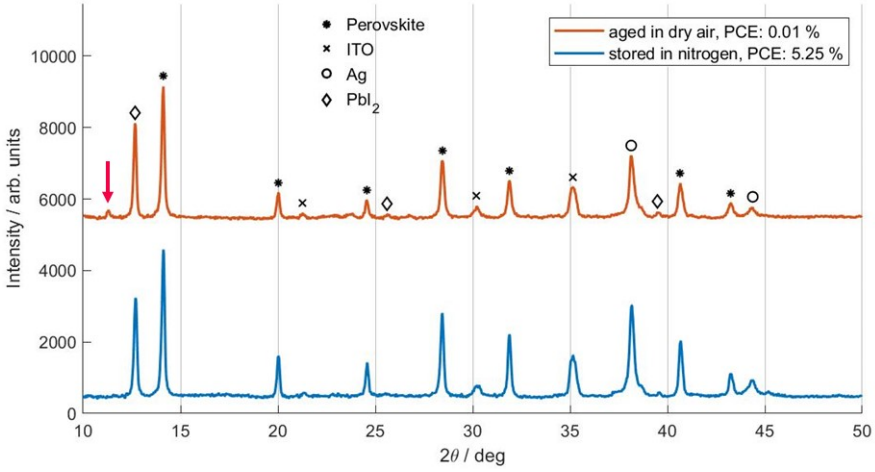

Figure 5.6: Comparison of XRD pattern of devices with PEDOT:PSS (5 % DMSO) as HTL after 350 hours dark storage in nitrogen atmosphere and dry air respectively. Instrument: Rigaku. PCE values were measured in reverse direction, 500 ms per step, scan speed 26 mV/s.

5.6 Transient behaviour of JV-curves

The observation that solar cell parameters greatly depend on the scan direction as well as on the illumination time initiated further measurements striving to elucidate this peculiar behaviour. They were performed after 200 hours dark storage subsequent to the regular JV-measurements. After 4 consecutive JV-scans (with the following sequence of scan directions: forward-reverse-forward-reverse), the steady-state current was measured at several voltage points between the V_{oc} and the V_{mpp}. This was done by allowing the cell to stabilise at the particular voltage for 60 s before recording the current. For a stabilised cell, one would expect the consecutive forward scans, as well as the consecutive reverse scans, to coincide.

There might be a difference between the forward and reverse scans due to hysteresis. The steady state should lie somewhere in between the two scan directions, as was successfully demonstrated by Christians et al. [126].

However, neither the cells aged in dry air (Fig. 5.7) and nor those stored in nitrogen atmosphere (Fig. 5.8) exhibit this behaviour. Instead, the JV-curves appear to shift towards the steady-state over time, indicating that the cells undergo internal changes upon illumination until they reach a stabilised state. This transient change is most pronounced for the cells with 5 % DMSO. It even proceeds in opposing directions, depending on the degradation state of the samples. For cells aged in dry air, the efficiency drops upon illumination due to a decrease in both I_{sc} and V_{oc}. However, if the cells have not come into contact with air, the I_{sc} greatly improves upon illumination, while the V_{oc} remains fairly constant. Since the magnitude of the shift is much smaller for devices with pure PEDOT:PSS (see Fig. 5.7b and 5.8b), one can conclude that the change in the JV-curve is due to changes in the HTL. Apparently, light quite strongly alters the properties of DMSO-doped PEDOT:PSS. The increase in I_{sc} for the non-degraded cell (Fig. 5.8a) suggests that illumination enhances the conductivity of the HTL. However, in combination with air exposure, light seems to be detrimental to both the V_{oc} and the I_{sc}. As much as the addition of DMSO to PEDOT:PSS initially seems to boost the cell's efficiency, it seems to increase its instability towards air.

The case of pure PEDOT:PSS is different in the way that the shift is in the same direction for both the air-aged cell and the non-degraded cell, and that it is much smaller in extent. In Figure 5.7b, the second pair of JV-scans (forward and reverse) almost coincide with the steady-state values, suggesting that the cell has already reached its stabilised state.

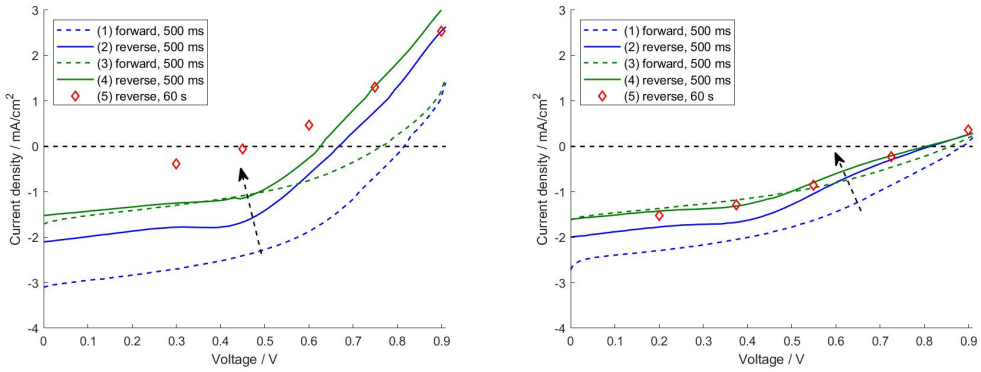

(a) PEDOT:PSS (5 % DMSO)

(b) PEDOT:PSS

Figure 5.7: Transient behaviour of JV-curves for devices aged in dry air. Scans were measured in the chronological order (1)-(5). Time per voltage step given in ms. Light source: Dedolight.

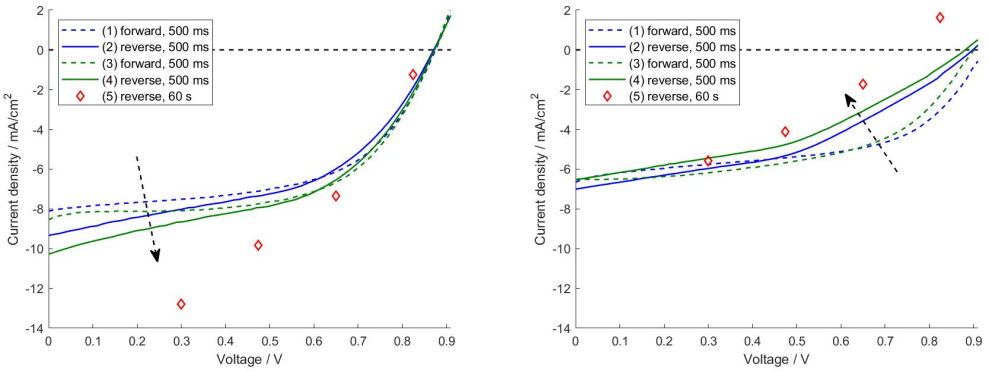

(a) PEDOT:PSS (5 % DMSO)

(b) PEDOT:PSS

Figure 5.8: Transient behaviour of JV-curves for reference devices stored inside the glovebox. Scans were measured in the chronological order (1)-(5). Time per voltage step given in ms. Light source: Dedolight.

5.7 Conclusion

In this section, the influence of storage conditions on the stability of perovskite solar cells with PEDOT:PSS (with and without DMSO added) were investigated. Dark storage testing was carried out in an inert nitrogen atmosphere and in dry air over a time period of 350 hours.

It could be demonstrated that approximately 2/3 of the devices stored in the dark in inert atmosphere remained reasonably stable, indicating that internal chemical reactions or ion diffusion processes do not occur on a large scale without any external influences such as oxygen, light, moisture or electric fields.

Exposure to dry air (i.e. oxygen) was shown to induce rapid degradation in all investigated devices, though those with DMSO-doped PEDOT:PSS were observed to degrade slightly faster. After 350 hours, all cells had lost over 80 % of their initial efficiency. A comparison of XRD results for thus degraded cells and fully intact nitrogen-stored cells revealed only small differences (see section 5.5). This indicates that the main cause of degradation is not a change of the bulk crystal structure but might be located at the interfaces or in volumes too small to show up in XRD. It was also shown (section 5.4) that electric fields speed up the degradation of the top silver electrodes.

Proper quantification of the degradation has proven difficult because the determination of the solar cell parameters requires exposure to light and the cells were observed to be quite unstable towards illumination. One can therefore either measure the cell as close to its dark state as possible by keeping measurement and illumination times short (which was tried for this thesis), or one can attempt to measure the steady-state (e.g. by very slow scan speeds or MPP-tracking) which requires longer illumination times and moves the cell away from its dark state. In addition, if the illumination times are too long, they might induce degradational changes. That way the testing conditions for 'dark storage' would not be fulfilled anymore. Furthermore, light is known to play an important role in oxygen-induced degradation (see section 1.3.2). It can therefore be expected that exposing cells that were stored in dry air and are most likely saturated with oxygen to light will significantly speed

up degradation. To better understand the role these factors play during dark storage testing, further experiments are required. The metastable behaviour of perovskite solar cells upon exposure to light is discussed in more detail in section 6.

Chapter 6

Stability towards light for different HTLs

6.1 Introduction

Previous results discussed in section 3.6.5 and 5.6 have already shown that perovskite solar cells respond to illumination. This section discusses the cells' stability towards light in greater detail.

In general, a solar cell can respond in 3 different ways to illumination. In the ideal case, the cell does not show any light-induced changes and is therefore stable towards illumination. If a response can be observed, it can take two different forms. Either the change is permanent (unstable behaviour) or it is reversible upon removal of the stressor (metastable behaviour). Metastable effects upon illumination are already known from other thin-film photovoltaic technologies, such as CIGS or CdTe-cells, where they were traced back to point defects (see section 1.4.3).

To investigate the stability of perovskite solar cells towards illumination, light/dark soaking experiments in different atmospheres were performed, as well as MPP-tracking. The measurements were carried out for cells with different hole transport layers so as to determine the impact of the hole transport layer on the cells' stability behaviour. Cells with organic PEDOT:PSS (with and without addition of DMSO) as HTL were compared to cells with an inorganic NiO_x layer.

6.2 Light/Dark soaking

Light/dark soaking allows to investigate the stability of perovskite solar cells towards illumination at open circuit conditions, i.e. without any current flow. During light (dark) soaking the cells are continuously illuminated (kept in the dark). At regular intervals, their JV-curves are measured. In between the measurements, the solar cell is kept at open circuit.

Light soaking experiments were carried out in different atmospheres (see below) and for different hole transport layers (PEDOT:PSS and NiO_x) to investigate the impact of the transport layer on the light soaking behaviour. Since exchanging the hole transport layer

completely alters the interface and defect properties, it is likely that the choice of hole transport layer plays a large role in determining the cell's stability towards light.

6.2.1 Different atmospheres

For this thesis, light soaking experiments were carried out in an inert nitrogen atmosphere and in ambient air. The measurements performed in inert atmosphere were designed to simulate the case of a perfect encapsulation where the cell is fully protected from oxygen and humidity. During light soaking, the cell is only exposed to light, and to some extent to internal heating (see section 6.2.3). To investigate the stability of perovskite solar cells towards illumination in the presence of oxygen and humidity, light soaking experiments were also performed in ambient air. According to literature, the combination of oxygen and light should lead to rapid degradation of the devices (see section 1.3.2). To slow down this degradation, some of the devices were encapsulated with epoxy glue (see section 3.5). In the ideal case of a perfect encapsulation, the results for the encapsulated devices should equal those for the inert atmosphere. Thus, conclusions on the effectiveness of the encapsulation can be drawn.

6.2.2 Measurement routine

For the light/dark soaking experiments performed within this thesis, a 10-hour light soaking period was followed by 8 hours dark soaking to investigate the cell's relaxation behaviour. The length of the light/dark soaking periods was chosen so that the measurements could be performed overnight. The intervals between JV-scans were about 1 minute at the beginning of the light/dark soaking process and subsequently increased to 15 min and 30 min for light and dark soaking respectively so as to minimize the influence of the measurements on the cell.

For the light/dark soaking measurements carried out in nitrogen atmosphere, the JV-setup at the TU Graz was used (see section 2.2.1). JV-scans were performed in forward direction at a scan rate of 200 ms/V. The reason for the fast scan rate was to keep the measurement time small relative to the time intervals between the scans. Before and after the light/dark soaking process, the devices were characterised by XRD and EQE measurements.

For the light soaking measurements carried out in ambient air (encapsulated and unencapsulated), the JV-setup at the AIT in Vienna was used (see section 2.2.1). JV-scans were performed in forward direction at a scan rate of 250 ms/V. After each scan, the V_{oc} and J_{sc} were measured directly to achieve a higher accuracy. In the results, these directly obtained values are used instead of the ones derived from the JV-scan. The unencapsulated devices were characterised by XRD and SEM measurements before and after the light/dark soaking process.

6.2.3 The effect of temperature

Usually, light soaking experiments are carried out in standard conditions (i.e. at 25 °C). However, cooling of the cells was not possible for this thesis' work. Since the solar cells are illuminated from one side but contacted from the other side, i.e. the electrodes are positioned on the substrate side facing away from the incident light, the devices could not

simply be placed on top of a cooling plate. To monitor the temperature change during light/dark soaking, a temperature sensor was attached to the cell's glass substrate for a measurement in ambient air. During the light soaking phase, the cell temperature rose up to 55 °C and dropped back down to 25 °C during dark soaking. A similar temperature curve can be expected for light/dark soaking in an inert atmosphere.

To investigate the influence of the elevated temperature on device stability, two reference devices, one encapsulated and one unencapsulated, were subjected to tempering at 55 °C in the dark for several hours. The reference devices had PEDOT:PSS (5 % DMSO) as hole transport layer. Tempering was performed in an oven in ambient atmosphere. At regular intervals, XRD- and JV-characterisation was performed to monitor the stability of the devices.

No change could be found in their XRD pattern, indicating that the bulk crystal structure remained stable upon tempering. Figure 6.1a shows the JV-curves measured at different instants throughout the tempering for the encapsulated device. No significant change is visible, confirming that the cell is unaffected by the temperature exposure. The unencapsulated device (Fig. 6.1b) exhibit a slight reduction in J_{sc} upon tempering, as well as a change in V_{oc}. The open-circuit voltage initially increases upon temperature exposure, followed by a decrease that appears to be caused mainly by a change in curvature around the intercept with the x-axis. Evidently, the device undergoes a change throughout the tempering experiment. However, it is possible that these changes are a result of oxygen exposure rather than increased device temperature, an assumption that is supported by the fact that the encapsulated device remained unchanged.

In conclusion, based on the results described above, it can be safely assumed that the elevated temperature present during the light soaking experiments does not result in device degradation on its own. It cannot be ruled out, however, that the elevated temperature accelerates degradation mechanisms driven by light, oxygen and/or humidity.

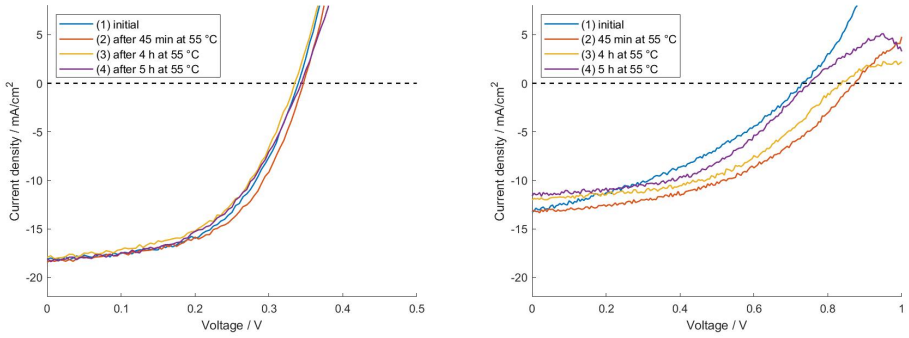

(a) encapsulated (b) unencapsulated

Figure 6.1: Change in JV-curves upon dark storage at 55 °C in ambient air for an encapsulated and an unencapsulated cell with PEDOT:PSS (5 % DMSO) as HTL. Scan direction: reverse. Scan speed: 250 mV/s. Light source: solar simulator.

6.3 Light/Dark soaking for cells with PEDOT:PSS

The following section presents and discusses the results of light/dark soaking for cells with PEDOT:PSS (both pure and with DMSO added) as hole transport layer in the different atmospheres.

6.3.1 Inert atmosphere

Figure 6.2 shows the evolution of the most important solar cell parameters, namely PCE, V_{oc}, J_{sc} and FF, during light/dark soaking, plotted both on a linear and a logarithmic time scale. For the logarithmic time scale, the time axis was reset to zero at the beginning of the dark soaking period to emphasize the initial response of the cell to the change of lighting conditions. All values have been normalized to their initial ones to visualise their relative change. A strong metastable behaviour that is superimposed by an irreversible part can be seen. Upon light soaking, the efficiency goes up by a factor larger than 3 until it reaches a saturation value. During dark soaking, it drops back down, ending up at 1.5 times its initial value. The metastable behaviour of the efficiency appear to be driven mainly by the metastability in V_{oc}. The open-circuit voltage rises by a factor of 2 upon illumination, a change that is almost fully reversible upon dark soaking. The irreversible part of the PCE-curve is due to the irreversible behaviour of the FF. It also increases upon light soaking but does not revert back to its original value during the dark soaking phase. The increase in FF might correspond to a reduction in series resistance. The short-circuit current density J_{sc} shows a metastable behaviour similar to that of the V_{oc}, though much smaller in magnitude.

The change in V_{oc} is also clearly recognisable in Figure 6.3. It shows the JV-scans at different instants throughout the light/dark soaking effect. After dark storage, the V_{oc} is about 0.45 V but it increases to almost 0.9 V upon illumination.

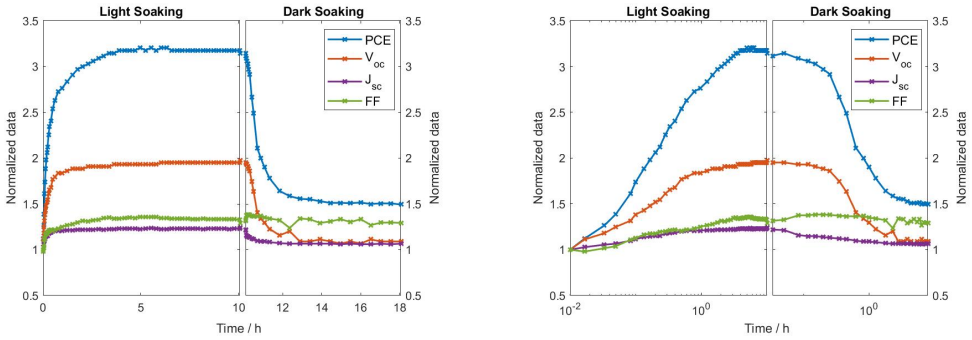

(a) linear time scale

(b) logarithmic time scale

Figure 6.2: 10 hours light soaking + 8 hours dark soaking for a cell with PEDOT:PSS as HTL in nitrogen atmosphere. (a) linear time scale, (b) logarithmic time scale. Light source: Dedolight.

The results of light/dark soaking in inert atmosphere, clearly shows that exposure to illumination does not lead to degradation in cells with PEDOT:PSS as a HTL within the observed period of time. On the contrary, the measured device significantly improved,

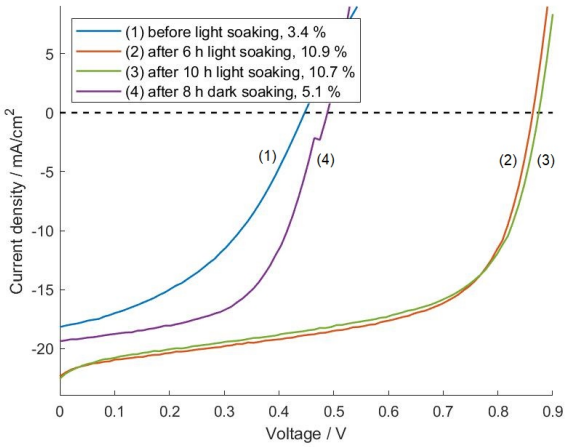

Figure 6.3: JV-scans of a cell with PEDOT:PSS as HTL at different instants throughout the light/dark soaking process in nitrogen atmosphere. Line (2) corresponds to the maximum PCE that was reached.

especially in terms of its fill factor. A strong metastable behaviour is observable in the V_{oc}, which is in agreement with results reported in literature (see section 1.4.3 and Zhao et al. [101]). However, the behaviour of the J_{sc} differs from that observed by Zhao et al. In their light soaking experiments, the J_{sc} showed an initial increase followed by a decrease, while no decrease is present in the results obtained for this thesis. The reason might be slight differences in device architecture. Zhao et al. used identical hole and electron transport layers but instead of a triple cation perovskite they used the simpler structure $MAPbI_3$.

Structural changes (XRD)

No change could be observed in the XRD-pattern measured before and after light soaking, indicating that changes occurring inside the device do not concern the large-volume bulk crystal structure. They might, however, take place at the interfaces or in volumes too small to show up in the XRD.

EQE measurements

EQE measurements were performed before and after the light/dark soaking experiment. To gain some information on the reproducibility, EQE spectra of a reference cell were measured in addition to the light-soaked cell. The reference cell was located on the same substrate as the light-soaked cell, and thus exposed to the same light conditions, but its JV-curve was not monitored during the experiment. Before each EQE measurement, the J_{sc} of the cells were measured directly using the JV-setup and subsequently compared to the values calculated from the respective EQE spectra. In an ideal case, the two values are equal. However, since the light intensity greatly differs in the two experimental setups - 100 mW/cm^2 for the JV-scan and a much lower value for the EQE measurements - and only part of the active cell area is illuminated during EQE measurements, recombination mechanisms as well as

microshunts might play a more dominant role in the EQE setup resulting in a lower current output.

The measured EQE spectra are displayed in Figure 6.4. After light soaking an overall shift of the EQE is visible but the shape of the spectra remains unchanged which indicates that no major structural changes in the absorber material take place. The shift of the EQE spectra might be due to a change in charge extraction efficiency but it might also be caused by slight differences in the positioning of the monochromatic light source. The fact that the directly measured J_{sc} remains stable for the light-soaked cell (see table 6.1) might be an indication that the change in the J_{sc} derived from the EQE stems from imperfect light source positioning rather than from internal changes in the cell.

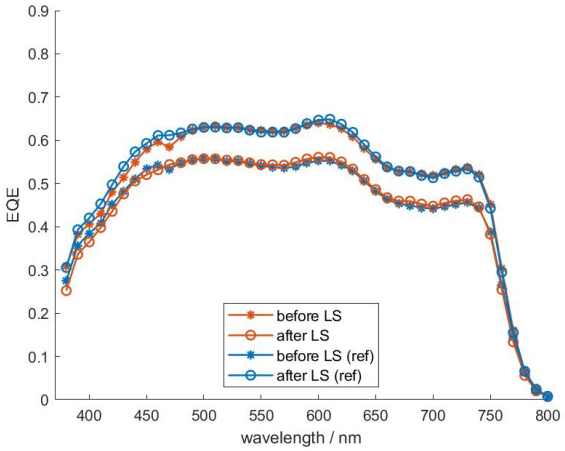

Figure 6.4: EQE spectra measured before and after light soaking (LS) in nitrogen atmosphere for a cell with PEDOT:PSS as HTL. The reference cell (ref) was kept at open circuit at all times.

Table 6.1: Comparison between directly measured J_{sc} and the J_{sc} derived from the EQE spectrum for light/dark soaked cell with PEDOT:PSS as HTL. (ref) represents the reference cell that was kept at open circuit at all times during light/dark soaking.

	J_{sc} direct / mA/cm^2	J_{sc} EQE / mA/cm^2	J_{sc} direct : J_{sc} EQE
before light soaking	18.7	13.5	1.38
after light soaking	18.7	11.9	1.58
before light soaking (ref)	16.7	11.8	1.42
after light soaking (ref)	18.7	13.6	1.38

Conclusion

To sum up, a strong metastable behaviour upon light soaking in inert atmosphere could be demonstrated for perovskite solar cells with PEDOT:PSS as HTL. Invoked changes were to a large extent reversible. The irreversible part resulted in an overall improvement of the cell over the course of the experiment. No significant alterations in the XRD-measurements or the EQE-spectra could be observed, indicating that the improvement in cell efficiency did not involve permanent changes in the bulk perovskite structure. Instead, it might have been caused by a light-induced post-ordering in one of the thin transport layers, an alteration of the interfaces or a change in defect densities. The reversible, metastable behaviour is most likely electrically driven. A change in V_{oc} usually corresponds to a change in the built-in electric field. And such a change in electric field could be caused by a change of charge accumulations at the interfaces, the neutralisation of defect or trap states by photo-generated charge carriers or ion migration.

6.3.2 Encapsulated device

Light/dark soaking for an encapsulated device was performed for two different variants of PEDOT:PSS hole transport layers: a pure PEDOT:PSS layer and a PEDOT:PSS layer doped with 5 % DMSO. The results of the light/dark soaking experiments can be found in Figure 6.5-6.6. Unlike the results in inert atmosphere, the evolution of the fill factor is not displayed for the light soaking measurements carried out in ambient air because the derived values strongly fluctuate and cannot be used to draw any conclusions on the state of the solar cell. For the measurements in ambient air, J_{sc} and V_{oc} were measured

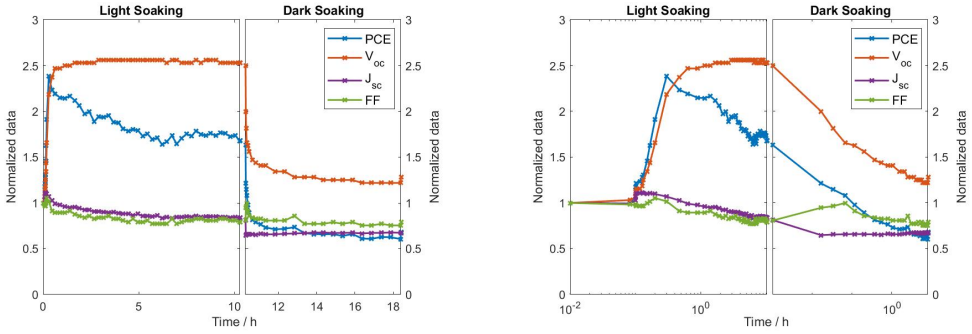

(a) linear time scale

(b) logarithmic time scale

Figure 6.5: 10 hours light soaking + 8 hours dark soaking for an encapsulated cell with **PEDOT:PSS (5 % DMSO)** as HTL in ambient air. Light source: solar simulator.

Similar to the measurements in inert atmosphere, both cells show a strong metastable behaviour in their V_{oc}. Again, the light-induced change is to a large extent reversible with a small irreversible part that results in an overall improvement of the V_{oc} upon the light/dark soaking experiment. However, this time, the metastability is superimposed by a degradation in the short-circuit current density J_{sc}, causing an overall drop in efficiency

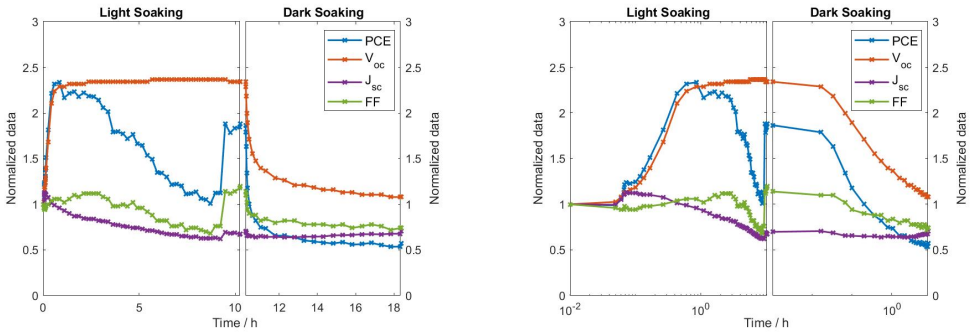

(a) linear time scale (b) logarithmic time scale

Figure 6.6: 10 hours light soaking + 8 hours dark soaking for an encapsulated cell with **PEDOT:PSS** as HTL in ambient air. Light source: solar simulator.

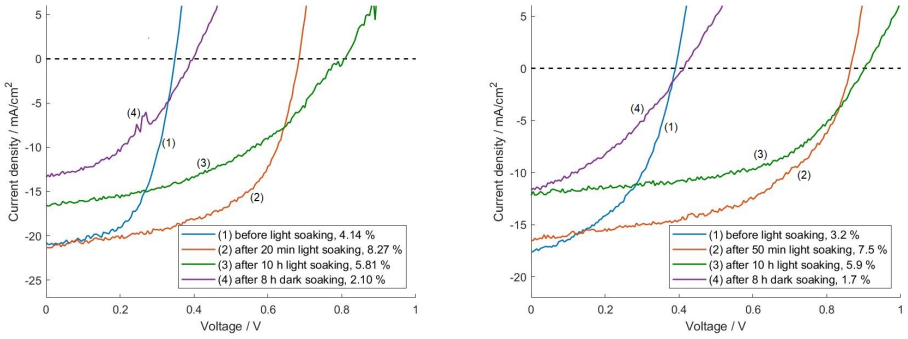

(a) PEDOT:PSS (5 % DMSO) (b) pure PEDOT:PSS

Figure 6.7: JV-scans of two encapsulated cells (one with PEDOT:PSS (5 % DMSO) and one with pure PEDOT:PSS as HTL) at different instants throughout the light/dark soaking process in ambient air. Line (2) corresponds to the maximum PCE that was reached.

by almost 50 %. It can be noted that the general behaviour is the same for both cells, and therefore independent of the addition of DMSO. The temporary drops in the PCE-curve in Figure 6.6 were most likely caused by a bad electrical contact.

When compared to the results for inert atmosphere, the light-induced increase in V_{oc} is stronger in magnitude (factor 2.5 instead of 2). This is because the encapsulated devices started at a lower initial voltage, an effect caused by the encapsulant (see section 3.5).

The fact that irreversible degradation occurs in the short-circuit current density J_{sc} demonstrates that the encapsulation does not sufficiently protect the cell. Degradation only takes place while the cell is exposed to light. However, since no degradation was observable in inert atmosphere, it cannot be the influence of light alone that deteriorates the device. There are two possible culprits: either the encapsulant reacts with the cell under illumination or, more likely, the encapsulation allows for sufficient oxygen ingress so that the combination

of light and oxygen is responsible for the degradation (according to the mechanism described in section 1.3.2).

Figure 6.7 shows JV-scans that were extracted from the light/dark soaking measurements at representative instants, i.e. before light soaking, at the maximum PCE, after light soaking and after dark soaking. The metastable behaviour of V_{oc} as well as the degradation in J_{sc} are clearly visible.

6.3.3 Ambient air

Analogous to the measurements for encapsulated devices, light/dark soaking in ambient air was performed for the same two variants of a PEDOT:PSS hole transport layer: a pure PEDOT:PSS layer and a PEDOT:PSS layer doped with 5 % DMSO.

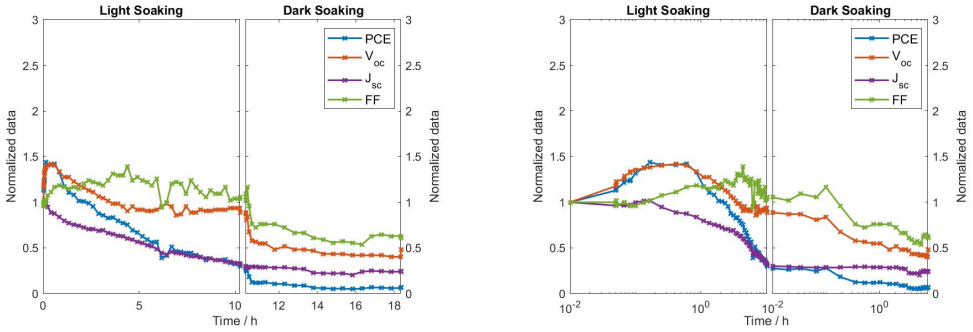

(a) linear time scale (b) logarithmic time scale

Figure 6.8: 10 hours light soaking + 8 hours dark soaking for an unencapsulated cell with **PEDOT:PSS (5 % DMSO)** as HTL in ambient air. Light source: solar simulator.

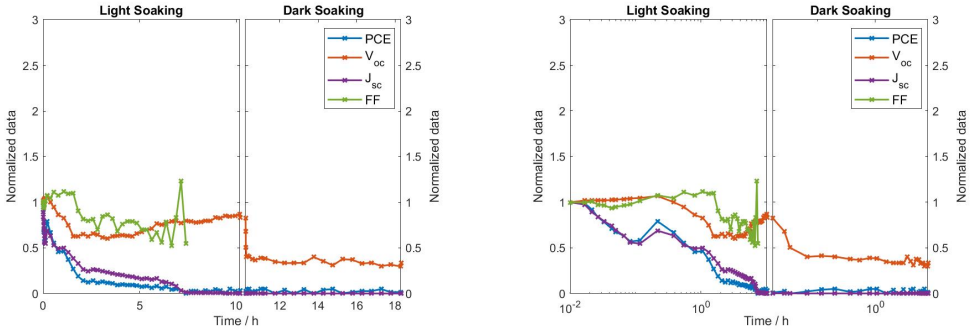

(a) linear time scale (b) logarithmic time scale

Figure 6.9: 10 hours light soaking + 8 hours dark soaking for an **unencapsulated** cell with **PEDOT:PSS** as HTL in ambient air. Light source: solar simulator.

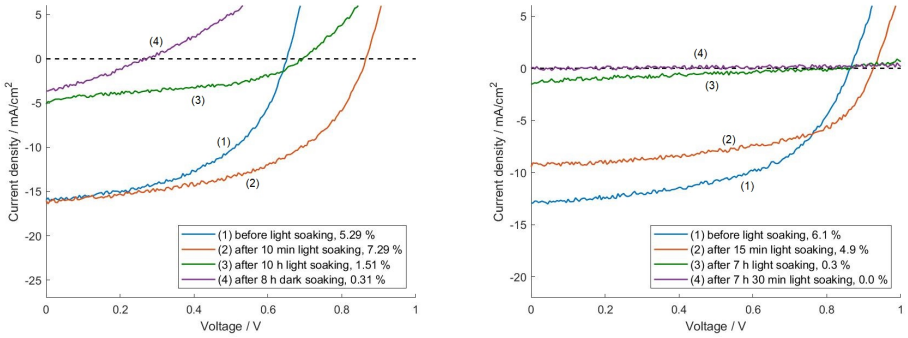

(a) PEDOT:PSS (5 % DMSO) (b) pure PEDOT:PSS

Figure 6.10: JV-scan of two unencapsulated cells (one with PEDOT:PSS (5 % DMSO) and the other with pure PEDOT:PSS as HTL) at three different instants of the light/dark soaking process in ambient air.

The results of the light/dark soaking experiments can be found in Figure 6.8-6.9. They show quite clearly that the combined exposure to light and oxygen (and to some degree to the humidity present in ambient air) is too much for the perovskite solar cells. The device with pure PEDOT:PSS fully degraded within 7 hours, while the DMSO-doped device lost over 90 % of its initial efficiency. Rudimentarily, the metastable behaviour of the V_{oc} can be observed but it is almost fully quenched by the rapid degradation. For the cell with pure PEDOT:PSS, the fill factor cannot be defined in a meaningful way anymore after the J_{sc} has dropped to zero.

Degradation of the silver electrode

A visual inspection of the devices after the light soaking experiment revealed a severe degradation of the silver electrodes for some of the cells on the substrates (see Fig. 6.11).

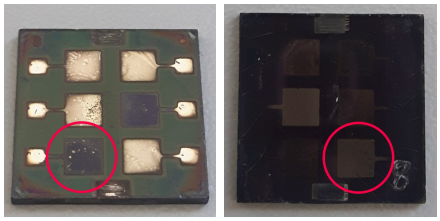

(a) top view (b) bottom view

Figure 6.11: Photos of a sample with PEDOT:PSS as HTL after light/dark soaking in ambient air. The whole cell was under illumination, but only the marked cell was repeatedly measured. Top (bottom) view: Ag electrode (glass substrate) facing upwards.

For the cell whose light/dark soaking behaviour was tracked (indicated by a pink circle in Fig. 6.11), the electrode appears to have etched through the whole device, making it visible from the back side. However, etching did also occur to different extents for the other cells on

the substrate that were kept at open circuit throughout the light/dark soaking experiment. This indicates that the current flow and/or change in electric fields present throughout the JV-scans cannot be the main driver for this degradation process.

Etching of the metal electrode has already been observed by You et al. [90] (see section 1.3.5) upon storing their devices in ambient air. They ascribed the etching to a chemical reaction of the perovskite with the metal electrode but found that an intermediate ZnO nanoparticle layer was able to block the reaction.

However, it seems that the additional exposure to light during the light/dark soaking process in this thesis has significantly enhanced the etching process. None of the other experiments (especially dark storage in dry air, light soaking in an inert atmosphere), performed for this thesis, lead to electrode etching, suggesting that the combination of ambient air and light is necessary to overcome the reaction barrier formed by ZnO. The blocking properties of ZnO should also depend on the thickness of the layer. In areas where the ZnO is thinner or insufficiently covers the perovskite, its blocking properties will be especially low. This might explain why etching for the different cells on the substrate took place at different speeds and to different extents.

Moreover, etching was only observed to occur in the active area of the cell. The contact pads at the edges appear to be unaffected. This indicates that electric fields and/or current flow might represent a driving factor in the process.

Structural changes (XRD)

The XRD characterisation revealed several additional peaks that appeared upon light/dark soaking in ambient air. Unfortunately, the peaks could not be assigned to a specific crystal structure. Apparently, the emerging peaks do not belong to any of the common compounds such as PbI_2, MAI, FAI etc. whose XRD pattern can be found in literature.

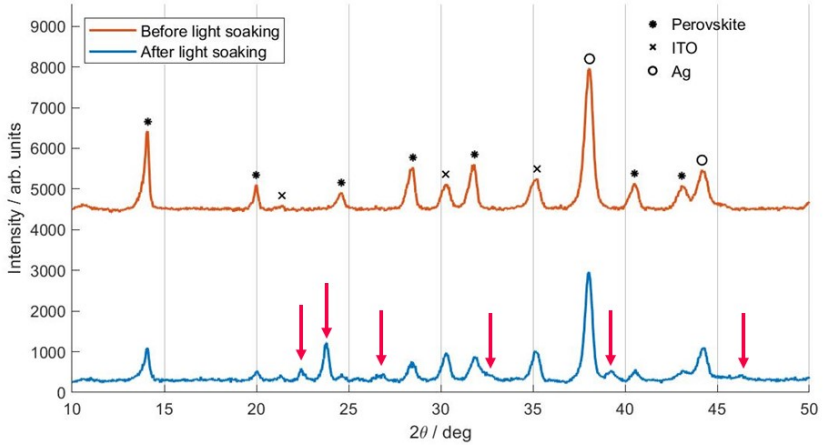

Figure 6.12: Change in the bulk crystal structure for a device with PEDOT:PSS as HTL upon light soaking. Instrument: ThermoScientific.

Table 6.2: Positions of XRD peaks appearing upon light/dark soaking of a cell with PEDOT:PSS as HTL in ambient air.

2θ / °
22.5
23.8
26.8
32.7
39.3
46.3

6.4 Light/Dark soaking for cells with NiO_x

Light/dark soaking experiments were performed on cells with NiO_x as hole transport layer in the exact same manner as on cells with PEDOT:PSS.

6.4.1 Inert atmosphere

The results for the light/dark soaking measurement in inert atmosphere can be found in Figure 6.13, both on a linear and a logarithmic time scale. Compared to cells with PEDOT:PSS, the response of the cell to illumination is much smaller and different in nature. For cells with PEDOT:PSS, the V_{oc} exhibited a huge metastable behaviour upon light exposure, whereas the open-circuit voltage is very stable for cells incorporating NiO_x as hole transport layer and shows only a small response to illumination. The fill factor exhibits an irreversible increase upon light soaking, leading to an overall improvement of the cell efficiency by a factor larger than 1.5 throughout the whole cycle. A similar increase in fill factor was also observable for PEDOT:PSS but it was less pronounced. Differences between cells with PEDOT:PSS and NiO_x can also be seen in the short-circuit current density J_{sc}. While the J_{sc} followed the movement of the V_{oc} in cells with PEDOT:PSS, it shows a reverse light soaking effect for NiO_x. After an initial increase, the J_{sc} deteriorates upon light soaking, followed by a full recovery during the dark period.

Figure 6.14 shows JV-scans at different instants throughout the light/dark soaking effect. The increase in fill factor FF from line (1) to (4) can be clearly seen.

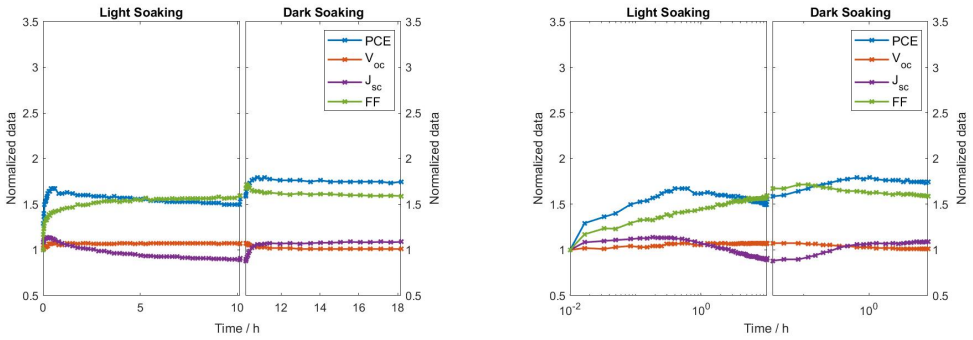

(a) linear time scale

(b) logarithmic time scale

Figure 6.13: 10 hours light soaking + 8 hours dark soaking for a cell with NiO_x as HTL in nitrogen atmosphere. Light source: Dedolight.

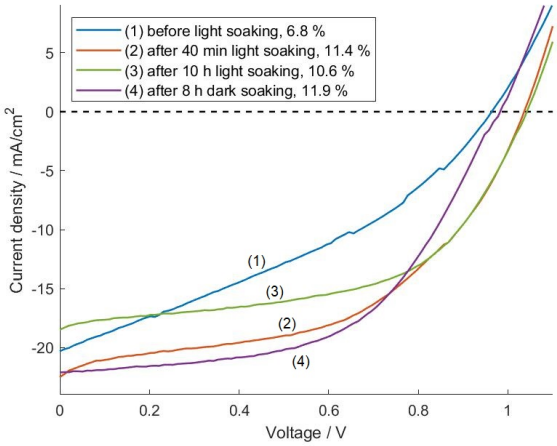

Figure 6.14: JV-scans of a cell with NiO_x as HTL at different instants throughout the light/dark soaking process in nitrogen atmosphere. Line (2) corresponds to the maximum PCE that was reached.

Structural changes (XRD)

Similar to cells with PEDOT:PSS, no change could be observed in the XRD pattern measured before and after light soaking. Here, too, irreversible changes that occurred throughout the light/dark soaking cycle do not concern the large-volume bulk crystal structure.

EQE measurements

EQE measurements were performed before and after the light/dark soaking experiment. Analogous to the measurements for cells with PEDOT:PSS, EQE spectra were acquired for the light-soaked cell and for a reference cell located on the same substrate. The results are displayed in Figure 6.15. The observed behaviour is similar to that of PEDOT:PSS, i.e. the

Table 6.3: Comparison between directly measured J_{sc} and the J_{sc} derived from the EQE spectrum for a light/dark soaked cell with NiO_x as HTL.

	J_{sc} direct / mA/cm^2	J_{sc} EQE / mA/cm^2	J_{sc} direct : J_{sc} EQE
before light soaking	18.0	17.2	1.05
after light soaking	18.4	15.9	1.16
before light soaking (ref)	16.6	17.1	0.97
after light soaking (ref)	14.9	16.0	0.93

shape of the spectra remains almost unchanged apart from a small overall shift in EQE.

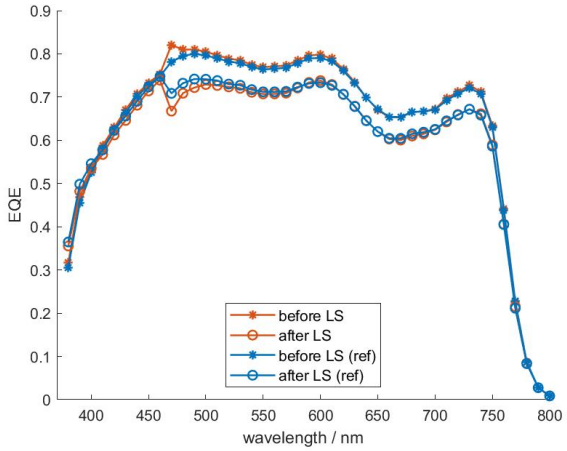

Figure 6.15: EQE spectra measured before and after light soaking in nitrogen atmosphere for a cell with NiO_x as HTL. The reference cell (ref) was kept at V_{oc} at all times.

Conclusion

It could be demonstrated that upon light exposure, cells with NiO_x behave quite differently from cells with PEDOT:PSS. The V_{oc} is much more stable and the J_{sc} shows a deterioration upon illumination of the cell that is fully reversible upon storage in the dark.

6.4.2 Encapsulated device

For the encapsulated device, the light soaking behaviour of cells with NiO_x (see Fig. 6.16) is quite similar to that observed in inert atmosphere. The only difference is that the degradation in J_{sc} is more severe and irreversible, indicating that permanent degradation occurs within the cell. Figure 6.17 shows JV-curves at different instants throughout the light/dark soaking cycle. Similar to the measurements in inert atmosphere, an increase in fill factor FF can be observed from line (1) to (4).

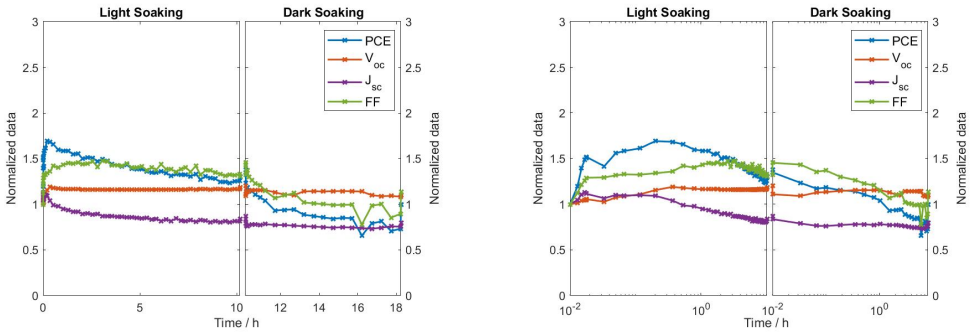

(a) linear time scale

(b) logarithmic time scale

Figure 6.16: 10 hours light soaking + 8 hours dark soaking for an **encapsulated** cell with NiO_x as HTL in ambient air. Light source: solar simulator.

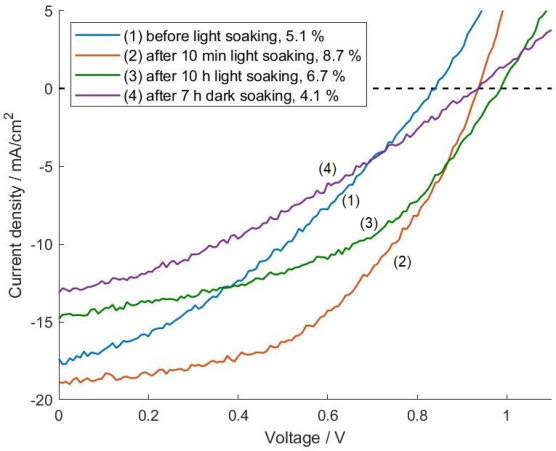

Figure 6.17: JV-scan of an encapsulated cell with NiO_x as HTL at different instants of the light/dark soaking process in ambient air. Line (2) corresponds to the maximum PCE that was reached.

6.4.3 Ambient air

Light soaking measurements in ambient air do not reveal that the cell with NiO_x are more stable (see Fig. 6.18). Combined exposure to light and ambient air results in complete degradation within 6 hours, a timescale similar to that observed for cells with PEDOT:PSS.

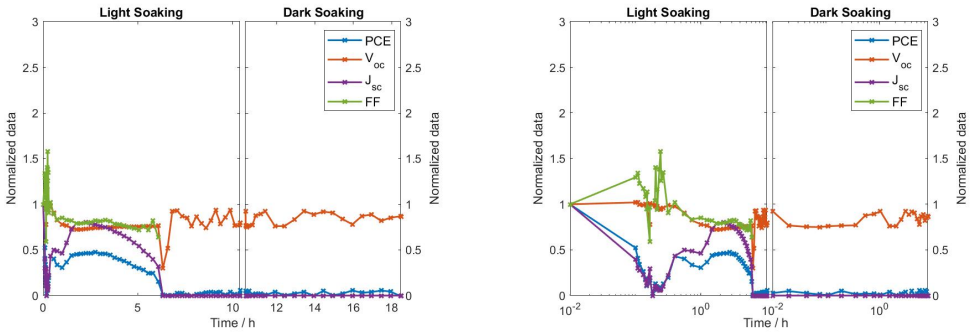

(a) linear time scale (b) logarithmic time scale

Figure 6.18: 10 hours light soaking + 8 hours dark soaking for an **unencapsulated** cell with NiO_x as HTL in ambient air. Light source: solar simulator.

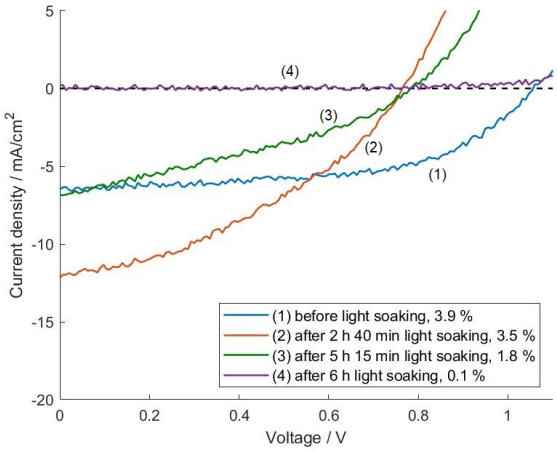

Figure 6.19: JV-scan of a cell with NiO_x as HTL at different instants of the light/dark soaking process in ambient air. Line (2) corresponds to the maximum PCE that was reached.

Degradation of the silver electrode

Taking a look at the visual appearance of the cell after the light/dark soaking cycle (Fig. 6.20) resolves any doubt as to why the cell is not working anymore. Similar to what has been observed for devices with PEDOT:PSS as hole transport layer, the cells with NiO_x display severe degradation of the silver electrode. The electrode of the light-soaked cell (marked with a pink circle) has darkened completely, as have some of the other cells on the substrate that were kept at open circuit during the light soaking process. The bottom view (Fig. 6.20b) shows that the silver electrodes have again partly etched through the whole device.

SEM images of the light-soaked cell reveal a curious effect. The edge of the underlying ITO electrode is clearly visible at the position of the silver electrode, and degradation of the silver electrode appears to be confined mainly to the active cell area.

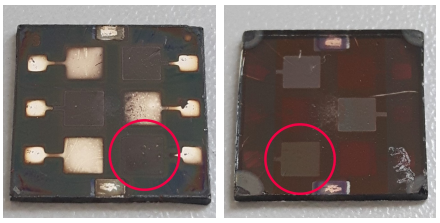

(a) top view (b) bottom view

Figure 6.20: Photos of sample with NiO_x as HTL after light/dark soaking in ambient air. The whole cell was under illumination, but only the marked cell was continuously measured. Top (bottom) view: Ag electrode (glass substrate) facing upwards.

A reason why this effect only occurred for cells with NiO_x but not for cells with PEDOT:PSS could be that the NiO_x-layer is much thinner than the PEDOT:PSS layer (20 nm compared to roughly 50 nm, see section 3.6.2), and thus less efficient in smoothing out the sharp edges of the ITO electrode that has a thickness of 120 nm.

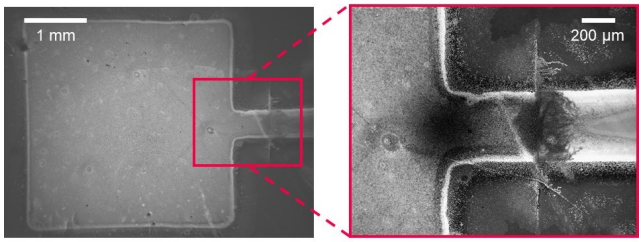

Figure 6.21: SEM images of an unencapsulated cell with NiO_x as HTL after light/dark soaking in ambient air. The edge of the ITO electrode is clearly visible.

Structural changes (XRD)

Evaluation of XRD measurements revealed the same additional peaks emerging upon the light/dark soaking process in ambient air as for the cell with PEDOT:PSS (see section 6.3.3).

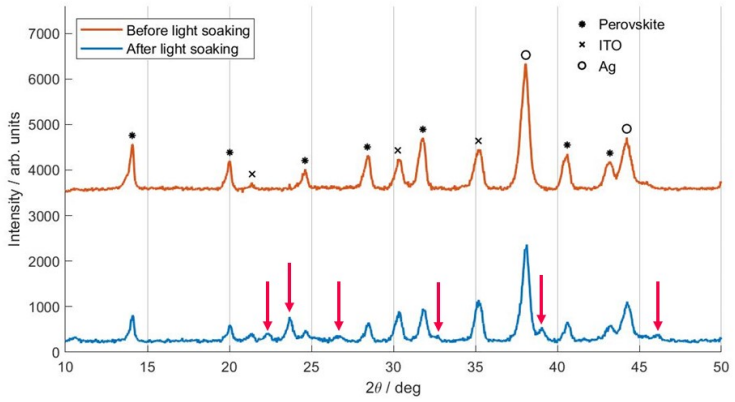

Figure 6.22: Change in the bulk crystal structure for an unencapsulated device with NiO_x as HTL upon light soaking in ambient air. Instrument: ThermoScientific.

Table 6.4: Positions of XRD peaks appearing upon light/dark soaking of a cell with NiO_x as HTL in ambient air.

2θ / °
22.3
23.7
26.7
32.6
39.1
46.1

6.5 Impact of hole transport layer on light soaking behaviour

Figure 6.23 shows the change in solar cell parameters upon light/dark soaking in inert atmosphere for both types of hole transport layer, PEDOT:PSS and NiO_x, in direct comparison. The results quite clearly show that the choice of hole transport layer plays an important role in determining the light soaking behaviour of the solar cells. Light-induced changes are much more pronounced in cells with PEDOT:PSS who exhibit a large metastable response especially in the open-circuit voltage V_{oc}. Cells with NiO_x, on the other hand, showed only very small changes in V_{oc}.

Even though no conclusion can be drawn regarding the microscopic mechanisms underlying the light soaking behaviour of the V_{oc}, it is clear from these results that the origin is in the hole transport layer, either in the layer itself or in the interfaces that are formed with the adjacent layers. Mechanisms that cause the steep increase of V_{oc} in cells with PEDOT:PSS are either not present in cells with NiO_x or counteracted by other effects. Based on experiences with similar effects in chalcogenide photovoltaics, it can be expected that defects play a large role in determining the light soaking behaviour. However, considering

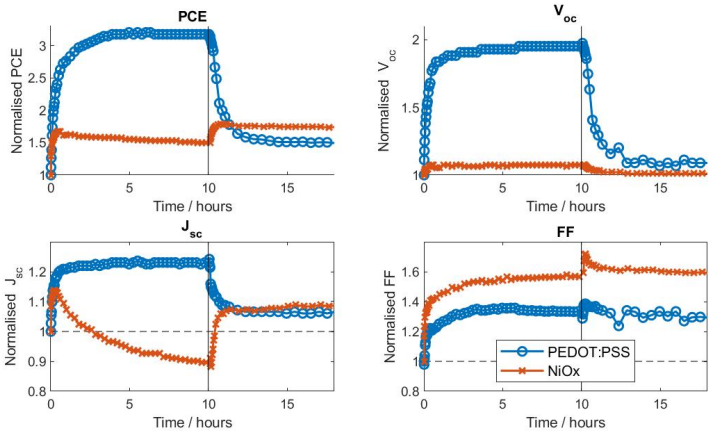

Figure 6.23: Comparison of light/dark soaking behaviour in inert atmosphere for cells with different HTLs. All cell parameters were normalised to their initial values.

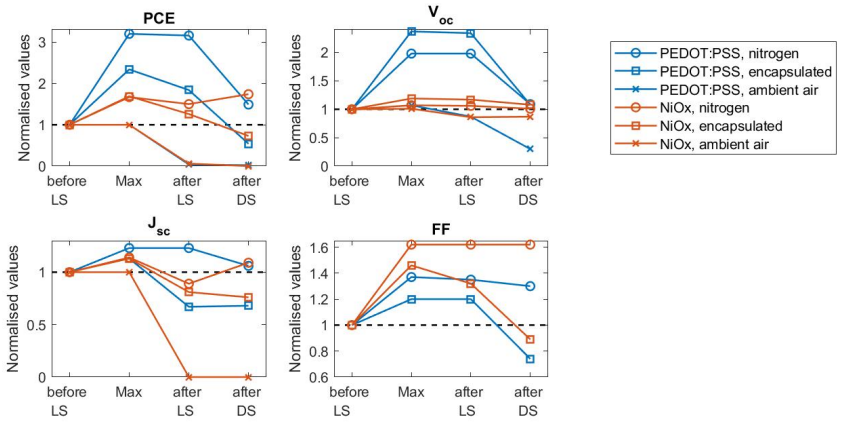

Figure 6.24: Comparison of solar cell parameters at specific instances throughout the light/dark soaking process for cells with different HTLs in different atmospheres. All cell parameters were normalised to their initial values. Light soaking for 10 h, followed by 8 h dark soaking. Max corresponds to the maximum values that was adopted throughout the light soaking phase.

that PEDOT:PSS is a polymer dispersion composed of two ionomers ($PEDOT^+$ and PSS^-), polarisation effects might also play a part.

The behaviour of the short-circuit current density J_{sc} also depends on the hole transport layer. While cells with PEDOT:PSS show a reversible light-induced increase that reaches saturation after roughly 1 hour, cells with NiO_x exhibit an initial rise but then drop upon continued illumination. However, in an inert atmosphere, this loss in current was shown to be reversible when the cell was stored in the dark again. Apparently, NiO_x introduces an additional mechanism that results in a reversible reduction of J_{sc} upon illumination and superposes the initial increase in current. Such an effect is not present in cells with

PEDOT:PSS.

Regarding the fill factor FF, the response to light and dark soaking is similar for both HTLs, though the effect is larger for cells with NiO_x. Upon light soaking, the fill factor increases until a saturation value is reached. In inert atmosphere, the change is irreversible upon dark soaking, resulting in an improved device performance after the completed light/dark soaking cycle.

When comparing the results for different atmospheres, it can be found that the encapsulated cells show the same tendency as the cells measured in inert atmosphere but the evolution is superposed by irreversible degradation. This agreement provides a first indication for the reproducibility of the results.

6.6 Operational Stability: MPP-tracking

During light soaking, the cells stability towards illumination at open circuit conditions was investigated. In MPP-tracking, the solar cell is operated at its maximum power point (MPP), so in addition to the light exposure, a current is constantly flowing through the device. This allows the investigation of the cell's operational stability. Analogous to the light soaking experiments, MPP-tracking was carried out for a cell with PEDOT:PSS and a cell with NiO_x to compare the long-term stability of the two. Because light soaking had already revealed that in ambient air cells undergo distinct degradation, whether they were encapsulated or not, within less than 20 hours, MPP-tracking was only performed in inert conditions.

6.6.1 Measurement routine

The MPP-measurements were performed with the JV setup at Graz (see section 2.2.1) and controlled by an additional Labview-based program. The starting V_{MPP} was determined by an initial JV-scan and readjusted at regular time intervals (looptime) by scanning a voltage range of 0.05 V around the current MPP. At the beginning of the measurements, the looptime was set to 5 s and subsequently increased to 20 s once the cell had sufficiently stabilised (after about an hour). Before and after MPP-tracking, the devices were characterised by JV-scans, XRD and EQE measurements.

6.7 MPP-tracking for a cell with PEDOT:PSS

Figure 6.25-6.26 show the results of MPP-tracking for a cell with PEDOT:PSS both on a linear and a logarithmic time scale. Within the first 10 hours, the cell's efficiency improves considerably (by a factor of ≈ 1.5). After that, degradation dominates and the PCE rapidly deteriorates, dropping below 50 % of the initial value before 90 hours have passed.

Figure 6.27a shows the JV-curves of the MPP-tracked cell measured before and after 87 hours of MPP-tracking. Before the MPP-tracking the cell was kept mainly in the dark but some light exposure did take place due to EQE and JV-characterisation. The JV-curve taken immediately after MPP-tracking shows that the main reason for the performance loss is not a decrease in V_{oc} or J_{sc} but a kink that appears in the curve, greatly reducing FF, V_{mpp}, J_{mpp} and thus PCE.

Figure 6.27b shows similar JV-curves for a reference cell that was located on the same substrate but kept at open circuit throughout the MPP-tracking procedure, i.e. it was basically light-soaked for 87 hours but without the regular JV-scans. The reference cell shows a similar kink after the illumination period, though it is less pronounced.

Both cells exhibit the characteristic metastable change of V_{oc} with respect to illumination (see Fig. 6.27) that has already been observed during the light soaking experiments. It would be interesting to investigate whether the light-induced shape change of the JV-curve is permanent or whether it can be reversed by storing the cell in the dark for a long enough time.

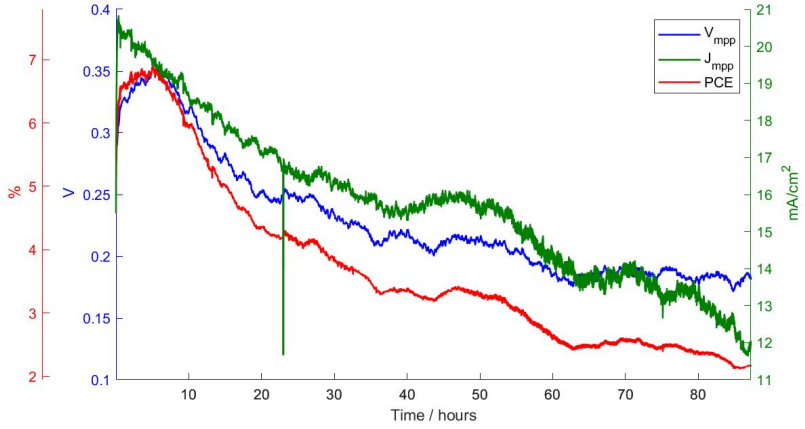

Figure 6.25: MPP-tracking of a cell with PEDOT:PSS as HTL in nitrogen atmosphere for 87 hours. Light source: Dedolight.

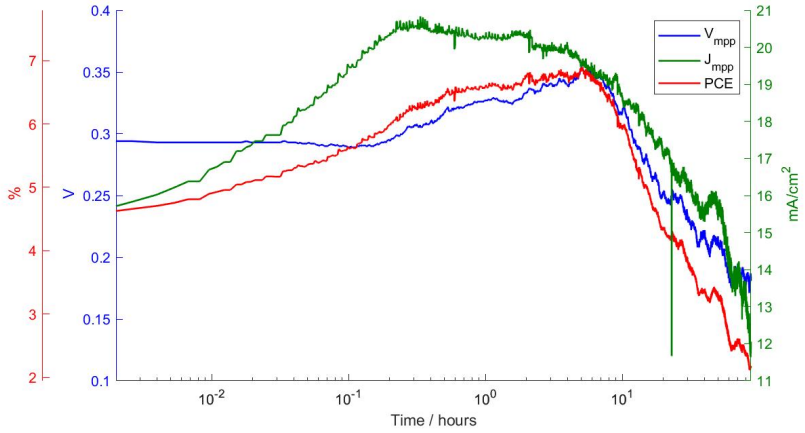

Figure 6.26: MPP-tracking of a cell with PEDOT:PSS as HTL in nitrogen atmosphere for 87 hours. Time is displayed in a logarithmic scale to emphasise the rapid, initial changes. Light source: Dedolight.

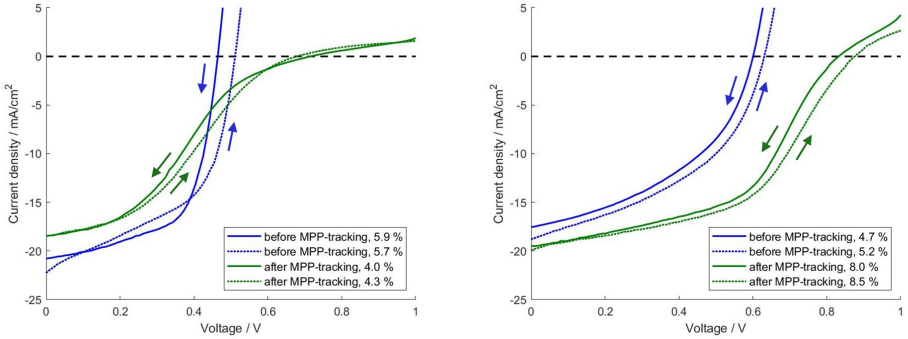

(a) MPP-tracked cell (b) reference cell

Figure 6.27: JV-curves of cells with PEDOT:PSS as HTL measured before and after MPP-tracking for 87 hours. Reference cell was only illuminated while being kept at V_{oc}. Scan direction: reverse (solid line), forward (dotted line). Scan rate: 100 mV/s. Light source: Dedolight.

6.7.1 EQE measurements

EQE measurements performed before and after MPP-tracking show a similar change for both the MPP-tracked and the light-soaked cell. After illumination for 87 hours, the efficiency is enhanced in the long-wavelength region and reduced towards the blue part of the spectrum. Table 6.5 lists the J_{sc}-values - directly measured and calculated from the EQE spectrum -

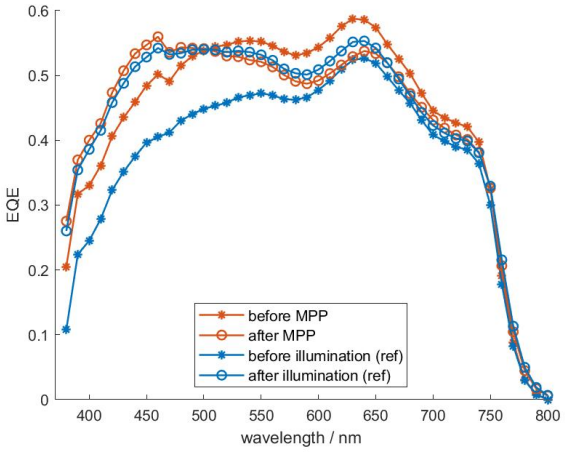

Figure 6.28: Effect of MPP-tracking (87 hours) in nitrogen atmosphere on EQE of a cell with PEDOT:PSS as HTL. The reference cell (ref) was illuminated while being kept at V_{oc}.

before and after the MPP-tracking experiment.

Table 6.5: Comparison between directly measured J_{sc} and the J_{sc} derived from the EQE spectrum for a MPP-tracked cell with PEDOT:PSS as HTL.

	J_{sc} direct / mA/cm^2	J_{sc} EQE / mA/cm^2	J_{sc} direct : J_{sc} EQE
before MPP-tracking	20.4	11.7	1.74
after MPP-tracking	18.5	11.5	1.60
before illumination (ref)	20.0	10.2	1.96
after illumination (ref)	19.5	11.6	1.68

6.7.2 Structural changes (XRD)

XRD measurements performed before and after MPP-tracking did not reveal any structural changes in the cell.

6.7.3 Comparison to light soaking results

Comparing the light soaking results to the first 10 hours of MPP-tracking (Fig. 6.29) shows that similar changes occur in both cases but to a very different extent. The increase in voltage is much larger for light soaking than for MPP-tracking. This dependence on load has already been observed for chalcogenide solar cells [102], as well as for perovskite cells [99].

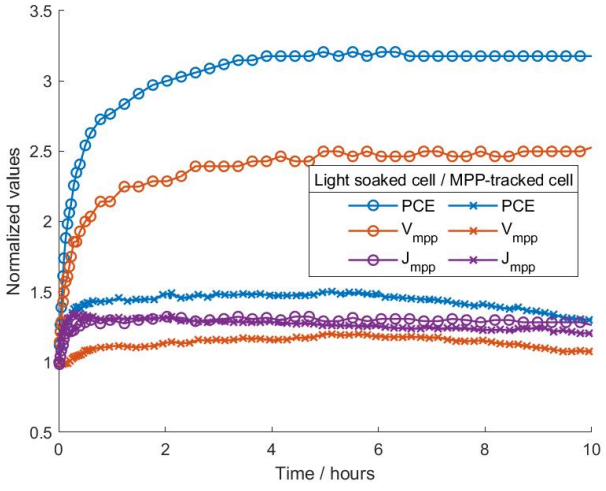

Figure 6.29: Comparison between MPP-tracking and light soaking in an inert atmosphere for cells with PEDOT:PSS as HTL. The cells' efficiencies were normalised to their respective initial values.

6.8 MPP-tracking for a cell with NiO_x

The MPP-tracking procedure for cells with NiO_x was identical to that of cells with PEDOT:PSS. Figure 6.30-6.31 show the results, plotted on a linear and a logarithmic time scale. From the linear plot, it can be clearly seen that the efficiency undergoes a fast initial decrease within the first 10 hours that is then followed by a more stabilised region. In contrast to the cell with PEDOT:PSS (see section 6.7), no initial increase in V_{mpp} can be observed, which was to be expected based on the results of the light soaking experiments where cells with NiO_x exhibited a very stable voltage. During MPP-tracking, the current J_{mpp} sees a steady increase throughout the first 10 hours but start to drop afterwards.

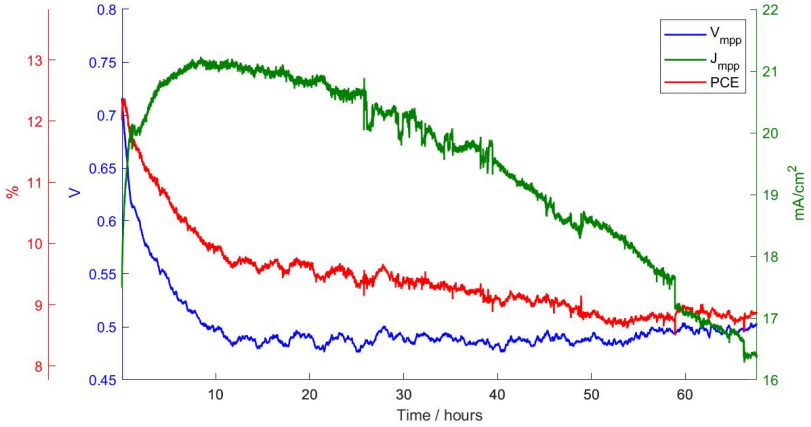

Figure 6.30: MPP-tracking of a cell with NiO_x as HTL in nitrogen atmosphere for 67 hours. Light source: Dedolight.

Figure 6.32 displays JV-curves measured directly before and after the MPP-tracking process, as well as after a recovery period of 1 hour in the dark, for the MPP-tracked cell (6.32a) and a reference cell (6.32b) that was located on the same substrate and kept at open circuit throughout the stability measurement. For the MPP-tracked cell, a change in the shape of the JV-curve that reduces the V_{oc} can be noticed after MPP-tracking, similar to the shift observed in the cell with PEDOT:PSS. Such a shift is, however, not present in the light-soaked reference cell. The forward scans measured immediately after the illumination period are not smooth. The scans were started at a slight reverse bias of -20 mV. Apparently, the light-soaked cells respond strongly to reverse biasing. Moreover, it is interesting that the cells do not show a relaxation behaviour during the dark recovery period but seem to deteriorate further. One possible explanation might be that the initial light-induced increase in current that was observed upon MPP-tracking is reversible and lost again once the cells are stored in the dark. A similar behaviour has been observed by Saliba et al. [99] who referred to the effect as "reversible bonus" (see section 1.4.3).

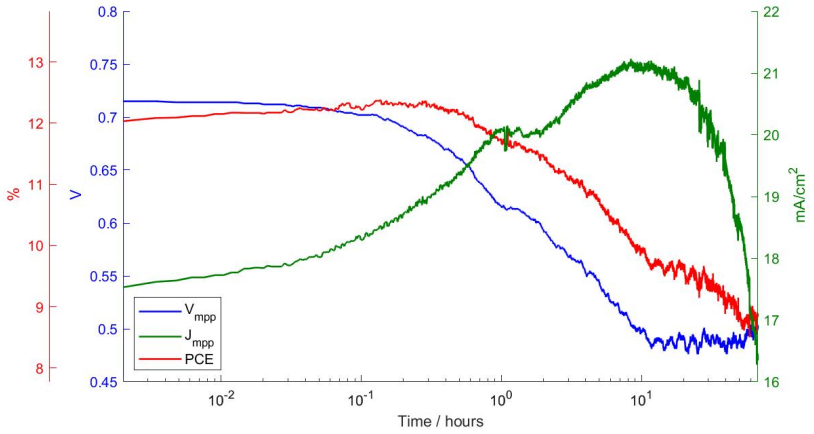

Figure 6.31: MPP-tracking of a cell with NiO_x as HTL in nitrogen atmosphere for 67 hours. Time is displayed in a logarithmic scale to emphasise the rapid, initial changes. Light source: Dedolight.

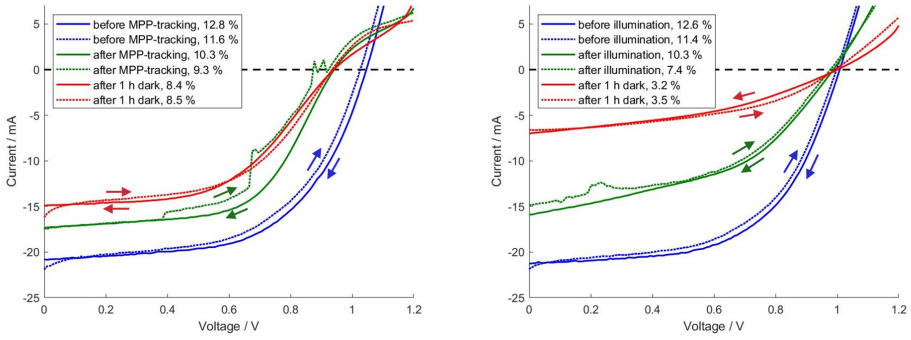

(a) MPP-tracked cell

(b) reference cell

Figure 6.32: JV-curves of cells with NiO_x as HTL measured before and after MPP-tracking for 67 hours, as well as after 1 hour recovery in the dark. Reference cell was illuminated while being kept at V_{oc}. Scan direction: reverse (solid line), forward (dotted line). Scan rate: 100 mV/s. Light source: Dedolight.

6.8.1 EQE-measurements

The EQE measurements performed before and after MPP-tracking (Fig. 6.33) show an overall decrease of the quantum efficiency that is in agreement with the drop in the directly measured J_{sc} (see table 6.6). However, in contrast to the cells with PEDOT:PSS, no significant change in the shape of the spectra is noticeable.

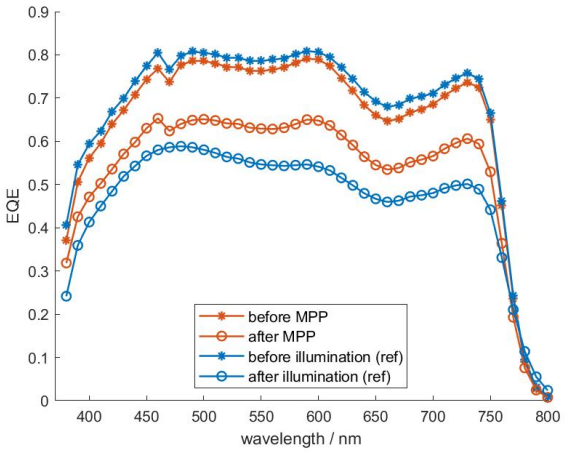

Figure 6.33: Effect of MPP-tracking (67 hours) in nitrogen atmosphere on EQE of a cell with NiO_x as HTL. The reference cell (ref) was illuminated while being kept at V_{oc}.

Table 6.6: Comparison between directly measured J_{sc} and the J_{sc} derived from the EQE spectrum for a MPP-tracked cell with NiO_x as HTL.

	J_{sc} direct / mA/cm^2	J_{sc} EQE / mA/cm^2	J_{sc} direct : J_{sc} EQE
before MPP-tracking	19.3	17.1	1.13
after MPP-tracking	17.1	14.2	1.21
before MPP-tracking (ref)	20.7	17.5	1.18
after MPP-tracking (ref)	15.5	12.3	1.26

6.8.2 Structural changes (XRD)

Similar to the other stability experiments performed in inert atmosphere, no changes were observable in the XRD pattern that were measured before and after MPP-tracking. This indicates that, in this case, too, the bulk crystal structure remains unchanged.

6.8.3 Comparison to light soaking results

Comparing the light soaking results to the first 10 hours of MPP-tracking (Fig. 6.34) for cells with NiO_x shows that the behaviour is quite different depending on whether the cell is kept at open circuit or at its maximum power point.

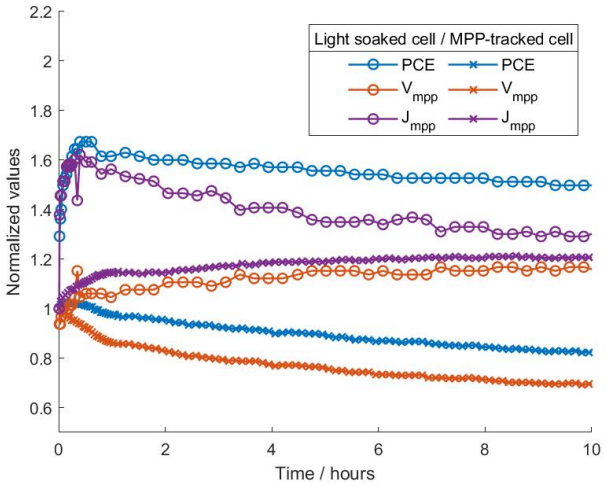

Figure 6.34: Comparison of MPP-tracking and light soaking in inert atmosphere for cells with NiO_x as HTL. The cells' efficiencies were normalised to their respective initial values.

6.9 Impact of hole transport layer on operational stability

The results in section 6.6 show quite clearly that the operational stability of perovskite solar cells strongly depends on the hole transport layer. Within the examined time periods, PEDOT:PSS appeared to introduce a strong initial increase in efficiency, probably due to its strong light soaking behaviour, that is then followed by a rather rapid degradation. NiO_x, on the other hand, shows a fast initial decrease but stabilises afterwards. These results seem to indicate that, in the long run, cells with NiO_x can be expected to be more stable and retain a larger part of their initial efficiency. To illustrate the differences in the stability behaviour of cells with PEDOT:PSS and NiO_x, Figure 6.35 provides a direct comparison of the evolution of the normalised solar cell parameters.

In order to quantify the operational stability of the MPP-tracked cells, different figures-of-merit were calculated according to the procedures discussed in section 1.4.2 and can be found in Table 6.7. T_{80} represents the time after which the efficiency has dropped below 80 % of its initial value. For T_{s80}, instead of the initial efficiency, the maximum efficiency reached after the initial improvement of the cell is used as a reference. For T_{s90}, the degradation curve after the initial burn-in time was extrapolated back (see Fig. 6.36) and the thus-obtained value at time t = 0 used as a reference.

The resulting values quite clearly show that for perovskite solar cells the quantification of their stability is all but straightforward. Depending on the calculation method, the results can lead to quite different conclusions. It is therefore crucial to specify how such figures-of-merit were obtained and how the actual stability curves looked like.

Furthermore, one must not forget that the figures presented in this thesis are based on a singular measurement (only 1 cell per hole transport layer was subjected to long-term MPP-

tracking). In order to set the results on solid ground and confirm the stability behaviours observed within this thesis' work, measurements have to be performed on several equivalent cells.

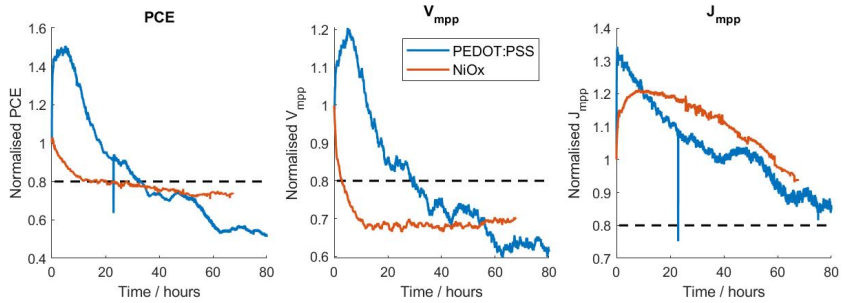

Figure 6.35: Comparison of MPP-tracking behaviour in inert atmosphere for cells with different HTLs. Values are normalised to their respective initial values.

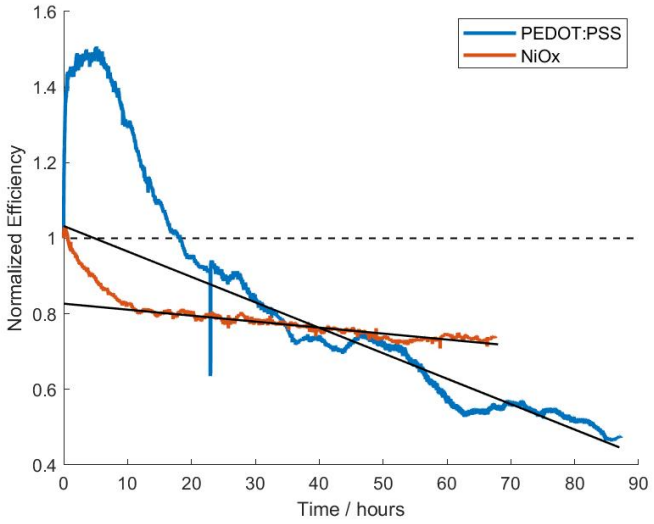

Figure 6.36: Comparison of MPP-tracking behaviour in inert atmosphere for cells with different HTLs. Values are normalised to their respective initial values. Extrapolated curves are displayed in black.

Table 6.7: Stability of MPP-tracked cells with different HTLs. T_80: time after which the cell efficiency dropped to 80 % of its initial value. T_{s80}: stabilised T_{80}-value with respect to the maximum PCE. T_{s90}: stabilised T_{90}-value with respect to back-extrapolated PCE (see sec. 1.4.2).

HTL	T_{80} / h	T_{s80} / h	T_{s90} / h	$PCE_{initial}$ / %	PCE_{max} / %
PEDOT:PSS	32.9	11.9	22.1	4.6	6.9
NiO_x	19.9	9.9	54.6	12.0	12.4

6.10 Impact of hole transport layer on charge recombination

Table 6.8 shows that the ratio between the directly measured J_{sc} and the J_{sc} that was calculated from EQE depends on the choice of hole transport layer. For cells with PEDOT:PSS, the ratio is 1.6 on average, while it is only 1.1 for cells with NiO_x.

As already discussed in section 6.3.1, the discrepancy between the two J_{sc} values can stem from the difference in light intensity and the fact that during EQE measurements, only part of the cell area is illuminated. As a result, recombination mechanisms and microshunts have a larger impact on EQE measurements as compared to the JV-setup. The different ratios for PEDOT:PSS and NiO_x might indicate that recombination is less dominant in cells with NiO_x. Possible reasons might be a higher interface quality between NiO_x and the perovskite that exhibits a lower defect density.

Table 6.8: Average ratio between directly measured J_{sc} and the J_{sc} derived from EQE-measurements for different HTLs.

HTL	J_{sc} direct : J_{sc} EQE
PEDOT:PSS	1.6 ± 0.2
NiO_x	1.1 ± 0.1

6.11 Conclusion

To sum up, it was demonstrated that the stability of perovskite solar cells towards illumination is decisively influenced by the choice of hole transport layer. For cells with the organic PEDOT:PSS, a strong metastable light soaking behaviour could be observed that showed primarily in an increase in V_{oc}. Over one light/dark soaking cycle, the change in V_{oc} was almost fully reversible except for a small irreversible part. Cells with NiO_x, on the other hand, exhibited a much smaller response to illumination that mainly showed in the J_{sc} and the FF. In contrast to cells with PEDOT:PSS, the V_{oc} remained very stable. For both hole transport layers, the light-induced change in solar cell parameter was observed to be to a large extent reversible, except for the FF that permanently increased upon illumination. To investigate whether the irreversible parts of the light-induced changes correspond to a "burn-in" of the cell, that is an initial change that then stabilises, it would be necessary to perform several successive cycles of light/dark soaking.

Based on the observations described above, it can be concluded that the reversible light soaking behaviour has its origin mainly in the hole transport layer, or in the interface formed between the hole transport layer and the perovskite. However, the experiments performed for this thesis do not allow any conclusions on the mechanisms that underlie the light soaking behaviour, though experiences with similar effects in chalcogenide photovoltaics suggest that it is defect-driven. In order to verify this assumption, more detailed experiments would be necessary.

When light/dark soaking was performed for unencapsulated cells in ambient air, devices both with pure PEDOT:PSS and NiO_x degraded completely within several hours. The device with DMSO-doped PEDOT:PSS retained a very small percentage of its efficiency over one light/dark soaking effect but to determine whether there is really a significant difference in stability between the different cell architectures the experiment has to be repeated for several equivalent devices. The cells degraded by light/dark soaking in ambient air showed structural changes that could not be observed for light/dark soaking in inert atmosphere. Regardless of the type of hole transport layer, the same additional peaks emerged in the XRD. Unfortunately, the peaks could not be assigned to a known crystal structure but a list of the peaks can be found in Table 6.2 and 6.4.

During MPP-tracking (and long term illumination) in inert atmosphere, degradation was observable for cells with both PEDOT:PSS and NiO_x. Again, the behaviour was quite different, and in the long run, NiO_x appeared to be more stable. Despite the degradation in cell efficiency, no structural changes were noticeable in the XRD. The EQE spectra showed changes only for cells with PEDOT:PSS. The relaxation behaviour and reversibility of the light-induced degradation was insufficiently investigated. This would be an interesting objective for future experiments.

Chapter 7

Conclusion and Outlook

In the following, the key conclusions that can be drawn based on the results discussed in chapter 3-6 are summarised and suggestions for future experiments are provided.
An important remark has to be made right at the beginning. For all results presented in this thesis, the restricted time did not allow for a proper statistical verification of the data. In order to verify the results and set them onto solid ground, all the measurements have to be repeated for a large enough number of equivalent cells. This is especially important as the fabrication process of perovskite solar cells used within this thesis is poorly controllable (due to spin coating, anti-solvent dripping, crystallisation etc.) and the cells were found to be sensitive to almost all process parameters. Even though the controllable parameters were kept unchanged, resulting cell efficiencies exhibited a large variance (see section 3.6.1).

To sum up the main achievements of this thesis, the successful synthesis of perovskite solar cells with inorganic Cs-doped NiO_x as an alternative to organic hole transport layers could be demonstrated. The operational stability and the metastable response to light soaking was investigated and compared for both cell architectures. The results showed that NiO_x is the better choice, both in terms of long-term stability and metastable behaviours. Cells with NiO_x responded far less strongly to illumination and showed a much more stable V_{oc}.

7.1 Synthesis

Regarding the synthesis process in more detail, this thesis could, for one thing, confirm that the addition of a small amount of DMSO (5-10 %) to PEDOT:PSS significantly enhances the current output of the resulting solar cells. This is in agreement with previous results [111, 112]. However, issues were faced during the deposition process. For some substrates, inhomogeneities and holes appeared in the film upon spin-coating, a problem that has never occurred for pure PEDOT:PSS.
As an alternative to organic PEDOT:PSS, cells with an inorganic Cs-doped NiO_x hole transport layer could be successfully synthesised based on a sol-gel process. Compared to cells with PEDOT:PSS, they achieved higher PCE values which is mainly due to their higher V_{oc} of roughly 1 V (cells with PEDOT:PSS exhibited a $V_{oc} \approx 0.85$ V).
It was further shown that the introduction of ZnO as a second electron transport layer is

beneficial to the device performance.
For time reasons, no optimisation of layer thicknesses could be performed. This would certainly be an important step on the way to achieving device efficiencies that are closer to the current record of 25.2 %.

EBIC images taken of cells with both PEDOT:PSS and NiO_x revealed a spatially inhomogeneous current output that greatly limits the total efficiency of the cells. The shapes of the inhomogeneities indicate that they might be a results of solution processing, i.e. spin-coating and anti-solvent dripping but further experiments are necessary to better understand the cause and formation of these inhomogeneities.

7.2 Stability of perovskite solar cells

In this thesis, the high sensitivity of perovskite solar cells to external factors such as moisture, oxygen and light could be demonstrated. Unencapsulated cells with PEDOT:PSS as hole transport layer were observed to fully degrade within minutes in damp heat conditions (85 °C, 85 % RH), within hours upon light soaking in ambient air and within days when stored in the dark in dry air. In terms of stability, no significant difference could be observed between pure and DMSO-doped PEDOT:PSS. Cells with NiO_x were only subjected to light soaking in ambient air which resulted in degradation times similar to those of cells with PEDOT:PSS.
In ambient air, degradation of the silver electrode posed a serious problem. Upon light soaking, etching of the electrodes through the whole solar cell was observed, especially for the cell that was repeatedly measured. Storage in dry air resulted in a darkening of the electrode of the cell whose performance was tracked by regular JV-scans. Apparently, the degradation of the silver electrode is accelerated by electric fields/current flow through the device. Replacement of silver by a more stable electrode material might improve the overall stability of the cells.

Regarding the operational stability that was examined by MPP-tracking in inert atmosphere, cells with PEDOT:PSS and NiO_x as hole transport layer both showed significant degradation over the course of about 70 hours though different in shape and magnitude. For the cell with PEDOT:PSS, a strong initial increase in efficiency (due to light soaking effect) was followed by a steady, rather steep degradation curve. The cell with NiO_x, however, only showed a small initial increase that was quickly dominated by degradation after 1 hour. However, the cell was observed to stabilise after a steep initial decrease in PCE. Therefore, in the long run, the use of NiO_x proved to result in a more stable cell architecture as compared to PEDOT:PSS.
Still, some degree of degradation was observable for both types of hole transport layers and further experiments are necessary to gain a better understanding of the involved mechanisms and to eventually be able to eliminate all causes for degradation. Furthermore, experimental data on the (ir)reversibility of the changes induced by MPP-tracking is still missing.

7.2.1 Metastable light soaking behaviour and impact of HTL

In the experimental work, special focus was laid on the cells' metastable response to light soaking. Experiments performed in inert atmosphere demonstrated that devices with PEDOT:PSS as hole transport layer exhibit a huge metastable light soaking effect. Their V_{oc} strongly increases upon illumination, a change that is almost fully reversible when the cells are stored in the dark for several hours. In contrast, cells with NiO_x showed a much smaller and different response to illumination, in particular their V_{oc} was found to be very stable. This indicates that the origin of the strong light soaking behaviour of cells with PEDOT:PSS lies in the hole transport layer (or the interface formed by the transport layer and the perovskite). Further experiments are necessary to investigate the mechanisms responsible for the metastable behaviour but based on experiences with similar effects in chalcogenide photovoltaics, it can be expected that the behaviour is mainly defect-driven. However, due to the ionomeric nature of PEDOT:PSS, polarisation effects might also play a role.

7.2.2 Structural changes

XRD measurements were frequently performed within this thesis to check for changes in the bulk crystal structure. Such changes could only be observed when the cells were exposed to ambient air and some degree of humidity (e.g. light soaking in ambient air and damp heat testing). All experiments performed in inert atmosphere (light soaking, MPP-tracking, dark storage) left the bulk structure unaltered, thus demonstrating that the bulk perovskite is stable in the absence of oxygen and humidity. Therefore, any permanent degradation or changes that could be observed during measurements in inert atmosphere can only have occurred at the interfaces or in volumes inside the bulk (e.g. grain boundaries) that are small enough not to show up in XRD.
Even if changes could be observed in XRD (see below), they did not correspond to the formation of PbI_2 that usually accompanies the complete, irreversible decomposition of the perovskite. This is another indication for the high structural stability of the triple-cation perovskite.

Table 7.1 provides an overview of the structural changes that have been observed. It comprises a list of the XRD peaks that appeared after different stability tests. Upon light soaking in ambient air, the same additional peaks emerged in the XRD patten for both HTLs, NiO_x and PEDOT:PSS. However, the peaks could not be assigned to any known crystal structure so far. Damp heat conditions were observed to lead to the formation of a hydrate structure for a cell with PEDOT:PSS. Upon dark storage in dry air, only one small additional peak appeared at 11.3 ° for cells both with pure DMSO-doped PEDOT:PSS.

Table 7.1: Summary of XRD peaks appearing in unencapsulated devices after applying different external stressors. Peaks that emerge after both light soaking and damp heat testing are highlighted in grey.

Damp heat testing		Light soaking in ambient air		Dark storage in dry air	
2θ / °	$\Delta 2\theta$ / °	2θ / °	$\Delta 2\theta$ / °	2θ / °	$\Delta 2\theta$ / °
-	-	-	-	11.3	0.1
11.9	0.1	-	-	-	-
20.5	0.1	-	-	-	-
-	-	22.4	0.3	-	-
23.8	0.1	23.8	0.2	-	-
25.7	0.1	-	-	-	-
26.6	0.2	26.7	0.1	-	-
32.6	0.2	32.7	0.2	-	-
33.5	0.1	-	-	-	-
35.8	0.2	-	-	-	-
-	-	39.2	0.4	-	-
-	-	46.2	0.5	-	-

Appendix A

Used measuring instruments

Table A.1: List of measuring instruments and equipment used for this thesis.

Instrument	Manufacturer	Comment
2400 SourceMeter	Keithley	IV characterisation and EQE measurements, Graz
2600 Series SourceMeter	Keithley	EBIC measurements
2651A High Power System SourceMeter	LXI	IV characterisation, Vienna
6490LV SEM	Jeol	EBIC measurements
818-UV low-power UV-enhanced silicon photodetector	Newport	EQE measurements
AB204-S Analytical Balance	Mettler Toledo	Weighing out chemicals (glovebox)
Adventurer Analytical Balance	OHAUS	Weighing out NiO_x precursor
ADwin-Pro II Data Aquisition System	ADwin	EBIC measurements
ARL EQUINOX 100 X-Ray Diffractometer	ThermoScientific	XRD, Vienna
Climate Chamber TCZ 7016 S(m) -1,2K	$TIRA_{UWS}$	-
Controller P 330 Furnace	Nabertherm	Annealing of NiO_x films
DektakXT Stylus Profilometer	Bruker	Profilometry
DLH400D HMI Daylight Spotlight	dedolight	Light source, Graz
Empyrean x-ray diffractometer	Malvern Panalytical	XRR
Femto Plasma System	diener electronic	O_2-plasma treatment of ITO
Lamp Housing for 75W Xenon Lamp	AMKO	EQE measurements
LPS20-U Universal Lamp Power Supply	AMKO	EQE measurements
MCS 66 Heating Plate	CAT	Annealing of perovskite layers
MiniFlex x-ray diffractometer	Rigaku	XRD, Graz
MR 3001 K Hot plate	Heidolph	Stirring of NiO_x-precursor
MulLTImode4-AT Grating Monochromator	AMKO	EQE measurements
Oberflaechen TEMP Heizplatte	IKAMAG RCT	Stirring of precursors
SQM-160 Rate/Thickness Monitor	Inficon	Thickness monitoring during PVD
SR570 Low noise current preamplifier	SRS Stanford Research Systems	EBIC measurements
SUPRA 40 FE-SEM	ZEISS	SEM, Vienna
$Trisol^{TM}$ Class AAA Standard Solar Simulator TSS-208	OAI	Light source, Vienna
Ultrasonic Cleaner	VWR	-
WS-650MZ-23NPPB Spin Coater	Laurell	-

Bibliography

[1] Renewables 2019: Analysis and forecasts to 2024, https://www.iea.org/reports/renewables-2019, accessed 13.04.2020 (2019).

[2] A. McEvoy, L. Castañer, T. Markvart (Eds.), Solar Cells, 2nd Edition, Elsevier, 2013.

[3] A. P. Kirk, Solar photovoltaic cells: Photons to electricity, Academic Press an inprint of Elsevier, London and San Diego, 2015.

[4] Dino Green, Advantages and disadvantages of Solar Photovoltaic: Quick Pros and Cons of Solar PV, http://www.renewablegreenenergypower.com/advantages-and-disadvantages-of-solar-photovoltaic-quick-pros-and-cons-of-solar-pv/, accessed 21.03.2020 (2012).

[5] Market share of global solar photovoltaics from 2011 to 2015, by technology, https://www.statista.com/statistics/492724/solar-pv-global-market-share-by-cell-technology/, accessed 16.03.2020 (2018).

[6] What Are the Most Efficient Solar Panels on the Market?, https://greentumble.com/most-efficient-solar-panels-on-the-market/, accessed 16.03.2020 (2019).

[7] W. Shockley, H. J. Queisser, Detailed Balance Limit of Efficiency of p–n Junction Solar Cells, Journal of Applied Physics 32 (3) (1961) 510–519. doi:10.1063/1.1736034.

[8] Joseph Mathurin Kuitche, A Statistical Approach to Solar Photovoltaic Module Lifetime Prediction, Dissertation, Arizona State University (December 2014).
URL https://repository.asu.edu/attachments/143310/content/Kuitche_asu_0010E_14456.pdf

[9] M. Woodhouse, B. Smith, A. Ramdas, R. Margolis, Crystalline Silicon Photovoltaic Module Manufacturing Costs and Sustainable Pricing: 1H 2018 Benchmark and Cost Reduction Road Map: Technical Report, https://www.nrel.gov/docs/fy19osti/72134.pdf, accessed 13.04.2020 (February 2020).

[10] T. Ibn-Mohammed, S. Koh, I. M. Reaney, A. Acquaye, G. Schileo, K. B. Mustapha, R. Greenough, Perovskite solar cells: An integrated hybrid lifecycle assessment and review in comparison with other photovoltaic technologies, Renewable and Sustainable Energy Reviews 80 (2017) 1321–1344. doi:10.1016/j.rser.2017.05.095.

[11] A. Kojima, K. Teshima, Y. Shirai, T. Miyasaka, Organometal halide perovskites as visible-light sensitizers for photovoltaic cells, Journal of the American Chemical Society 131 (17) (2009) 6050–6051. doi:10.1021/ja809598r.

[12] A. K. Jena, A. Kulkarni, T. Miyasaka, Halide Perovskite Photovoltaics: Background, Status, and Future Prospects, Chemical reviews 119 (5) (2019) 3036–3103. doi:10.1021/acs.chemrev.8b00539.

[13] NREL - U.S. National Renewable Energy Laboratory, Best Research-Cell Efficiencies, https://www.nrel.gov/pv/assets/pdfs/best-research-cell-efficiencies.20200311.pdf, accessed 16.03.2020.

[14] NREL - U.S. National Renewable Enery Laboratory, Champion Photovoltaic Module Efficiency Chart, https://www.nrel.gov/pv/assets/pdfs/champion-module-efficiencies.20191104.pdf, accessed 16.03.2020.

[15] D. A. Egger, A. Bera, D. Cahen, G. Hodes, T. Kirchartz, L. Kronik, R. Lovrincic, A. M. Rappe, D. R. Reichman, O. Yaffe, What Remains Unexplained about the Properties of Halide Perovskites?, Advanced materials (Deerfield Beach, Fla.) 30 (20) (2018) e1800691. doi:10.1002/adma.201800691.

[16] M. Saliba, T. Matsui, J.-Y. Seo, Cesium-containing triple cation perovskite solar cells: improved stability, reproducibility and high efficiency, Energy & Environmental Sience 9 (2016) 1989–1997. doi:10.1039/c5ee03874j.

[17] A. M. A. Leguy, Y. Hu, M. Campoy-Quiles, M. I. Alonso, O. J. Weber, P. Azarhoosh, M. van Schilfgaarde, M. T. Weller, T. Bein, J. Nelson, P. Docampo, P. R. F. Barnes, Reversible Hydration of CH3NH3PbI3 in Films, Single Crystals, and Solar Cells, Chemistry of Materials 27 (9) (2015) 3397–3407. doi:10.1021/acs.chemmater.5b00660.

[18] H. Fu, Review of lead-free halide perovskites as light-absorbers for photovoltaic applications: From materials to solar cells, Solar Energy Materials and Solar Cells 193 (2019) 107–132. doi:10.1016/j.solmat.2018.12.038.

[19] N. K. Noel, S. D. Stranks, A. Abate, C. Wehrenfennig, S. Guarnera, A.-A. Haghighirad, A. Sadhanala, G. E. Eperon, S. K. Pathak, M. B. Johnston, A. Petrozza, L. M. Herz, H. J. Snaith, Lead-free organic–inorganic tin halide perovskites for photovoltaic applications, Energy & Environmental Science 7 (9) (2014) 3061–3068. doi:10.1039/C4EE01076K.

[20] World Health Oranization, Lead poisoning and health, www.who.int/en/news-room/fact-sheets/detail/lead-poisoning-and-health, accessed 09.10.2019 (August 2018).

[21] International Agency for Research on Cancer, Inorganic and Organic Lead Compounds: Summary of Data Reported and Evaluation, IARC Monographs on the Evaluation of Carcinogenic Risks to Humans 87.

[22] Joint FAO/WHO Expert Comittee on Food Additives: Seventy-third meeting, www.who.int/foodsafety/publications/chem/summary73.pdf, accessed 13.04.2020 (June 2010).

[23] The European Parliament and the Council of the European Union, Directive 2011/65/EU of the European Parliament and of the Council of 8 June 2011: on the restriction of the use of certain hazardous substances in electrical and electronic equipment: Text with EEA relevance, Official Journal of the European Union L 174 (2011) 88–110.

[24] A. Babayigit, H.-G. Boyen, B. Conings, Environment versus sustainable energy: The case of lead halide perovskite-based solar cells, MRS Energy & Sustainability 5 (2018) 1293. doi:10.1557/mre.2017.17.

[25] M. Saurat, M. Ritthoff, Photovoltaics and the RoHS Directive: Position Paper, Wuppertal Institute, http://www.dartmouth.edu/ cushman/courses/engs171/SauratRittoff-Photovoltaics_and_RoHS-2010.pdf, accessed 13.04.2020 (May 2010).

[26] B. Hailegnaw, S. Kirmayer, E. Edri, G. Hodes, D. Cahen, Rain on Methylammonium Lead Iodide Based Perovskites: Possible Environmental Effects of Perovskite Solar Cells, The journal of physical chemistry letters 6 (9) (2015) 1543–1547. doi:10.1021/acs.jpclett.5b00504.

[27] A. R. Chakhmouradian, P. M. Woodward, Celebrating 175 years of perovskite research: a tribute to Roger H. Mitchell, Physics and Chemistry of Minerals 41 (6) (2014) 387–391. doi:10.1007/s00269-014-0678-9.

[28] X. Zhao, M. Wang, Organic hole-transporting materials for efficient perovskite solar cells, Materials Today Energy 7 (2018) 208–220. doi:10.1016/j.mtener.2017.09.011.

[29] T. Leijtens, K. Bush, R. Cheacharoen, R. Beal, A. Bowring, M. D. McGehee, Towards enabling stable lead halide perovskite solar cells; interplay between structural, environmental, and thermal stability, Journal of Materials Chemistry A 5 (23) (2017) 11483–11500. doi:10.1039/c7ta00434f.

[30] S. P. Dunfield, L. Bliss, F. Zhang, J. M. Luther, K. Zhu, M. F. A. M. Hest, M. O. Reese, J. J. Berry, From Defects to Degradation: A Mechanistic Understanding of Degradation in Perovskite Solar Cell Devices and Modules, Advanced Energy Materials 7 (2020) 1904054. doi:10.1002/aenm.201904054.

[31] Perovskite Structure and Derivatives, http://www.princeton.edu/ cava-lab/tutorials/public/structures/perovskites.html, accessed 17.03.2020.

[32] A. R. B. Mohd Yusoff, P. Gao, M. K. Nazeeruddin, Recent progress in organohalide lead perovskites for photovoltaic and optoelectronic applications, Coordination Chemistry Reviews 373 (2018) 258–294. doi:10.1016/j.ccr.2017.10.021.

[33] Z. Yi, N. H. Ladi, X. Shai, H. Li, Y. Shen, M. Wang, Will organic–inorganic hybrid halide lead perovskites be eliminated from optoelectronic applications?, Nanoscale Advances 1 (4) (2019) 1276–1289. doi:10.1039/C8NA00416A.

[34] G. Kieslich, S. Sun, A. K. Cheetham, Solid-state principles applied to organic–inorganic perovskites: new tricks for an old dog, Chem. Sci. 5 (12) (2014) 4712–4715. doi:10.1039/C4SC02211D.

[35] F. Brivio, K. T. Butler, A. Walsh, M. van Schilfgaarde, Relativistic quasiparticle self-consistent electronic structure of hybrid halide perovskite photovoltaic absorbers, Physical Review B 89 (15). doi:10.1103/PhysRevB.89.155204.

[36] T. Leijtens, G. E. Eperon, N. K. Noel, S. N. Habisreutinger, A. Petrozza, H. J. Snaith, Stability of Metal Halide Perovskite Solar Cells, Advanced Energy Materials 5 (20) (2015) 1500963. doi:10.1002/aenm.201500963.

[37] M. Liu, M. B. Johnston, H. J. Snaith, Efficient planar heterojunction perovskite solar cells by vapour deposition, Nature 501 (2013) 395 EP –. doi:10.1038/nature12509.

[38] C. C. Boyd, R. Cheacharoen, T. Leijtens, M. D. McGehee, Understanding Degradation Mechanisms and Improving Stability of Perovskite Photovoltaics, Chemical reviews 119 (5) (2019) 3418–3451. doi:10.1021/acs.chemrev.8b00336.

[39] M. Grundmann (Ed.), The Physics of Semiconductors, Graduate Texts in Physics, Springer International Publishing, Cham, 2016. doi:10.1007/978-3-319-23880-7.

[40] H. Ishii, K. Sugiyama, E. Ito, K. Seki, Energy Level Alignment and Interfacial Electronic Structures at Organic/Metal and Organic/Organic Interfaces, Advanced Materials 11 (8) (1999) 605–625.

[41] A. Köhler, H. Bässler, Electronic processes in organic semiconductors: An introduction / Anne Köhler and Heinz Bässler, Wiley-VCH, Weinheim, 2015.

[42] H. Ishii, N. Hayashi, E. Ito, Y. Washizu, K. Sugi, Y. Kimura, M. Niwano, Y. Ouchi, K. Seki, Kelvin probe study of band bending at organic semiconductor/metal interfaces: examination of Fermi level alignment, physica status solidi (a) 201 (6) (2004) 1075–1094. doi:10.1002/pssa.200404346.

[43] G. Grosso, G. P. Parravicini, Transport in Intrinsic and Homogeneously Doped Semiconductors, in: G. Grosso, G. Pastori Parravicini (Eds.), Solid state physics, Academic Press, Oxford, 2014, p. 590. doi:10.1016/B978-0-12-385030-0.00013-X.

[44] S. Holliday, J. E. Donaghey, I. McCulloch, Advances in Charge Carrier Mobilities of Semiconducting Polymers Used in Organic Transistors, Chemistry of Materials 26 (1) (2014) 647–663. doi:10.1021/cm402421p.

[45] T. Minami, Transparent conducting oxide semiconductors for transparent electrodes, physica status solidi (a) 20 (4) (2005) S35–S44. doi:10.1088/0268-1242/20/4/004.

[46] A. Janotti, C. G. van de Walle, Native point defects in ZnO, Physical Review B 76 (16) (2007) 869. doi:10.1103/PhysRevB.76.165202.

[47] C.-C. Lien, C.-Y. Wu, Z.-Q. Li, J.-J. Lin, Electrical conduction processes in ZnO in a wide temperature range 20–500 K, Journal of Applied Physics 110 (6) (2011) 063706. doi:10.1063/1.3638120.

[48] M. L. Grilli, F. Menchini, T. Dikonimos, P. Nunziante, L. Pilloni, M. Yilmaz, A. Piegari, A. Mittiga, Effect of growth parameters on the properties of RF-sputtered highly conductive and transparent p-type NiO x films, Semiconductor Science and Technology 31 (5) (2016) 055016. doi:10.1088/0268-1242/31/5/055016.

[49] R. Huebener, Leiter, Halbleiter, Supraleiter: Eine kompakte Einführung in Geschichte, Entwicklung und Theorie der Festkörperphysik / Rudolf Huebener, second edition Edition, Springer Spektrum, Berlin, Heidelberg, 2016.

[50] E. Edri, S. Kirmayer, S. Mukhopadhyay, K. Gartsman, G. Hodes, D. Cahen, Elucidating the charge carrier separation and working mechanism of CH3NH3PbI(3-x)Cl(x) perovskite solar cells, Nature Communications 5 (2014) 3461. doi:10.1038/ncomms4461.

[51] H.-W. Li, Z. Guan, Y. Cheng, T. Lui, Q. Yang, C.-S. Lee, S. Chen, S.-W. Tsang, On the Study of Exciton Binding Energy with Direct Charge Generation in Photovoltaic Polymers, Advanced Electronic Materials 2 (11) (2016) 1600200. doi:10.1002/aelm.201600200.

[52] V. D'Innocenzo, G. Grancini, M. J. P. Alcocer, A. R. S. Kandada, S. D. Stranks, M. M. Lee, G. Lanzani, H. J. Snaith, A. Petrozza, Excitons versus free charges in organo-lead tri-halide perovskites, Nature Communications 5 (2014) 3586. doi:10.1038/ncomms4586.

[53] M. Hirasawa, T. Ishihara, T. Goto, K. Uchida, N. Miura, Magnetoabsorption of the lowest exciton in perovskite-type compound (CH3NH3)PbI3, Physica B: Condensed Matter 201 (1994) 427–430. doi:10.1016/0921-4526(94)91130-4.

[54] L. Bertoluzzi, C. C. Boyd, N. Rolston, J. Xu, R. Prasanna, B. C. O'Regan, M. D. McGehee, Mobile Ion Concentration Measurement and Open-Access Band Diagram Simulation Platform for Halide Perovskite Solar Cells, Joule 4 (1) (2020) 109–127. doi:10.1016/j.joule.2019.10.003.

[55] S. N. Habisreutinger, N. K. Noel, H. J. Snaith, Hysteresis Index: A Figure without Merit for Quantifying Hysteresis in Perovskite Solar Cells, ACS Energy Letters 3 (10) (2018) 2472–2476. doi:10.1021/acsenergylett.8b01627.

[56] C. Eames, J. M. Frost, P. R. F. Barnes, B. C. O'Regan, A. Walsh, M. S. Islam, Ionic transport in hybrid lead iodide perovskite solar cells, Nature Communications 6 (2015) 7497. doi:10.1038/ncomms8497.

[57] P. Lopez-Varo, J. A. Jiménez-Tejada, M. García-Rosell, S. Ravishankar, G. Garcia-Belmonte, J. Bisquert, O. Almora, Device Physics of Hybrid Perovskite Solar cells: Theory and Experiment, Advanced Energy Materials 8 (14) (2018) 1702772. doi:10.1002/aenm.201702772.

[58] J. Wei, Y. Zhao, H. Li, G. Li, J. Pan, D. Xu, Q. Zhao, D. Yu, Hysteresis Analysis Based on the Ferroelectric Effect in Hybrid Perovskite Solar Cells, The journal of physical chemistry letters 5 (21) (2014) 3937–3945. doi:10.1021/jz502111u.

[59] E. L. Unger, E. T. Hoke, C. D. Bailie, W. H. Nguyen, A. R. Bowring, T. Heumüller, M. G. Christoforo, M. D. McGehee, Hysteresis and transient behavior in current–voltage measurements of hybrid-perovskite absorber solar cells, Energy & Environmental Science 7 (11) (2014) 3690–3698. doi:10.1039/C4EE02465F.

[60] H. J. Snaith, A. Abate, J. M. Ball, G. E. Eperon, T. Leijtens, N. K. Noel, S. D. Stranks, J. T.-W. Wang, K. Wojciechowski, W. Zhang, Anomalous Hysteresis in Perovskite Solar Cells, The journal of physical chemistry letters 5 (9) (2014) 1511–1515. doi:10.1021/jz500113x.

[61] Q. Wang, N. Phung, D. Di Girolamo, P. Vivo, A. Abate, Enhancement in lifespan of halide perovskite solar cells, Energy & Environmental Science 12 (3) (2019) 865–886. doi:10.1039/C8EE02852D.

[62] T. A. Berhe, W.-N. Su, C.-H. Chen, C.-J. Pan, J.-H. Cheng, H.-M. Chen, M.-C. Tsai, L.-Y. Chen, A. A. Dubale, B.-J. Hwang, Organometal halide perovskite solar cells: degradation and stability, Energy & Environmental Science 9 (2) (2016) 323–356. doi:10.1039/C5EE02733K.

[63] J. Li, Q. Dong, N. Li, L. Wang, Direct Evidence of Ion Diffusion for the Silver-Electrode-Induced Thermal Degradation of Inverted Perovskite Solar Cells, Advanced Energy Materials 7 (14) (2017) 1602922. doi:10.1002/aenm.201602922.

[64] T. Oku, Crystal Structures of CH3NH3PbI3 and Related Perovskite Compounds Used for Solar Cells, in: L. A. Kosyachenko (Ed.), Solar Cells - New Approaches and Reviews, InTech, 2015. doi:10.5772/59284.

[65] B. Conings, J. Drijkoningen, N. Gauquelin, A. Babayigit, J. D'Haen, L. D'Olieslaeger, A. Ethirajan, J. Verbeeck, J. Manca, E. Mosconi, F. de Angelis, H.-G. Boyen, Intrinsic Thermal Instability of Methylammonium Lead Trihalide Perovskite, Advanced Energy Materials 5 (15) (2015) 1500477. doi:10.1002/aenm.201500477.

[66] T. M. Koh, K. Fu, Y. Fang, S. Chen, T. C. Sum, N. Mathews, S. G. Mhaisalkar, P. P. Boix, T. Baikie, Formamidinium-Containing Metal-Halide: An Alternative Material for Near-IR Absorption Perovskite Solar Cells, The Journal of Physical Chemistry C 118 (30) (2014) 16458–16462. doi:10.1021/jp411112k.

[67] N. J. Jeon, J. H. Noh, W. S. Yang, Y. C. Kim, S. Ryu, J. Seo, S. I. Seok, Compositional engineering of perovskite materials for high-performance solar cells, Nature 517 (2015) 476 EP –. doi:10.1038/nature14133.

[68] C. C. Stoumpos, C. D. Malliakas, M. G. Kanatzidis, Semiconducting Tin and Lead Iodide Perovskites with Organic Cations: Phase Transitions, High Mobilities, and Near-Infrared Photoluminescent Properties, Inorganic chemistry 52 (15) (2013) 9019–9038. doi:10.1021/ic401215x.

[69] S. Aharon, A. Dymshits, A. Rotem, L. Etgar, Temperature dependence of hole conductor free formamidinium lead iodide perovskite based solar cells, Journal of Materials Chemistry A 3 (17) (2015) 9171–9178. doi:10.1039/C4TA05149A.

[70] J. H. Noh, S. H. Im, J. H. Heo, T. N. Mandal, S. I. Seok, Chemical management for colorful, efficient, and stable inorganic-organic hybrid nanostructured solar cells, Nano letters 13 (4) (2013) 1764–1769. doi:10.1021/nl400349b.

[71] B. Suarez, V. Gonzalez-Pedro, T. S. Ripolles, R. S. Sanchez, L. Otero, I. Mora-Sero, Recombination Study of Combined Halides (Cl, Br, I) Perovskite Solar Cells, The journal of physical chemistry letters 5 (10) (2014) 1628–1635. doi:10.1021/jz5006797.

[72] S. Colella, E. Mosconi, P. Fedeli, A. Listorti, F. Gazza, F. Orlandi, P. Ferro, T. Besagni, A. Rizzo, G. Calestani, G. Gigli, F. de Angelis, R. Mosca, MAPbI3-xClx Mixed Halide Perovskite for Hybrid Solar Cells: The Role of Chloride as Dopant on the Transport and Structural Properties, Chemistry of Materials 25 (22) (2013) 4613–4618. doi:10.1021/cm402919x.

[73] A. Amat, E. Mosconi, E. Ronca, C. Quarti, P. Umari, M. K. Nazeeruddin, M. Grätzel, F. de Angelis, Cation-induced band-gap tuning in organohalide perovskites: interplay of spin-orbit coupling and octahedra tilting, Nano letters 14 (6) (2014) 3608–3616. doi:10.1021/nl5012992.

[74] P. Roy, N. Kumar Sinha, S. Tiwari, A. Khare, A review on perovskite solar cells: Evolution of architecture, fabrication techniques, commercialization issues and status, Solar Energy 198 (2020) 665–688. doi:10.1016/j.solener.2020.01.080.

[75] N. Aristidou, I. Sanchez-Molina, T. Chotchuangchutchaval, M. Brown, L. Martinez, T. Rath, S. A. Haque, The Role of Oxygen in the Degradation of Methylammonium Lead Trihalide Perovskite Photoactive Layers, Angewandte Chemie (International ed. in English) 54 (28) (2015) 8208–8212. doi:10.1002/anie.201503153.

[76] E. T. Hoke, D. J. Slotcavage, E. R. Dohner, A. R. Bowring, H. I. Karunadasa, M. D. McGehee, Reversible photo-induced trap formation in mixed-halide hybrid perovskites for photovoltaics, Chem. Sci. 6 (1) (2015) 613–617. doi:10.1039/c4sc03141e.

[77] J. A. Christians, P. Schulz, J. S. Tinkham, T. H. Schloemer, S. P. Harvey, B. J. Tremolet de Villers, A. Sellinger, J. J. Berry, J. M. Luther, Tailored interfaces of unencapsulated perovskite solar cells for >1,000 hour operational stability, Nature Energy 3 (1) (2018) 68–74. doi:10.1038/s41560-017-0067-y.

[78] X. Deng, X. Wen, J. Zheng, T. Young, C. F. J. Lau, J. Kim, M. Green, S. Huang, A. Ho-Baillie, Dynamic study of the light soaking effect on perovskite solar cells by in-situ photoluminescence microscopy, Nano Energy 46 (2018) 356–364. doi:10.1016/j.nanoen.2018.02.024.

[79] K. Domanski, B. Roose, T. Matsui, M. Saliba, S.-H. Turren-Cruz, J.-P. Correa-Baena, C. R. Carmona, G. Richardson, J. M. Foster, F. de Angelis, J. M. Ball, A. Petrozza,

N. Mine, M. K. Nazeeruddin, W. Tress, M. Grätzel, U. Steiner, A. Hagfeldt, A. Abate, Migration of cations induces reversible performance losses over day/night cycling in perovskite solar cells, Energy & Environmental Science 10 (2) (2017) 604–613. doi:10.1039/C6EE03352K.

[80] M. Lira-Cantú, Perovskite solar cells: Stability lies at interfaces, Nature Energy 2 (7). doi:10.1038/nenergy.2017.115.

[81] L. Zhao, R. A. Kerner, Z. Xiao, Y. L. Lin, K. M. Lee, J. Schwartz, B. P. Rand, Redox Chemistry Dominates the Degradation and Decomposition of Metal Halide Perovskite Optoelectronic Devices, ACS Energy Letters 1 (3) (2016) 595–602. doi:10.1021/acsenergylett.6b00320.

[82] J. Yang, B. D. Siempelkamp, D. Liu, T. L. Kelly, Investigation of CH3NH3PbI3 Degradation Rates and Mechanisms in Controlled Humidity Environments Using in Situ Techniques, ACS Nano 9 (2) (2015) 1955–1963. doi:10.1021/nn506864k.

[83] J. A. Christians, P. A. Miranda Herrera, P. V. Kamat, Transformation of the Excited State and Photovoltaic Efficiency of CH3NH3PbI3 Perovskite upon Controlled Exposure to Humidified Air, Journal of the American Chemical Society 137 (4) (2015) 1530–1538. doi:10.1021/ja511132a.

[84] R. Gottesman, E. Haltzi, L. Gouda, S. Tirosh, Y. Bouhadana, A. Zaban, E. Mosconi, F. de Angelis, Extremely Slow Photoconductivity Response of CH3NH3PbI3 Perovskites Suggesting Structural Changes under Working Conditions, The journal of physical chemistry letters 5 (15) (2014) 2662–2669. doi:10.1021/jz501373f.

[85] T. Leijtens, E. T. Hoke, G. Grancini, D. J. Slotcavage, G. E. Eperon, J. M. Ball, M. de Bastiani, A. R. Bowring, N. Martino, K. Wojciechowski, M. D. McGehee, H. J. Snaith, A. Petrozza, Mapping Electric Field-Induced Switchable Poling and Structural Degradation in Hybrid Lead Halide Perovskite Thin Films, Advanced Energy Materials 5 (20) (2015) 1500962. doi:10.1002/aenm.201500962.

[86] S. Bae, S. Kim, S.-W. Lee, K. J. Cho, S. Park, S. Lee, Y. Kang, H.-S. Lee, D. Kim, Electric-Field-Induced Degradation of Methylammonium Lead Iodide Perovskite Solar Cells, The journal of physical chemistry letters 7 (16) (2016) 3091–3096. doi:10.1021/acs.jpclett.6b01176.

[87] D. Bryant, N. Aristidou, S. Pont, I. Sanchez-Molina, T. Chotchunangatchaval, S. Wheeler, J. R. Durrant, S. A. Haque, Light and oxygen induced degradation limits the operational stability of methylammonium lead triiodide perovskite solar cells, Energy & Environmental Science 9 (5) (2016) 1655–1660. doi:10.1039/C6EE00409A.

[88] J. Xiong, B. Yang, C. Cao, R. Wu, Y. Huang, J. Sun, J. Zhang, C. Liu, S. Tao, Y. Gao, J. Yang, Interface degradation of perovskite solar cells and its modification using an annealing-free TiO2 NPs layer, Organic Electronics 30 (2016) 30–35. doi:10.1016/j.orgel.2015.12.010.

[89] K. Domanski, J.-P. Correa-Baena, N. Mine, M. K. Nazeeruddin, A. Abate, M. Saliba, W. Tress, A. Hagfeldt, M. Grätzel, Not All That Glitters Is Gold: Metal-Migration-Induced Degradation in Perovskite Solar Cells, ACS Nano 10 (6) (2016) 6306–6314. doi:10.1021/acsnano.6b02613.

[90] J. You, L. Meng, T.-B. Song, T.-F. Guo, Y. Yang, W.-H. Chang, Z. Hong, H. Chen, H. Zhou, Q. Chen, Y. Liu, N. D. Marco, Improved air stability of perovskite solar cells via solution-processed metal oxide transport layers, Nature Nanotechnology 11 (1) (2016) 75–81. doi:10.1038/nnano.2015.230.

[91] M. V. Khenkin, E. A. Katz, A. Abate, G. Bardizza, J. J. Berry, C. Brabec, F. Brunetti, V. Bulović, Q. Burlingame, A. Di Carlo, R. Cheacharoen, Y.-B. Cheng, A. Colsmann, S. Cros, K. Domanski, M. Dusza, C. J. Fell, S. R. Forrest, Y. Galagan, D. Di Girolamo, M. Grätzel, A. Hagfeldt, E. von Hauff, H. Hoppe, J. Kettle, H. Köbler, M. S. Leite, S. Liu, Y.-L. Loo, J. M. Luther, C.-Q. Ma, M. Madsen, M. Manceau, M. Matheron, M. McGehee, R. Meitzner, M. K. Nazeeruddin, A. F. Nogueira, Ç. Odabaşı, A. Osherov, N.-G. Park, M. O. Reese, F. de Rossi, M. Saliba, U. S. Schubert, H. J. Snaith, S. D. Stranks, W. Tress, P. A. Troshin, V. Turkovic, S. Veenstra, I. Visoly-Fisher, A. Walsh, T. Watson, H. Xie, R. Yıldırım, S. M. Zakeeruddin, K. Zhu, M. Lira-Cantu, Consensus statement for stability assessment and reporting for perovskite photovoltaics based on ISOS procedures, Nature Energy 5 (1) (2020) 35–49. doi:10.1038/s41560-019-0529-5.

[92] C. Wiesmeier, I. Haedrich, K.-A. Weiss, I. Duerr, Overview of PV module encapsulation materials, Photovoltaics International 19 (2013) 85–92.

[93] R. Cheacharoen, C. C. Boyd, G. F. Burkhard, T. Leijtens, J. A. Raiford, K. A. Bush, S. F. Bent, M. D. McGehee, Encapsulating perovskite solar cells to withstand damp heat and thermal cycling, Sustainable Energy & Fuels 2 (11) (2018) 2398–2406. doi:10.1039/c8se00250a.

[94] I. Hwang, I. Jeong, J. Lee, M. J. Ko, K. Yong, Enhancing Stability of Perovskite Solar Cells to Moisture by the Facile Hydrophobic Passivation, ACS Applied Materials & Interfaces 7 (31) (2015) 17330–17336. doi:10.1021/acsami.5b04490.

[95] F. Bella, G. Griffini, J.-P. Correa-Baena, G. Saracco, M. Grätzel, A. Hagfeldt, S. Turri, C. Gerbaldi, Improving efficiency and stability of perovskite solar cells with photocurable fluoropolymers, Science (New York, N.Y.) 354 (6309) (2016) 203–206. doi:10.1126/science.aah4046.

[96] M. O. Reese, S. A. Gevorgyan, M. Jørgensen, E. Bundgaard, S. R. Kurtz, D. S. Ginley, D. C. Olson, M. T. Lloyd, P. Morvillo, E. A. Katz, A. Elschner, O. Haillant, T. R. Currier, V. Shrotriya, M. Hermenau, M. Riede, K. R. Kirov, G. Trimmel, T. Rath, O. Inganäs, F. Zhang, M. Andersson, K. Tvingstedt, M. Lira-Cantu, D. Laird, C. McGuiness, S. Gowrisanker, M. Pannone, M. Xiao, J. Hauch, R. Steim, D. M. DeLongchamp, R. Rösch, H. Hoppe, N. Espinosa, A. Urbina, G. Yaman-Uzunoglu, J.-B. Bonekamp, A. J. van Breemen, C. Girotto, E. Voroshazi, F. C. Krebs, Consensus stability testing protocols for organic photovoltaic materials and devices, Solar Energy

Materials and Solar Cells 95 (5) (2011) 1253–1267. doi:10.1016/j.solmat.2011.01.036.

[97] IEC, International Electrotechnical Commission, https://www.iec.ch/, accessed 26.03.2020.

[98] IEC, IEC 61215-2:2016 Terrestrial photovoltaic (PV) modules - Design qualification and type approval - Part 2: Test procedures (2016).

[99] M. Saliba, M. Stolterfoht, C. M. Wolff, D. Neher, A. Abate, Measuring Aging Stability of Perovskite Solar Cells, Joule 2 (6) (2018) 1019–1024. doi:10.1016/j.joule.2018.05.005.

[100] H. Tan, A. Jain, O. Voznyy, X. Lan, F. P. García de Arquer, J. Z. Fan, R. Quintero-Bermudez, M. Yuan, B. Zhang, Y. Zhao, F. Fan, P. Li, L. N. Quan, Y. Zhao, Z.-H. Lu, Z. Yang, S. Hoogland, E. H. Sargent, Efficient and stable solution-processed planar perovskite solar cells via contact passivation, Science (New York, N.Y.) 355 (6326) (2017) 722–726. doi:10.1126/science.aai9081.

[101] C. Zhao, B. Chen, X. Qiao, L. Luan, K. Lu, B. Hu, Revealing Underlying Processes Involved in Light Soaking Effects and Hysteresis Phenomena in Perovskite Solar Cells, Advanced Energy Materials 5 (14) (2015) 1500279. doi:10.1002/aenm.201500279.

[102] S. Novalin, M. Rennhofer, J. Summhammer, Electrical metastabilities in chalcogenide photovoltaic devices, Thin Solid Films 535 (2013) 261–264. doi:10.1016/j.tsf.2012.10.041.

[103] S. Siebentritt, M. Igalson, C. Persson, S. Lany, The electronic structure of chalcopyrites-bands, point defects and grain boundaries, Progress in Photovoltaics: Research and Applications 18 (6) (2010) 390–410. doi:10.1002/pip.936.

[104] R. Kenny, M. Nikolaeva-Dimitrova, E. Dunlop, Performance Measurements of CIS Modules: Outdoor and Pulsed Simulator Comparison for Power and Energy Rating, in: 2006 IEEE 4th World Conference on Photovoltaic Energy Conference, IEEE, 07.05.2006 - 12.05.2006, pp. 2058–2061. doi:10.1109/WCPEC.2006.279907.

[105] K. A. Bush, A. F. Palmstrom, Z. J. Yu, M. Boccard, R. Cheacharoen, J. P. Mailoa, D. P. McMeekin, R. L. Z. Hoye, C. D. Bailie, T. Leijtens, I. M. Peters, M. C. Minichetti, N. Rolston, R. Prasanna, S. Sofia, D. Harwood, W. Ma, F. Moghadam, H. J. Snaith, T. Buonassisi, Z. C. Holman, S. F. Bent, M. D. McGehee, 23.6%-efficient monolithic perovskite/silicon tandem solar cells with improved stability, Nature Energy 2 (2017) 17009 EP –. doi:10.1038/nenergy.2017.9.

[106] R. Cheacharoen, N. Rolston, D. Harwood, K. A. Bush, R. H. Dauskardt, M. D. McGehee, Design and understanding of encapsulated perovskite solar cells to withstand temperature cycling, Energy & Environmental Science 11 (1) (2018) 144–150. doi:10.1039/C7EE02564E.

[107] M. D. Kempe, G. J. Jorgensen, K. M. Terwilliger, T. J. McMahon, C. E. Kennedy, T. T. Borek, Acetic acid production and glass transition concerns with ethylene-vinyl acetate used in photovoltaic devices, Solar Energy Materials and Solar Cells 91 (4) (2007) 315–329. doi:10.1016/j.solmat.2006.10.009.

[108] S. Weber, T. Rath, J. Mangalam, B. Kunert, A. M. Coclite, M. Bauch, T. Dimopoulos, G. Trimmel, Investigation of NiOx-hole transport layers in triple cation perovskite solar cells, Journal of Materials Science: Materials in Electronics 29 (3) (2018) 1847–1855. doi:10.1007/s10854-017-8094-9.

[109] W. Yan, S. Ye, Y. Li, W. Sun, H. Rao, Z. Liu, Z. Bian, C. Huang, Hole-Transporting Materials in Inverted Planar Perovskite Solar Cells, Advanced Energy Materials 6 (17) (2016) 1600474. doi:10.1002/aenm.201600474.

[110] L. Ouyang, C. Musumeci, M. J. Jafari, T. Ederth, O. Inganäs, Imaging the Phase Separation Between PEDOT and Polyelectrolytes During Processing of Highly Conductive PEDOT:PSS Films, ACS Applied Materials & Interfaces 7 (35) (2015) 19764–19773. doi:10.1021/acsami.5b05439.

[111] S.-I. Na, G. Wang, S.-S. Kim, T.-W. Kim, S.-H. Oh, B.-K. Yu, T. Lee, D.-Y. Kim, Evolution of nanomorphology and anisotropic conductivity in solvent-modified PEDOT:PSS films for polymeric anodes of polymer solar cells, Journal of Materials Chemistry 19 (47) (2009) 9045. doi:10.1039/B915756E.

[112] J. Luo, D. Billep, T. Waechtler, T. Otto, M. Toader, O. Gordan, E. Sheremet, J. Martin, M. Hietschold, D. R. T. Zahn, T. Gessner, Enhancement of the thermoelectric properties of PEDOT:PSS thin films by post-treatment, Journal of Materials Chemistry A 1 (26) (2013) 7576. doi:10.1039/C3TA11209H.

[113] G. Adam, M. Kaltenbrunner, E. D. Głowacki, D. H. Apaydin, M. S. White, H. Heilbrunner, S. Tombe, P. Stadler, B. Ernecker, C. W. Klampfl, N. S. Sariciftci, M. C. Scharber, Solution processed perovskite solar cells using highly conductive PEDOT:PSS interfacial layer, Solar Energy Materials and Solar Cells 157 (2016) 318–325. doi:10.1016/j.solmat.2016.05.011.

[114] W. Chen, F.-Z. Liu, X.-Y. Feng, A. B. Djurišić, W. K. Chan, Z.-B. He, Cesium Doped NiO x as an Efficient Hole Extraction Layer for Inverted Planar Perovskite Solar Cells, Advanced Energy Materials 7 (19) (2017) 1700722. doi:10.1002/aenm.201700722.

[115] S. Lany, J. Osorio-Guillén, A. Zunger, Origins of the doping asymmetry in oxides: Hole doping in NiO versus electron doping in ZnO, Physical Review B 75 (24) (2007) 1199. doi:10.1103/PhysRevB.75.241203.

[116] Y.-H. Seo, I. H. Cho, S.-I. Na, Investigation of sol-gel and nanoparticle-based NiOx hole transporting layer for high-performance planar perovskite solar cells, Journal of Alloys and Compounds 797 (2019) 1018–1024. doi:10.1016/j.jallcom.2019.05.204.

[117] J. Tang, D. Jiao, L. Zhang, X. Zhang, X. Xu, C. Yao, J. Wu, Z. Lan, High-performance inverted planar perovskite solar cells based on efficient hole-transporting layers from

well-crystalline NiO nanocrystals, Solar Energy 161 (2018) 100–108. doi:10.1016/j.solener.2017.12.045.

[118] W. Qiu, M. Buffière, G. Brammertz, U. W. Paetzold, L. Froyen, P. Heremans, D. Cheyns, High efficiency perovskite solar cells using a PCBM/ZnO double electron transport layer and a short air-aging step, Organic Electronics 26 (2015) 30–35. doi:10.1016/j.orgel.2015.06.046.

[119] Y. Shao, Z. Xiao, C. Bi, Y. Yuan, J. Huang, Origin and elimination of photocurrent hysteresis by fullerene passivation in CH3NH3PbI3 planar heterojunction solar cells, Nature Communications 5 (1) (2014) 5784. doi:10.1038/ncomms6784.

[120] S. Chen, J. R. Manders, S.-W. Tsang, F. So, Metal oxides for interface engineering in polymer solar cells, Journal of Materials Chemistry 22 (46) (2012) 24202. doi:10.1039/C2JM33838F.

[121] M. Xiao, F. Huang, W. Huang, Y. Dkhissi, Y. Zhu, J. Etheridge, A. Gray-Weale, U. Bach, Y.-B. Cheng, L. Spiccia, A fast deposition-crystallization procedure for highly efficient lead iodide perovskite thin-film solar cells, Angewandte Chemie (International ed. in English) 53 (37) (2014) 9898–9903. doi:10.1002/anie.201405334.

[122] J. Burschka, N. Pellet, S.-J. Moon, R. Humphry-Baker, P. Gao, M. K. Nazeeruddin, M. Grätzel, Sequential deposition as a route to high-performance perovskite-sensitized solar cells, Nature 499 (7458) (2013) 316–319. doi:10.1038/nature12340.

[123] Z. Zhong, Y. Zhong, C. Liu, S. Yin, W. Zhang, D. Shi, Study on the surface wetting properties of treated indium-tin-oxide anodes for polymer electroluminescent devices, physica status solidi (a) 198 (1) (2003) 197–203. doi:10.1002/pssa.200306583.

[124] R. Hamaguchi, M. Yoshizawa-Fujita, T. Miyasaka, H. Kunugita, K. Ema, Y. Takeoka, M. Rikukawa, Formamidine and cesium-based quasi-two-dimensional perovskites as photovoltaic absorbers, Chemical communications (Cambridge, England) 53 (31) (2017) 4366–4369. doi:10.1039/C7CC00921F.

[125] A. Reinders, P. Verlinden, W. van Sark, A. Freundlich, Photovoltaic solar energy: From fundamentals to applications / edited by Angele Reinders, Pierre Verlinden, Wilfried van Sark, Alexandre Freundlich, John Wiley & Sons Ltd, Chichester, West Sussex, United Kingdom and Hoboken, NJ, 2017.

[126] J. A. Christians, J. S. Manser, P. V. Kamat, Best Practices in Perovskite Solar Cell Efficiency Measurements. Avoiding the Error of Making Bad Cells Look Good, The journal of physical chemistry letters 6 (5) (2015) 852–857. doi:10.1021/acs.jpclett.5b00289.

[127] J. I. Goldstein, D. E. Newbury, J. R. Michael, N. W. Ritchie, J. H. J. Scott, D. C. Joy, Scanning Electron Microscopy and X-Ray Microanalysis, Springer New York, New York, NY, 2018. doi:10.1007/978-1-4939-6676-9.

[128] P. Hofmann, Solid state physics: An introduction / by Philip Hofmann, second edition Edition, Wiley-VCH, Weinheim, 2015.

[129] Miho Yasaka (Ed.), X-ray thin-film measurement techniques: V . X-ray reflectivity measurement, no. 26 in The Rigaku Journal, 2010.

[130] S. Millow, Profilometer, Thieme Gruppe, 2005.
URL https://roempp.thieme.de/lexicon/RD-16-05526

[131] B. Bhushan, Modern tribology handbook, Mechanics and materials science series, CRC Press, Boca Raton, FL, 2001.

[132] Q. Han, S.-H. Bae, P. Sun, Y.-T. Hsieh, Y. M. Yang, Y. S. Rim, H. Zhao, Q. Chen, W. Shi, G. Li, Y. Yang, Single Crystal Formamidinium Lead Iodide (FAPbI3): Insight into the Structural, Optical, and Electrical Properties, Advanced materials (Deerfield Beach, Fla.) 28 (11) (2016) 2253–2258. doi:10.1002/adma.201505002.

[133] V. L. Pool, B. Dou, D. G. van Campen, T. R. Klein-Stockert, F. S. Barnes, S. E. Shaheen, M. I. Ahmad, M. F. A. M. van Hest, M. F. Toney, Thermal engineering of FAPbI3 perovskite material via radiative thermal annealing and in situ XRD, Nature Communications 8 (2017) 14075. doi:10.1038/ncomms14075.

[134] D. Yao, C. Zhang, N. D. Pham, Y. Zhang, V. T. Tiong, A. Du, Q. Shen, G. J. Wilson, H. Wang, Hindered Formation of Photoinactive δ-FAPbI3 Phase and Hysteresis-Free Mixed-Cation Planar Heterojunction Perovskite Solar Cells with Enhanced Efficiency via Potassium Incorporation, The journal of physical chemistry letters 9 (8) (2018) 2113–2120. doi:10.1021/acs.jpclett.8b00830.

[135] J. Mangalam, T. Rath, S. Weber, B. Kunert, T. Dimopoulos, A. Fian, G. Trimmel, Modification of NiOx hole transport layers with 4-bromobenzylphosphonic acid and its influence on the performance of lead halide perovskite solar cells, Journal of Materials Science: Materials in Electronics 30 (10) (2019) 9602–9611. doi:10.1007/s10854-019-01294-0.

[136] P. Wangyang, H. Sun, X. Zhu, D. Yang, X. Gao, Mechanical exfoliation and Raman spectra of ultrathin PbI2 single crystal, Materials Letters 168 (2016) 68–71. doi:10.1016/j.matlet.2016.01.034.

[137] H. R. Fallah, M. Ghasemi, A. Hassanzadeh, H. Steki, The effect of deposition rate on electrical, optical and structural properties of tin-doped indium oxide (ITO) films on glass at low substrate temperature, Physica B: Condensed Matter 373 (2) (2006) 274–279. doi:10.1016/j.physb.2005.11.159.

[138] K. Shameli, M. B. Ahmad, A. Zamanian, P. Sangpour, P. Shabanzadeh, Y. Abdollahi, M. Zargar, Green biosynthesis of silver nanoparticles using Curcuma longa tuber powder, International journal of nanomedicine 7 (2012) 5603–5610. doi:10.2147/IJN.S36786.

List of Figures

List of Tables